UNIVERSITA' DEGLI STUDI DI MILANO

PhD Course in Industrial Chemistry – XXVIII Cycle

DEVELOPMENT OF PHOTOCATALYTIC MATERIALS FOR SOLAR LIGHT CONVERSION INTO FUELS

PhD Student:

R10090 - Ivan GRIGIONI

Supervisor: Prof. Elena SELLI

Co-supervisor: Dr. Gian Luca CHIARELLO

A.A. 2014-2015

Index

– CHAPTER 5 –

Size-dependent performance of CdSe quantum dots in the photocatalytic evolution of hydrogen under visible light irradiation

– CHAPTER 6 –

Dynamics of photogenerated charge carriers in WO_3/$BiVO_4$ heterojunction photoanodes

– CHAPTER 7 –

– CHAPTER 8 –

The effects of surface carbon-containing impurities on the performances of TiO_2-based materials in the photocatalytic CO_2 reduction

– CHAPTER 9 –

Conclusions and perspectives

List of Figures

- CHAPTER 1 -

- CHAPTER 2 -

- CHAPTER 3 -

- CHAPTER 4 -

- CHAPTER 5 -

- CHAPTER 6 -

- CHAPTER 7 -

- CHAPTER 8 -

8.11. Photocatalytic H_2 accumulation profile over the Pt/Cu(0.1)/T photocatalyst in the presence of N_2 and water vapors as the only electron donor.

List of Schemes

- CHAPTER 2 -

- CHAPTER 4 -

- CHAPTER 6 -

- CHAPTER 7 -

List of Tables

- CHAPTER 5 –

- CHAPTER 6 -

- CHAPTER 7 -

- CHAPTER 8 –

List of Graphs

- Chapter 7 -

List of Acronyms

CB	Conduction band
VB	Valence band
E_g	Energy gap
E_F	Fermi level energy
V_{fb}	Flat band potential
E_{Fh}	Semi fermi level of holes
E_{Fe}	Semi fermi level of electrons
OER	Oxygen Evolution Reaction
RHE	Reversible Hydrogen Electrode
NHE	Normal Hydrogen Electrode
η_{STH}	Solar to hydrogen efficiency
fs-TAS	Femtosecond transient absorption spectroscopy
PA	Photoinduced absorption
PB	Photobleaching
SE	Stimulated emission
OPA	Optical parametric amplification
QDs	Quantum dots

NCs	Nanocrystals
FESEM	Field emission scanning electron microscope
PEC	Photoelectrochemical
IPCE	Incident photon to current efficiency

Chapter 1

Feeding the planet, with renewable and sustainable energy

“And if in a distant future the supply of coal becomes completely exhausted, civilization will not be checked by that, for life and civilization will continue as long as the sun shines! If our black and nervous civilization, based on coal, shall be followed by a quieter civilization based on the utilization of solar energy, that will not be harmful to progress and to human happiness.”[1] That is what Ciamician wrote, with a farseeing attitude, in 1912.

Today, coal has been flanked by other fossil fuels such as methane and oil but we are still looking for economical ways to exploit solar light. In the meantime we still burn *fossil solar energy* stored during millions of years into hydrocarbons, with an increasing consumption rate.

1. THE ENERGY ISSUE

Although our economic and social organization is completely based on the utilization of fossil fuels, there is a diffuse awareness that it is absolutely unsustainable to persist in such a way. Many environmental (climate change, increased probability of extreme weather, aridity, pollution), social (health problems such as the increase of cancer cases, wars and tension in area close to fossil fuels extraction) and economical (fuel crisis, oil price rise due to demand increase) problems have been correlating to our massive use of traditional energy sources. Therefore, we have to change the way to power with energy our society before it will be too late. Nowadays, in the developed countries, we would not be able to sustain our way of life without the traditional sources of energy. On the other hand, the direct access to electricity makes the difference between poor and rich countries. In fact more than 1.6 billion people in the developing world do not have access

to the energy service.[2] Moreover, the stocks of fossil fuels will be largely depleted during the current century and a middle term price rise have to be taken into account.

All the alternative energy sources are not storable as fossil fuels are, therefore we will progressively shift to an economy based on electricity.[3] This challenge represents a unique opportunity to drive the developed economies toward an innovative and sustainable reorganization of their social and economic assets. Moreover science, and chemistry first, will have a central role in establishing new concepts, ideas, materials and processes and lead to the development of practical solutions in the production, utilization, storage and distribution of the new energy sources.

2. THE RENEWABLE ENERGY SOURCES

Among all the renewable energy sources hydroelectricity has been the first employed. Today, hydroelectricity is by far the most largely used renewable energy source and contributes to around 16% of the total global electricity demand and to around 2% of the total energy consumed worldwide.[4] On the other hand, in the developed counties hydropower is exploited almost to its intrinsic limit. Moreover the construction of new dams implies several drawbacks, such as the geographical modification of entire areas and the consequent destruction of biodiversity.

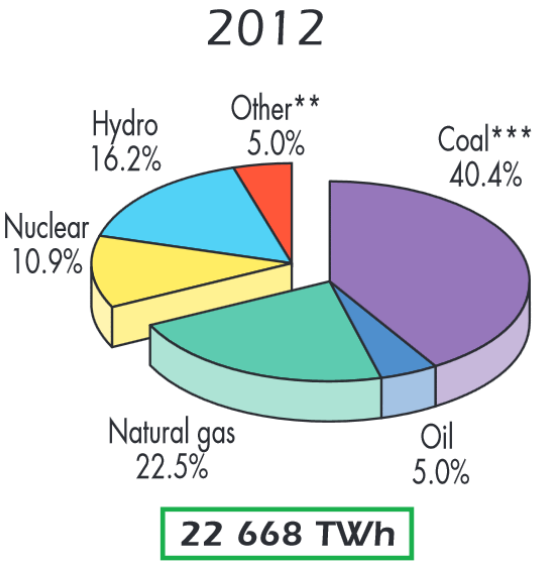

Figure 1.1. World total electricity generation by source during 2012.[4]

Nuclear energy is the second most widely used not-fossil energy source and accounts for *ca.* 11% of the total electricity produced globally and therefore *ca.* 1.4% of the world's

energy consumption. On the other hand, while nuclear energy has been initially considered the most promising technology to produce electricity, after 60 years of experience, its environmental and economical sustainability has not been completely proved. Long term storage of the by-products is a big issue, as well as the decommissioning of the nuclear plants arrived at the end of their lifecycle. Moreover, the possibility of unexpected accidents like that in Fukushima in 2011 or in Chernobyl in 1986 showed that safety is a crucial and unsolved issue for nuclear energy. As a consequence of such increasing concerns and of the high maintenance costs of nuclear plants, the number of operating reactors remained almost unchanged over the last 20 years and from 2010 the production of nuclear energy started to decrease.[4]

The remaining renewable energy sources (including mainly solar, geothermal and wind) accounts for no more than 5% of the world's electricity consumption. On the other hand, solar energy is by far the most abundant between all renewable and non-renewable energy sources.[5] In only 1.5 hour the sun delivers the same amount of energy that all the humankind consumes in an entire year.[6] Therefore a far better exploitation of this inextinguishable energy source is an essential and vital need.

3. SOLAR ENERGY CONVERSION

Solar light possesses a large amount of energy. The sun provides to our planet an intense flux of high energetic photons capable to promote extremely up-hill reactions, such as the photosynthetic fixation of CO_2 in biological systems. This energy flow drives life on Earth.

The AM 1.5G is the global solar irradiation spectra at the mid latitude and an irradiation power density of 1000 W m^2 is widely assumed as the average value at this latitude. The

reference photon composition of the solar irradiation flux is reported in Figure 1.2.[7] UV photons (having wavelengths ranging from 280 nm up to 400 nm) account for 4.5% of the total flux delivered to our planet. Visible photons (from 400 nm up to 900 nm) constitute 62.1 % of the total flux, while the IR region (from 900 nm up to 4000 nm) accounts for the remaining 33.4 %.

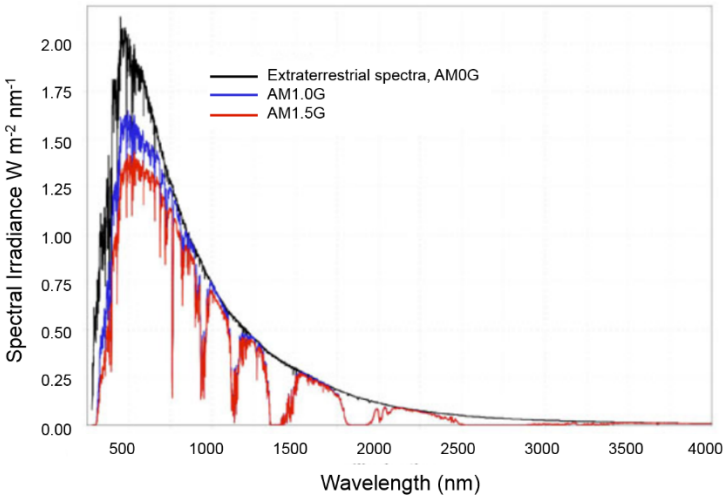

Figure 1.2. Extra-terrestrial AM 0G (black trace), equatorial AM 1.0G (blue trace) and middle latitude AM1.5G (red trace) standard solar spectra.[7]

Photovoltaic (PV) technology has been rapidly improved during the last 50 years and nowadays silicon based PV panels with conversion efficiencies exceeding 10% are widely available at affordable price. The Joint Research Center of the European Commission has studied the possibility to satisfy the entire European electricity consumption using PV panels. The percentage of the land area that needs to be covered with PV modules with a conversion efficiency of 10% in order to fulfil the electricity needs of the European Community is only about 0.6% of the total European territory.[8] On the other hand, the so generated electricity is not directly storable, unless it is accumulated in batteries or coupled with electrolysis.

Photocatalysis and photoelectrocatalysis offer the great possibility to directly convert solar energy into chemical bonds and therefore potentially solve the storage problems. While photocatalytic processes have been discovered in 1972,[9] very recently approaches led to the first demonstrations of practical devices showing solar to chemical conversion

efficiency exceeding 10%.[10] In the next two Chapters the basic principles of photocatalytic and photoelectrocatalytic processes are discussed, together with some of the most important and promising results obtained to date.

REFERENCES

(1) Ciamician, G. The Photochemistry of the Future. *Science* **1912**, *36*, 385–394.

(2) http://www.globalissues.org/article/26/poverty-Facts-and-Stats.

(3) Armaroli, N.; Balzani, V. Towards an Electricity-Powered World. *Energy Environ. Sci.* **2011**, *4*, 3193.

(4) http://www.iea.org/publications/freepublications/publication/keyworld2014.pdf.

(5) Perez, R.; Perez, M. The World's Energy Reserves. A Fundamental Look. *SHC Sol. Updat.* **2009**, *50*, 2–3.

(6) Lewis, N. S.; Nocera, D. G. Powering the Planet: Chemical Challenges in Solar Energy Utilization. *Proc. Natl. Acad. Sci. U. S. A.* **2006**, *103*, 15729–15735.

(7) http://rredc.nrel.gov/solar/spectra/am1.5.

(8) Šúri, M.; Huld, T. A.; Dunlop, E. D.; Ossenbrink, H. A. Potential of Solar Electricity Generation in the European Union Member States and Candidate Countries. *Sol. Energy* **2007**, *81*, 1295–1305.

(9) Fujishima, A.; Honda, K. Electrochemical Photolysis of Water at a Semiconductor Electrode. *Nature* **1972**, *238*, 37–38.

(10) Ager III, J. W.; Shaner, M.; Walczak, K.; Sharp, I. D.; Ardo, S. Experimental Demonstrations of Spontaneous, Solar-Driven Photoelectrochemical Water Splitting. *Energy Environ. Sci.* **2015**, *2*, 1–3.

Chapter 2

Basic Principles of Photocatalysis and some promising applications

Photocatalysis and photoinduced phenomena occurring under illumination at the interface between a photoactive material and a solution or gas-phase reactant, has been object of scientific research in the last two centuries. E. Becquerel in 1839 reported evidence of the first photocatalytic effect involving an illuminated silver chloride electrode in contact with an electrolyte solution in an electrochemical cell.[1] The Becquerel effect had to wait till 1954 to be completely explained through studies on the semiconducting properties of Ge.[2] At that time the scientific community was discovering the great potentials of semiconducting materials. Several successive studies followed the pioneering work about the photochemistry of Ge. Between 1954 and 1970, many semiconductor materials have been object of fundamental investigations aimed at understand and explain the semiconductor–electrolyte junction and the first models have been established.[3] After these early merely fundamental research on such systems, the possible application of photoelectrochemistry and photocatalysis in solar light conversion and storage was widely recognized. Fujishima and co-workers reported for the first time the evidence that water oxidation to O_2 was feasible over irradiated n-type TiO_2 at negative potentials, opening the opportunities that water could be split directly through the photoactivation of semiconductor electrodes.[4] In 1979 Inoue reported CO_2 reduction using different semiconductor photoelectrodes under irradiation with the application of a large electrical bias.[5]

1. PHOTOCATALYTIC WATER SPLITTING, BASIC PRINCIPLES

Photoassisted water splitting and carbon dioxide reduction to H_2 and hydrocarbons respectively, offer many attractive opportunities. H_2 and hydrocarbons are far much more easily stored than electricity or heat than photovoltaics and solar–thermal energy.[6] Moreover, these energy vectors could be used as building blocks in

chemical refinery and ammonia synthesis. Finally H_2 has extremely low environmental impact because it should be produced directly from water and is virtually renewable. On the other hand CO_2 reduction offers a way to buffer the rising atmospheric concentration of such pollutant. Furthermore the use of hydrocarbons obtained from its photoassisted reduction in the presence of water has nearly zero environmental impact.[7,8] Finally the development of these two fields offers the opportunity to produce solar fuels directly or close to the place they are used, with low transportation costs and the potential solution to the many conflicts and political tensions arising from the necessity of abundant fossil fuels.

Water splitting and carbon dioxide reduction are both endergonic reactions that need energy to drive the cleavage of hydrogen and carbon bonds with oxygen and to form the new high energetic C-H and H-H bonds. Photocatalytic processes offer the great opportunity to use solar light to carry out these reactions. In this way the energy supplied by photons can be stored in the new formed chemical bonds.

We now consider water splitting as a model reaction. To complete H_2 and O_2 production, the overall process is divided in the two separate oxidation and reduction half-reactions as follows:

Reduction reaction

$$2H^+ + 2e^- \rightarrow H_2 \qquad E^\circ_{red} = 0.00\ V\ vs\ RHE$$

Oxidation reaction

$$2H_2O + 4h^+ \rightarrow O_2 + 4H^+ \qquad E^\circ_{ox} = -1.23\ V\ vs\ RHE$$

Overall reaction

$$2H_2O \rightarrow 2H_2 + O_2 \qquad \Delta E = -1.23\ V$$

with the potentials against the reversible hydrogen electrode (RHE).[9]

Complete water splitting in an electrochemical cell needs a minimal external potential of 1.23 V. However a small overpotential is required to obtain oxygen and H_2 evolution. For example, state of the art electrolyzer devices need at least a bias of 1.8 V. In photodriven applications such potential corresponds to the photon energy. The lowest energy needed to carry out water splitting is 1.23 eV and correspond to ca 1000 nm wavelength photons. More than 70 % of the solar radiation possesses such energy. Otherwise due to the above mentioned overpotential, only photons with wavelengths shorter than 700 nm (43% of the solar spectrum) possesses enough energy to overcome the oxidation and reduction energy losses.[10]

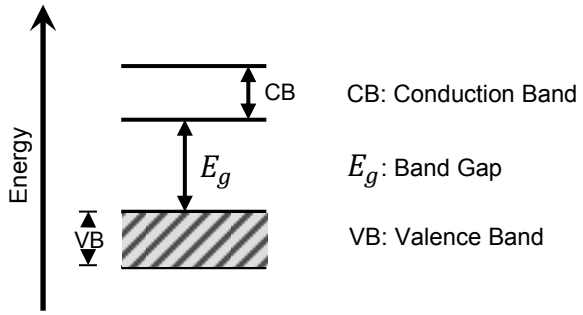

Scheme 2.1. Simplified scheme of the electronic structure of a semiconductor.

In photocatalytic or photoelectrocatalytic processes, the photon energy can be transformed in chemical energy through the excitation of an appropriate semiconducting material; the sequence following of the events involved is described in Scheme 2.1. After the absorption of a photon with energy greater than the semiconductor band gap (E_g) an e^-/h^+ pair is generated. The electron is photopromoted to a higher energy in the semiconductor conduction band (CB) while the hole counterpart has an energy close or equal to the valence band energy (VB). The so produced charge carriers can induce the reduction of electron acceptor species, having a reduction potential lower in energy than the CB, and the oxidation of electron donor species, having a reduction potential higher in energy than the VB, respectively.[11]

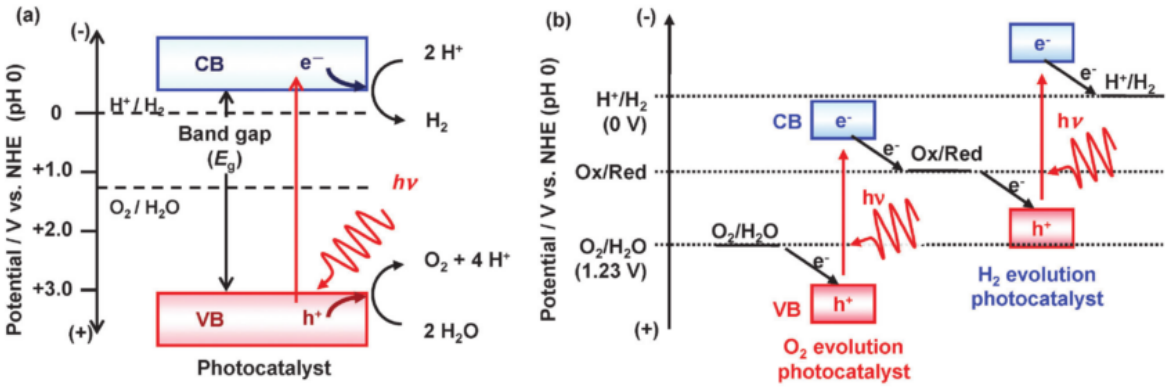

Figure 2.1. Energy diagram of photocatalytic water splitting showing a) the single semiconductor and b) Z-scheme approaches.[13]

This separation in energy does not mean necessarily a separation in space, with the consequence that direct e^-/h^+ recombination highly limits the overall photocatalytic process. In photoelectrocatalytic (PEC) approaches, as those discussed in Chapter 3, the application of an external electrical bias leads to more efficient charge separation because of the formation of a space charge region.[12]

We now take photocatalysis as a prototypical light assisted process and we discuss some basic concepts that are going to be useful in the successive discussion. The energy schemes for photocatalytic water splitting is reported in Figure 2.1, as well as the potentials for the reduction and oxidation reactions.[13]

1.1 Water splitting on a single semiconductor

The ideal case in which a single photocatalyst meets all the requirements (namely, E_g higher than the energy needed for water splitting and appropriate valence and conduction hand edge positions) is depicted in Figure 2.1a. Moreover, despite a wider band gap has a larger overpotential to efficiently carry out more the two semi reactions, only material with E_g < 3.2 eV should be considered in order to allow harvesting a significant portion of the solar spectrum.

For its suitable band edge position, high stability in strong oxidizing solutions and low cost, TiO_2 has been the most studied semiconductor for the overall water splitting reaction. Although in the first reports TiO_2 was employed as a photoanode material for water photoelectrochemical oxidation, this semiconductor has been successively employed and studied as a standalone material, without the support of an external bias.[14–16] During the last four decades many efforts have been made to overcome the drawbacks of this material, first of all the relatively large band gap (for anatase 3.0 eV and for rutile 3.2 eV), limiting its possible solar–to–hydrogen efficiency to 2-3 % only. Many strategies have been developed and adopted to selectively narrow the E_g of TiO_2: nitrogen, fluorine and sulphur doping,[17–20] grafting,[21] thermal reduction up to the so called “black titania”,[22–24] sensitization with organic/inorganic dyes[25] and nanostructuration.[26,27] Unfortunately none of them led to the effective activation of TiO_2 under visible light. On the other hand many of this studies have contributed to deeply understand photocatalytic processes and many techniques used with TiO_2 to improve charge separation of oxygen and hydrogen evolution are now widely employed for different semiconducting materials. For example, the use of electron donors such as organic molecules (methanol, ethanol, ascorbic acid and others) to increase the lifetime of photoexcited electrons by scavenging photogenerated holes, or the use of noble metal nanoparticles to scavenge, photopromoted electrons, are all approaches that can be adopted with any other semiconductor material.[15,28–30]

Another key factor limiting TiO_2 light conversion efficiency is the slow oxygen evolution kinetics typical of this material. Indeed, in the absence of an appropriate sacrificial agent, H_2 and O_2 production rates are very low.

TiO_2 is not the only material employed for the overall water splitting reaction, but only rare examples of materials ensuring linear evolution of both O_2 and H_2 with time have been reported so far.[31] In particular, Ni doped $InTaO_4$ has been one of the first materials which has been shown to allow overall water splitting, with a quantum yield of 0.66% at 402 nm and stoichiometric H_2 and O_2 evolution under visible light (λ>420 nm) radiation.[32] More recently the GaN and ZnO solid solution was found to exhibit water splitting under visible irradiation with excellent stability. In both cases the importance of the use of co-catalysts for hydrogen evolution was highlighted, and especially the GaN:ZnO solid solution[33], which was found to be inactive without RuO_2 or $NiO/Rh_{2-y}Cr_yO_3$ cocatalysts. Loading with such co-catalysts improve charge separation and thus the overall water splitting becomes feasible. On the other hand, the presence of an oxidation co-catalysts has no important effects. For example Mn_3O_4 loading on GaN:ZnO does not enable overall water splitting, pointing out how hydrogen evolution is a weak point for activating the photocatalyst in this reaction.[34] Moreover, the co-loading of a oxygen evolution catalyst (Mn_3O_4, RuO_2 or IrO_2) in the presence of a hydrogen production co-catalyst (core/shall Rh/Cr_2O_3) increases the water splitting rate by a factor of 1.4 at most.[35] The $(Ga_{0.88}Zn_{0.12})(N_{0.88}O_{0.12})$ with an interesting 2.6 eV band gap is the best performing photocatalyst for overall water splitting under visible light, with the highest apparent quantum efficiency of 5.1 % at 410 nm.[36]

1.2 The Z-scheme approach

Despite the many efforts put forth developing a singular material for complete water splitting under solar light irradiation also with recent promising results, a more versatile strategy has been the object of an increasing interest. This second approach to achieve the water splitting reaction is described in Figure 2.1b. In the Z-

scheme or tandem or D4 approach the overall reaction is rationally divided into two semireactions and two different narrow band gap semiconductors are used, one for water oxidation and the second for water reduction.[37] Two photons need to be absorbed by each of the two photocatalysts to produce a H_2 molecule. As discussed in Chapter 3, this kind of approach finds wide application in photoelectrocatalysis but the great advantage of having the two reactions occurring at the two separate semiconductors is extremely useful in photocatalytic systems as well. First of all, the use of two separate photocatalysts open the possibility to employ smaller band gap materials, active with a greater portion of the solar radiation; moreover larger overpotentials are accessible without the need of absorbing highly energetic photons (see Figure 2.1b). Many semiconductors meet this two less restrictive prerequisites; for example single metal or binary oxides (Fe_2O_3, WO_3, and $BiVO_4$), oxynitride (TaON, SmON) for oxygen evolution and calcogenides such as CdSe, CdS and CdSSe or GaP and GaAs for hydrogen production (see Figure 2.2).

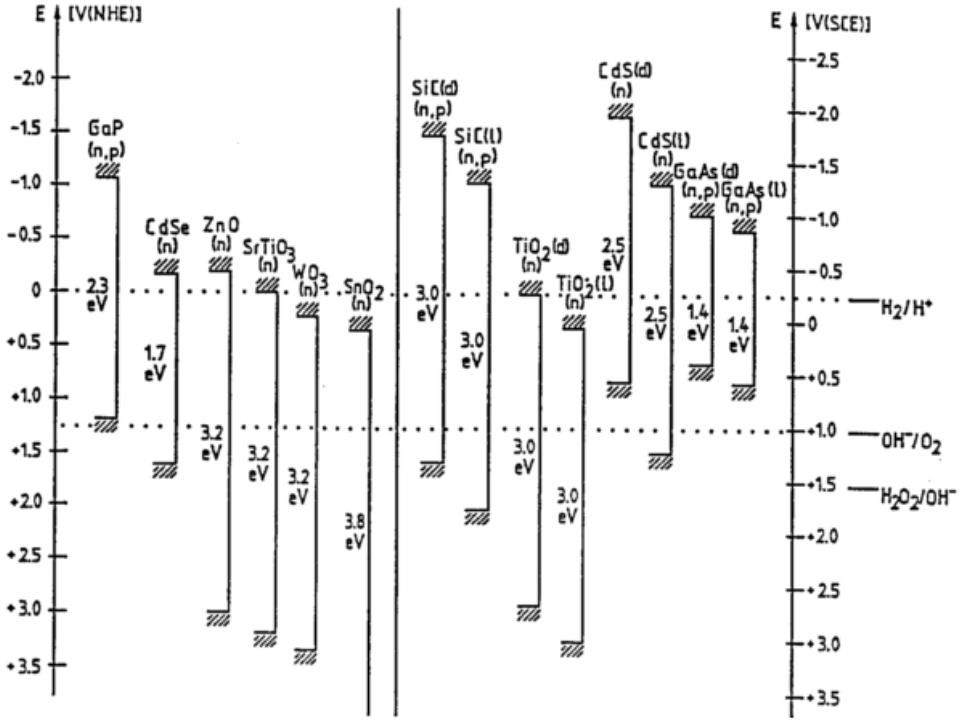

Figure 2.2. Energy gap and positions of the edges of various photocatalytic materials, in dark (labelled with d) and under light irradiation (labelled with l), with respect to the electrochemical scale.[3]

In the Z-scheme the majority carriers recombine at the junction between the two semiconductors while photogenerated holes and electrons, the minority carriers, responsible for the oxygen and hydrogen evolution reactions, are respectively, more efficiently separated. Moreover, research can focus on improving only one of the two semireactions and carry out more detailed investigations on single topics, without getting lost in the complexity of the overall water splitting reaction.

Recently an increasing number of papers appeared claiming the successful attainment of complete Z-scheme water splitting with both H_2 and O_2 production occurring simultaneously at the corresponding photocatalyst.[13] Furthermore Z-scheme water splitting can be attained with two different configurations: over the two separate materials in the presence of a redox mediator or over a monolithic photocatalyst obtained through the direct heterojunction of the two semiconductors. The highest apparent quantum yield of 6.3% at 420 nm was achieved using Pt-loaded ZrO_2/TaON as hydrogen evolution photocatalyst and Pt-loaded WO_3 as oxygen evolution photocatalyst in a Z-scheme system using IO_3^-/I^- as a redox couple.[38,39] The redox mediator drives the recombination of photopromoted electrons and of photogenerated holes at the oxidation and reduction materials respectively. IO_3^- acts as an acceptor at the water oxidation side (Pt/WO_3) while I^- ions act as electron donors at the water reduction side. This study is an example of how the knowledge gained during decades of studies (1970-2010) on TiO_2-based materials is now successfully applied on new generation semiconductors. In fact, without noble metal deposition over both photocatalysts, neither O_2 nor H_2 evolution occur. The deposition of a noble metal co-catalyst leads to a better charge separation and boosts surface electron transfer paths.

Another example of Z-scheme using separate semiconductor nanoparticles is the combination of Ru-loaded $SrTiO_3$ doped with rhodium ($SrTiO_3$:Rh) as water reducing material and $BiVO_4$ as water oxidation material.[40] Again, it is worth nothing how a wide band gap material studied since the beginning of photocatalysis, such as $SrTiO_3$, has been revisited using the modern strategy of employing Rh as a donor impurity in the valence band and hence allowing $SrTiO_3$ to absorb visible light through band gap narrowing. The redox mediator used with such photocatalyst combination is $[Co(bpy)_3]^{3+/2+}$ and the overall Z-scheme system has an excellent apparent quantum yield of 2.1% at 420 nm. The same photocatalyst combination ($SrTiO_3$:Ru and $BiVO_4$) generates stoichiometric amounts of hydrogen and oxygen in the absence of redox mediator, when the two oxides are aggregated together in a heterojunction system. The redox mediator-unassisted water splitting was possible due to the presence of Rh, having reversible whose oxidation states.[41]

Cadmium selenide, CdS, was one of the first materials showing excellent hydrogen evolving properties, due to its high conduction band (-1.5 V vs NHE) and good visible light absorption.[42] A colloidal solution of CdS was irradiated with monochromatic light in the presence of deaerated Na_2S aqueous solution and a quantum yield of 50% was obtained. Other chalcogenide p-type materials have been widely employed as hydrogen evolution photocatalyst.

As already mentioned before a positive aspect of the Z-scheme or tandem system is the possibility to study the oxidation and reduction reactions separately and to improve selectively only one side at a time. In order to check the oxygen or the hydrogen evolution catalyst alone suitable electron donors or acceptors are needed. For example methanol or other water soluble organic compounds can be used as electron donors, while silver or iron ions are often used as electron acceptors. Also

inorganic electron donors, such as Na_2SO_3 or Na_2S, are widely employed. This hole scavenger are more reactive than water and are consumed irreversibly, therefore are referred as sacrificial reagents. Their higher reactivity in one of the two half reactions is due to their more suitable redox potential.

For example the reduction of silver cations to metallic silver is thermodynamically more feasible than proton reduction to hydrogen ($E^{\circ}_{Ag^+/Ag}$ is + 0.80 V while $E^{\circ}_{H^+/H_2}$ is + 0.00 V for definition *vs* RHE). Hence Ag^+ is more easily reduced than water and can be used to consume photopromoted electrons and, increases the hole lifetime in the studied material.[43–46] Similarly, methanol is a far better electron donor than water because the standard potential for the reduction of carbonic acid to methanol is more negative than that of water oxidation ($E^{\circ}_{H_2CO_3\,(aq)}$ / CH_3OH is 0.04 V while $E^{\circ}_{O_2/H_2O}$ is 1.23 V *vs* RHE).[47]

Furthermore, the kinetics of methanol (organics) oxidation is extremely less demanding than water oxidation. In fact, while in photocatalytic water splitting assisted by the presence of methanol the oxidation of this compound proceeds through successive, increasingly oxidized, stable compounds (CH_3OH → CH_2O → HCOOH / CO → CO_2), overall water splitting has to proceed through a 4 holes process that involves highly unstable intermediates that easily undergo the back reactions.[48] Moreover, most of the methanol oxidation intermediates are soluble in water/organic solution and can directly dissolve in the reaction mixture. For these reasons methanol, as well as other organics, are widely employed to fill photogenerated holes as sacrificial hole scavenger.[49] Doing so the lifetime of photopromoted electrons can be extended and the reducing properties of the studied material are consequently increased. Is noteworthy that even if a photocatalyst is active in the two semireactions in the presence of sacrificial reagent, the material

should be inactive in the overall water splitting. This is because the scavenging process highly suppress e^-/h^+ recombination.

For example $Sm_2TiS_2O_4$ has been reported to be a promising photocatalyst for both half reactions separately but it is inactive in the overall reaction despite the correct bang edge position and the interesting 2.0 eV band gap.[50] $LaGaS_2O$ and La_3GaS_5O are both active in hydrogen and oxygen evolution, in the presence of Na_2S-Na_2SO_3 as hole scavenger and $AgNO_3$ as electron scavenger, respectively, but no H_2 or O_2 are detected in pure water.[51]

The most studied photocatalytic materials for water oxidation are WO_3, $BiVO_4$ and oxynitride materials such as $BaTaO_2N$,[52] TaON,[53] $SrNbO_2N$[43] or oxysulphides such as $Sm_2Ti_2S_2O_5$. Only few materials can be used as photocatalysts for the half reactions because of the harsh conditions needed and because self-oxidation of the photocatalyst itself is an issue. Again, the use of a co-catalyst improves the material activity and properties, for example it was found that the position of IrO_2 on TaON leads to a substantial increase of the stability of the material.

Semiconductor photocatalysts for hydrogen evolution are less prone to self photoxidation because a reduction reaction take place at their surface. A material for such application needs a conduction band more negative in energy than the proton reduction potential. Metal sulphides are attractive candidates as hydrogen evolution photocatalysts because of their narrow band gap and their suitable band edge position. Their valence band consists mainly of S_{3p} orbitals witch are more negative in energy than O_{2p} orbitals.[54]

CdS is one of the first semiconductor studied for the water reduction under visible light. With its 2.4 eV band gap can efficiently harvest solar energy up to 550 nm. The

first reports using CdS for photocatalytic H_2 evolution have been published in the early 80s.[55] More recently CdS loaded with Pt as co-catalyst and in the presence of Na_2SO_3 and Na_2S as sacrificial agents has been reported to show quantitative apparent quantum yields of more than 60% at 420 nm and ~ 20% at 500 nm with hydrogen production rates exceeding 26 mmol h^{-1} g_{cat}^{-1} under λ> 420 nm irradiation.[42] Also ZnS has been studied for this reaction but despite excellent H_2 evolution rates obtained with such material, its wide band gap (3.1- eV) limits its utilization under solar light.[56]

Metal sulphide solid solutions possess the attractive property of having tunable band gap and band edge position. The ZnS-$CuInS_2$-$AgInS_2$ solid solution has been investigated for its customizable band gap ranging from 3.5 to 1.5 eV, respectively, for ZnS and $(CuAg)_{0.5}In_1S_2$.[57] This material showed H_2 evolution over most of the visible spectrum with apparent quantum yields ranging from 7% at 470 nm and ~ 1% up to 750-780 nm, from an aqueous K_2SO_3-Na_2S solution and with 0.5 wt% loading of Pt. More recently Cu_2ZnSnS_4 (CZS) in the presence of Pt or Au as hydrogen evolution co-catalysts have been employed in the water splitting in an aqueous solution containing Na_2S and Na_2SO_3 as electron donor sacrificial agents.[58] This 1.5 eV E_g material allowed stable H_2 evolution rates under full lamp irradiation using a 300 W Xe lamp. More generally most of the semiconductor used in photovoltaic research (CIGS, CZTS, InP, GaP, CIS and more) can be used as hydrogen evolution photocatalysts because their conduction band is negatively shifted in energy with respect to the water reduction potential. Recently researches are successfully trying to stabilize Si that, with its abundance and small band gap energy (1.12 eV), has attracted great interest since the first report as photoelectrode material in 1976.[59]

With the raise of nanotechnology, the discovery of quantum size effects and the rapid development of facile and reproducible synthetic routes for a wide range of semiconducting nanocrystals, research a hydrogen evolution materials made a step forward through increased efficiency and solar light harvesting.

CdSe quantum dots, as well as other transition metal chalcogenides QDs, have many characteristics that make them eligible as photocatalyst for hydrogen production in Z-scheme solar driven water splitting devices. In CdSe, the band gap energy can be tuned from 1.9 eV of the bulk material up to 2.6 eV for 1.2 nm diameter nanocrystals. Quantum confinement allows to select the band gap by varying the QDs size. Moreover both experimental and modeling studies evidenced that the valence band energy is not affected by the QDs size and that only the QDs conduction band energy position is size-dependent. So, by varying the CdSe nanocrystal (NC) size from a bulk-like nanoparticle (with diameter more than 8-10 nm for spherical particles) down to 1.2 nm size sphere having respectively 1.9 and 2.6 eV E_g, the conduction band shifts to more negative potentials of 1.5 eV (see Figure 2.3).[60,61] Thus photopromoted electrons possess higher overpotentials to carry proton reduction. On the other hand the correlated increase of the band gap leads to a less complete utilization of the solar spectrum.

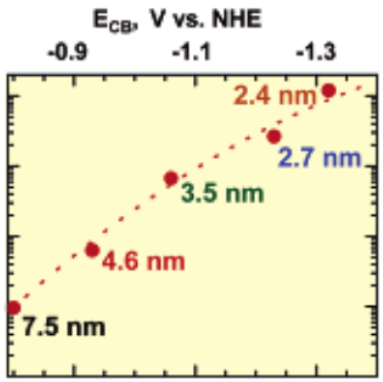

Figure 2.3. Dependence of CB energy position on QDs size.[61]

Durability is also important for photocatalytic materials and CdSe QDs have reported steady H_2 evolution rates during 15 days long testes under 520 nm, 13 mW/cm^2 light, provided by a LED source and in the presence of an aqueous ascorbic acid solution as sacrificial agent and a novel soluble Ni^{2+} co-catalyst.[49,62]

The possibility to obtain different quantum confined nanostructures through the use of appropriate non-coordinating solvents and new synthetic strategies have open the way to efficiently achieve charge separation, by decreasing charge carriers recombination rates, thus improving the apparent quantum efficiency.[63] For example CdSe nanorods, single and doubled-tipped with Pt nanoparticles, have been tested in the water reduction reaction under visible light in the presence of Na_2S and Na_2SO_3 as electron donor.[64] Surprisingly, the authors have found that the single tipped nanorods are three times more active toward H_2 production. In this nanostructure photogenerated holes and electrons can be separated: the electrons accumulate at the Pt side, while holes favorably diffuse at the unoccupied side. There holes can be trapped at the defect sites and successively transferred to the sacrificial agent.

Nanostructuring strategies also allow the engineering of multicomponent photocatalysts containing a light absorber, an hole acceptor and an electron acceptor. This all in one strategy can lead to the quick and effective delocalization of the photogenerated charges. For example triadic heterostructures are now extensively studied and the recombination kinetics of photogenerated excited states can be followed through pump and probe techniques such as time resolved fluorescence and absorption spectroscopy. For example CdSe/CdS-Pt dot-in-rod synthetized through the CdS nanorods growth over a CdSe QDs seed has been recently studied for H_2 production from water splitting in the presence of sacrificial electron donors (methanol and Na_2SO_3).[47] In this structure electrons are collected at the Pt side while holes accumulate at the CdSe QDs, being separated from the electrons counterparts of several microns. The study also pointed out how hole separation and stabilization is crucial to achieve higher efficiency.

2. HYDROGEN PRODUCTION USING CdSe QUANTUM DOTS WITH DIFFERENT SIZES

During the second half of the first year and part of the second year of my PhD I focused my research on the setup of the synthesis of CdSe QDs with different size. The adopted synthetic route was one of the most widely used because of the high resulting NC quality and limited hazard of the precursors. The procedure uses trioctylphosphine oxide (TOPO) as non-coordinating solvent, stable at temperature higher than 300°C, and trioctylphosphine (TOP) as reactant to dissolve metallic selenium in the organic media. Both reagents are technical grade (purity > 80%) and allow to maintain the reaction temperature at 270°C without any decomposition. On the other hand higher purity grade TOPO and TOP undergo thermal degradation, leading to CdO_2 formation at high temperature (and the resulting appearance of a brown coloration).

The so obtained QDs were then studied in the photocatalytic reduction of water under visible light ($\lambda > 420$ nm) using Na_2SO_3 as electron donor. The study was aimed to the identification of the best performing QDs size for the hydrogen evolution reaction to be employed in a Z-scheme configuration for the overall water splitting. In Chapter 5 we discuss the size-dependent CdSe water reduction properties found during such investigation.

REFERENCES

(1) Becquerel, E. A. Recherches Sur Les Effets de La Radiation Chimique de La Lumiere Solaire Au Moyen Des Courants Electriques. *Comptes Rendus L´Academie des Sci.* **1839**, *9*, 145–149.

(2) Turner, D. R. The Anode Behavior of Germanium in Aqueous Solutions. *J. Electrochem. Soc.* **1956**, *103*, 252.

(3) Nozik, A. J.; Memming, R. Physical Chemistry of Semiconductor−Liquid Interfaces.pdf. *J. Phys. Chem.* **1996**, *100*, 13061–13078.

(4) Fujishima, A.; Honda, K. Electrochemical Photolysis of Water at a Semiconductor Electrode. *Nature* **1972**, *238*, 37–38.

(5) Inoue, T.; Fujishima, A.; Konishi, T.; Honda, K. Photoelectrocatalytic Reduction of Carbon Dioxide in Aqueous Suspensions of Semiconductor Powders. *Nature* **1979**, *277*.

(6) Armaroli, N.; Balzani, V. Towards an Electricity-Powered World. *Energy Environ. Sci.* **2011**, *4*, 3193.

(7) Ahmed, N.; Morikawa, M.; Izumi, Y. Photocatalytic Conversion of Carbon Dioxide into Methanol Using Optimized Layered Double Hydroxide Catalysts. *Catal. Today* **2012**, *185*, 263–269.

(8) Tu, W.; Zhou, Y.; Zou, Z. Photocatalytic Conversion of CO_2 into Renewable Hydrocarbon Fuels: State-of-the-Art Accomplishment, Challenges, and Prospects. *Adv. Mater.* **2014**, *26*, 4607–4626.

(9) Prévot, M. S.; Sivula, K. Photoelectrochemical Tandem Cells for Solar Water Splitting. *J. Phys. Chem. C* **2013**, *117*, 17879–17893.

(10) http://rredc.nrel.gov/solar/spectra/am1.5.

(11) Hoffmann, M. R.; Martin, S. T.; Choi, W.; Bahnemann, D. W. Environmental Applications of Semiconductor Photocatalysis. *Chem. Rev.* **1995**, *95*, 69–96.

(12) Grätzel, M. Photoelectrochemical Cells. *Nature* **2001**, *414*, 338–344.

(13) Hisatomi, T.; Kubota, J.; Domen, K. Recent Advances in Semiconductors for

Photocatalytic and Photoelectrochemical Water Splitting. *Chem. Soc. Rev.* **2014**, *43*, 7520–7535.

(14) Chiarello, G. L.; Forni, L.; Selli, E. Photocatalytic Hydrogen Production by Liquid- and Gas-Phase Reforming of CH_3OH over Flame-Made TiO_2 and Au/TiO_2. *Catal. Today* **2009**, *144*, 69–74.

(15) Chiarello, G. L.; Aguirre, M. H.; Selli, E. Hydrogen Production by Photocatalytic Steam Reforming of Methanol on Noble Metal-Modified TiO_2. *J. Catal.* **2010**, *273*, 182–190.

(16) Chiarello, G. L.; Selli, E.; Forni, L. Photocatalytic Hydrogen Production over Flame Spray Pyrolysis-Synthesised TiO2 and Au/TiO2. *Appl. Catal. B Environ.* **2008**, *84*, 332–339.

(17) Dozzi, M. V.; Selli, E. Doping TiO_2 with P-Block Elements: Effects on Photocatalytic Activity. *J. Photochem. Photobiol. C Photochem. Rev.* **2013**, *14*, 13–28.

(18) Dozzi, M. V.; Andrea, C. D.; Ohtani, B.; Valentini, G.; Selli, E. Fluorine-Doped TiO_2 Materials: Photocatalytic Activity vs Time-Resolved Photoluminescence. *J. Phys. Chem. C* **2013**, *117*, 25586–25595.

(19) Tabata, M.; Maeda, K.; Higashi, M.; Lu, D.; Takata, T.; Abe, R.; Domen, K. Modified Ta_3N_5 Powder as a Photocatalyst for O_2 Evolution in a Two-Step Water Splitting System with an Iodate/iodide Shuttle Redox Mediator under Visible Light. *Langmuir* **2010**, *26*, 9161–9165.

(20) Dozzi, M. V.; Zuliani, A.; Grigioni, I.; Chiarello, G. L.; Meda, L.; Selli, E. Photocatalytic Activity of One Step Flame-Made Fluorine Doped TiO_2. *Appl. Catal. A Gen.* **2015**, *doi:10.1016/j.apcata.2015.10.048*.

(21) Irie, H.; Kamiya, K.; Shibanuma, T.; Miura, S.; Tryk, D. A.; Yokoyama, T.; Hashimoto, K. Visible Light-Sensitive Cu(II)-Grafted TiO_2 Photocatalysts: Activities and X-Ray Absorption Fine Structure Analyses. *J. Phys. Chem. C* **2009**, *113*, 10761–10766.

(22) Chen, X.; Liu, L.; Yu, P. Y.; Mao, S. S. Increasing Solar Absorption for Photocatalysis with Black Hydrogenated Titanium Dioxide Nanocrystals. *Science* **2011**, *331*, 746–750.

(23) Naldoni, A.; Allieta, M.; Santangelo, S.; Marelli, M.; Fabbri, F.; Cappelli, S.; Bianchi, C. L.; Psaro, R.; Santo, V. D. Effect of Nature and Location of Defects on Bandgap Narrowing in Black TiO_2 Nanoparticles. *J. Am. Chem. Soc.* **2012**,

134, 7600–7603.

(24) Danon, A.; Bhattacharyya, K.; Vijayan, B. K.; Lu, J.; Sauter, D. J.; Gray, K. A.; Stair, P. C.; Weitz, E. Effect of Reactor Materials on the Properties of Titanium Oxide Nanotubes. *ACS Catal.* **2012**, *2*, 45–49.

(25) Swierk, J. R.; Mallouk, T. E. Design and Development of Photoanodes for Water-Splitting Dye-Sensitized Photoelectrochemical Cells. *Chem. Soc. Rev.* **2013**, *42*, 2357–2387.

(26) Tian, J.; Zhao, Z.; Kumar, A.; Boughton, R. I.; Liu, H. Recent Progress in Design, Synthesis, and Applications of One-Dimensional TiO_2 Nanostructured Surface Heterostructures: A Review. *Chem. Soc. Rev.* **2014**, *43*, 6920–6937.

(27) Altomare, M.; Lee, K.; Killian, M. S.; Selli, E.; Schmuki, P. Ta-Doped TiO_2 Nanotubes for Enhanced Solar-Light Photoelectrochemical Water Splitting. *Chem. - A Eur. J.* **2013**, *19*, 5841–5844.

(28) Dozzi, M. V.; Prati, L.; Canton, P.; Selli, E. Effects of Gold Nanoparticles Deposition on the Photocatalytic Activity of Titanium Dioxide under Visible Light. *Phys. Chem. Chem. Phys.* **2009**, *11*, 7171–7180.

(29) Dozzi, M. V.; Chiarello, G. L.; Selli, E. Effects of Surface Modification and Doping on the Photocatalytic Activity of TiO_2. *J. Adv. Oxid. Technol.* **2010**, *13*, 305–312.

(30) Subramanian, V.; Wolf, E. E.; Kamat, P. V. Catalysis with TiO_2/gold Nanocomposites. Effect of Metal Particle Size on the Fermi Level Equilibration. *J. Am. Chem. Soc.* **2004**, *126*, 4943–4950.

(31) Kudo, A.; Miseki, Y. Heterogeneous Photocatalyst Materials for Water Splitting. *Chem. Soc. Rev.* **2009**, *38*, 253–278.

(32) Zou, Z.; Ye, J.; Sayama, K.; Arakawa, H. Direct Splitting of Water under Visible Light Irradiation with an Oxide Semiconductor Photocatalyst. *Nature* **2001**, *414*, 625–627.

(33) Maeda, K.; Takata, T.; Hara, M.; Saito, N.; Inoue, Y.; Kobayashi, H.; Domen, K. GaN:ZnO Solid Solution as a Photocatalyst for Visible-Light-Driven Overall Water Splitting. *J. Am. Chem. Soc.* **2005**, *127*, 8286–8287.

(34) Maeda, K.; Xiong, A.; Yoshinaga, T.; Ikeda, T.; Sakamoto, N.; Hisatomi, T.; Takashima, M.; Lu, D.; Kanehara, M.; Setoyama, T.; et al. Photocatalytic

Overall Water Splitting Promoted by Two Different Cocatalysts for Hydrogen and Oxygen Evolution under Visible Light. *Angew. Chemie - Int. Ed.* **2010**, *49*, 4096–4099.

(35) Xiong, A.; Yoshinaga, T.; Ikeda, T.; Takashima, M.; Hisatomi, T.; Maeda, K.; Setoyama, T.; Teranishi, T.; Domen, K. Effect of Hydrogen and Oxygen Evolution Cocatalysts on Photocatalytic Activity of GaN:ZnO. *Eur. J. Inorg. Chem.* **2014**, No. 4, 767–772.

(36) Maeda, K.; Domen, K. Photocatalytic Water Splitting: Recent Progress and Future Challenges. *J. Phys. Chem. Lett.* **2010**, *1*, 2655–2661.

(37) Maeda, K. Z‐Scheme Water Splitting Using Two Different Semiconductor Photocatalysts. *ACS Catal.* **2013**, *3*, 1486–1503.

(38) Maeda, K.; Higashi, M.; Lu, D.; Abe, R.; Domen, K. Efficient Nonsacrificial Water Splitting through Two-Step Photoexcitation by Visible Light Using a Modified Oxynitride as a Hydrogen Evolution Photocatalyst. *J. Am. Chem. Soc.* **2010**, *132*, 5858–5868.

(39) Abe, R.; Takata, T.; Sugihara, H.; Domen, K. Photocatalytic Overall Water Splitting under Visible Light by TaON and WO_3 with an IO_3^-/I^- Shuttle Redox Mediator. *Chem. Commun.* **2005**, No. 30, 3829–3831.

(40) Jia, Q.; Iwase, A.; Kudo, A. $BiVO_4$–Ru/$SrTiO_3$:Rh Composite Z-Scheme Photocatalyst for Solar Water Splitting. *Chem. Sci.* **2014**, *5*, 1513–1519.

(41) Ma, S. S. K.; Maeda, K.; Hisatomi, T.; Tabata, M.; Kudo, A.; Domen, K. A Redox-Mediator-Free Solar-Driven Z-Scheme Water-Splitting System Consisting of Modified Ta_3N_5 as an Oxygen-Evolution Photocatalyst. *Chem. - A Eur. J.* **2013**, *19*, 7480–7486.

(42) Bao, N.; Shen, L.; Takata, T.; Domen, K. Self-Templated Synthesis of Nanoporous CdS Nanostructures for Highly Efficient Photocatalytic Hydrogen Production under Visible Light. *Chem. Mater.* **2008**, *20*, 110–117.

(43) Maeda, K.; Higashi, M.; Siritanaratkul, B.; Abe, R.; Domen, K. $SrNbO_2N$ as a Water-Splitting Photoanode with a Wide Visible-Light Absorption Band. *J. Am. Chem. Soc.* **2011**, *133*, 12334–12337.

(44) Kato, H.; Asakura, K.; Kudo, A. Highly Efficient Water Splitting into H_2 and O_2 over Lanthanum-Doped $NaTaO_3$ Photocatalysts with High Crystallinity and Surface Nanostructure. *J. Am. Chem. Soc.* **2003**, *125*, 3082–3089.

(45) Pesci, F. M.; Cowan, A. J.; Alexander, B. D.; Durrant, J. R.; Klug, D. R. Charge Carrier Dynamics on Mesoporous WO_3 during Water Splitting. *J. Phys. Chem. Lett.* **2011**, *2*, 1900–1903.

(46) Ma, Y.; Pendlebury, S. R.; Reynal, A.; Le Formal, F.; Durrant, J. R. Dynamics of Photogenerated Holes in Undoped $BiVO_4$ Photoanodes for Solar Water Oxidation. *Chem. Sci.* **2014**, *5*, 2964–2973.

(47) Wu, K.; Chen, Z.; Lv, H.; Zhu, H.; Hill, C. L.; Lian, T. Hole Removal Rate Limits Photodriven H_2 Generation Efficiency in CdS-Pt and CdSe/CdS-Pt Semiconductor Nanorod-Metal Tip Heterostructures. *J. Am. Chem. Soc.* **2014**, *136*, 7708–7716.

(48) Tang, J.; Durrant, J. R.; Klug, D. R. Mechanism of Photocatalytic Water Splitting in TiO_2. Reaction of Water with Photoholes, Importance of Charge Carrier Dynamics, and Evidence for Four-Hole Chemistry. *J. Am. Chem. Soc.* **2008**, *130*, 13885–13891.

(49) Han, Z.; Qiu, F.; Eisenberg, R.; Holland, P. L.; Krauss, T. D. Robust Photogeneration of H_2 in Water Using Semiconductor Nanocrystals and a Nickel Catalyst. *Science* **2012**, *338*, 1321–1324.

(50) Ishikawa, A. Novel Synthesis and Photocatalytic Activity of Oxysulfide $Sm_2Ti_2S_2O_5$. *Chem. Mater.* **2003**, *15*, 4442.

(51) Ogisu, K.; Ishikawa, A.; Shimodaira, Y.; Takata, T.; Kobayashi, H.; Domen, K. Electronic Band Structures and Photochemical Properties of La−Ga-Based Oxysulfides. *J. Phys. Chem. C* **2008**, *112*, 11978–11984.

(52) Higashi, M.; Domen, K.; Abe, R. Fabrication of an Efficient $BaTaO_2N$ Photoanode Harvesting a Wide Range of Visible Light for Water Splitting. *J. Am. Chem. Soc.* **2013**, *135*, 10238–10241.

(53) Abe, R.; Higashi, M.; Domen, K. Facile Fabrication of an Efficient Oxynitride TaON Photoanode for Overall Water Splitting into H_2 and O_2 under Visible Light Irradiation. *J. Am. Chem. Soc.* **2010**, *132*, 11828–11829.

(54) Brook, S. The Absolute Energy Positions of Conduction and Valence Bands of Selected Semiconducting Minerals. *Am. Mineral.* **2000**, *85*, 543–556.

(55) Matsumura, M.; Saho, Y.; Tsubomura, H. Photocatalytic Hydrogen Production from Solutions of Sulfite Using Platinized Cadmium Sulfide Powder. *J. Phys. Chem.* **1983**, *87*, 3807–3808.

(56) Reber, J. F.; Meier, K. Photochemical Production of Hydrogen with Zinc-Sulfide Suspensions. *J. Phys. Chem.* **1984**, *88*, 5903–5913.

(57) Tsuji, I.; Kato, H.; Kudo, A. Photocatalytic Hydrogen Evolution on ZnS-$CuInS_2$-$AgInS_2$ Solid Solution Photocatalysts with Wide Visible Light Absorption Bands. *Chem. Lett.* **2006**, *18*, 1969–1975.

(58) Yu, X.; Shavel, A.; An, X.; Luo, Z.; Cabot, A.; Ibáñez, M. Cu_2ZnSnS_4-Pt and Cu_2ZnSnS_4-Au Heterostructured Nanoparticles for Photocatalytic Water Splitting and Pollutant Degradation. *J. Am. Chem. Soc.* **2014**, *136*, 9236–9239.

(59) Candea, R. M.; Kastner, M.; Goodman, R.; Hickok, N. Photoelectrolysis of Water: Si in Salt Water. *J. Appl. Phys.* **1976**, *47*, 2724–2726.

(60) Li, L.; Hu, J.; Yang, W.; Alivisatos, A. P. Band Gap Variation of Size- and Shape-Controlled Colloidal CdSE Quantum Rods. *Nano Lett.* **2001**, *1*, 349–351.

(61) Robel, I.; Kuno, M.; Kamat, P. V. Size-Dependent Electron Injection from Excited CdSe Quantum Dots into TiO_2 Nanoparticles. *J. Am. Chem. Soc.* **2007**, *129*, 4136–4137.

(62) Li, Z.-J.; Wang, J.-J.; Li, X.-B.; Fan, X.-B.; Meng, Q.-Y.; Feng, K.; Chen, B.; Tung, C.-H.; Wu, L.-Z. An Exceptional Artificial Photocatalyst, Ni_h-CdSe/CdS Core/Shell Hybrid, Made In Situ from CdSe Quantum Dots and Nickel Salts for Efficient Hydrogen Evolution. *Adv. Mater.* **2013**, *25*, 6613–6618.

(63) Zhu, H.; Song, N.; Lv, H.; Hill, C. L.; Lian, T. Near Unity Quantum Yield of Light-Driven Redox Mediator Reduction and Efficient H_2 Generation Using Colloidal Nanorod Heterostructures. *J. Am. Chem. Soc.* **2012**, *134*, 11701–11708.

(64) Bang, J. U.; Lee, S. J.; Jang, J. S.; Choi, W.; Song, H. Geometric Effect of Single or Double Metal-Tipped CdSe Nanorods on Photocatalytic H_2 Generation. *J. Phys. Chem. Lett.* **2012**, *3*, 3781–3785.

Chapter 3

The photoelectrochemical approach to split water

ABSTRACT

The photoelectrochemical approach to undergo light-to-chemical energy conversion reactions from water to H_2 and O_2 or from CO_2 to hydrocarbons has been first reported in 1971 and in 1979 (for carbon dioxide reduction). During these 40 years of investigation the understanding in this scientific field considerably increased also thanks to the parallel research in photocatalytic processes. As in the last Chapter we described the basic principles and strategies to obtain industrially interesting photocatalytic performances, in the present Chapter the physical and chemical basis of photoelectrochemical (PEC) systems are examined as well as the factors that nowadays seem to limit photoconversion efficiency.

1. PHOTOELECTROCHEMISTRY: SOME BASIC CONCEPTS

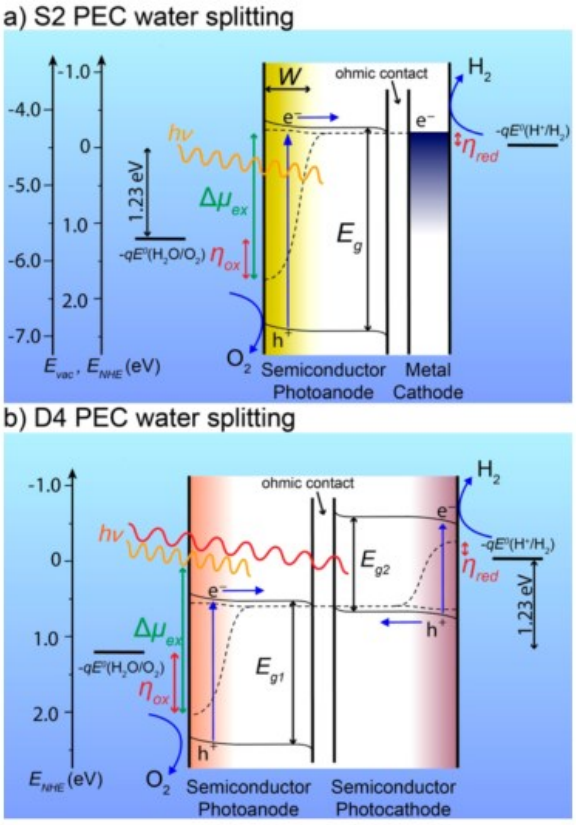

Figure 3.1: diagrams of the two different PEC approaches, a) S2, single semiconductor two photons and b) D4 double semiconductors, four photons.[47]

Taking PEC water splitting as an example, the overall reaction can be pursued in two different ways (see Figure 3.1a and Figure 3.1b), in analogy to the photocatalytic approach. In the ideal case, a single semiconductor can be used to drive complete water splitting by absorbing 2 photons to produce a H_2 molecule, this approach is called S2 scheme, single semiconductor, two photons, and it is schematically represented in Figure 3.1a. In Figure 3.2 the Fermi level equilibration is depicted between an n-type semiconductor

in contact with an electrolyte solution.[1] When the semiconductor is not in contact with the electrolyte solution (initial condition in Figure 3.2a) the band edge potentials and the Fermi level (E_F) are flat through the semiconductor because there it is no chemical potential equilibration. In that situation E_F correspond to the flat band potential V_{fb}, the maximum Fermi level possible in the material. In the example reported in **Figure 3.2** the n-type material is not able to undergo overall water splitting since its V_{fb} is lower in energy to the water reduction potential (as for Fe_2O_3, WO_3 or $BiVO_4$). When the photoelectrode is immersed in the electrolyte solution in the dark (Figure 3.2b), the Fermi level in the semiconductor equilibrates with the chemical potential of the electrolyte ($E_{F,redox}$):

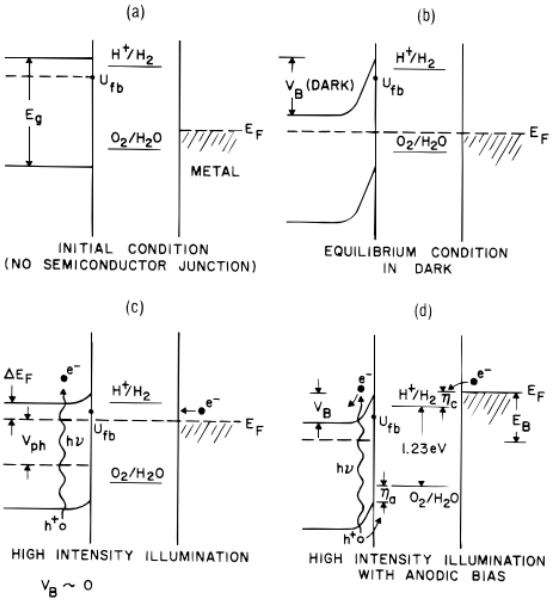

Figure 3.2: sequence of the energy diagrams for a PEC with the semiconductor photoelectrode and a metal counter electrode, from a) the starting situation, namely no contact with the electrolyte, b) after equilibration with the electrolyte in solution, c) under high intensity irradiation and d) under both high intensity irradiation and applied bias.[1]

$$E_F = E_{F,redox}$$

The conduction and valence bands in the bulk material move together with the Fermi level, while the energy level at the surface stays fixed, producing a band bending. The band bending causes holes accumulation (the minority carrier in an n-type material) at the junction between the semiconductor and the electrolyte (semiconductor-liquid junction SCLJ), while electrons in the conduction band, if populated in dark condition, move toward the bulk. Since electrons in an n-type material are the majority carriers, the electrons

concentration in the space close to the SCLJ result depleted: the depletion zone of thickness W is thus formed.

Charges segregation in the depletion zone leads to the presence of a dipole (space charge). Upon band gap excitation with a photon with energy $h\nu = E_g$ the space charge field drives the separation of photopromoted electrons in the conduction band and of photogenerated holes in the valence band. In n-type semiconductors, like most of the oxide materials, the band bending at the electrolyte is upward and the Fermi level shift to more positive potentials. For this kind of materials the photogenerated holes travel at the SCLJ where the Fermi level is more positive, while the photoexcited electrons move through the bulk toward the counter electrode. Under irradiation the presence of the depletion zone splits the Fermi level in two quasi-Fermi levels for holes (E_{Fh} positively shifted at the SCLJ) and for electrons (E_{Fe} more negative in energy and extending in the bulk toward the ohmic contact). Under high intensity irradiation E_{Fe} rises up to the flat band potential V_{fb} (Figure 3.2c), the highest possible potential energy for the electrons in the material. Because the counter electrode is in equilibrium with the irradiated semiconductor the Fermi level of the metal counter electrode equal that of photogenerated electrons. As a consequence, Fermi level separation generate a chemical potential $\Delta\mu_{ex}$ between the SCLJ and the counter electrode. It is noteworthy that $\Delta\mu_{ex} \leq E_g$ and that the energy gap of a semiconductor decreases when it is in contact with an electrolyte solution. Moreover two more energy losses comes from the overpotentials required for the oxidation and reduction reactions (η_{ox} and η_{red} respectively). If $\Delta\mu_{ex}$ is greater than the 1,23 V potential necessary to split water plus the two overpotentials, the overall reaction can proceed without the application of an external bias. For the semiconductor used as an example in

Figure 3.2 $\Delta\mu_{ex}$ is lower than the required potential and an external anodic potential is needed. The applied bias shifts the potential energy of the electrons in the counter electrode to more negative potentials, Figure 3.2d, allowing the hydrogen evolution reaction.

Due to the high overpotential required, the difference in energy of the two quasi-Fermi levels from the initial band edges and other loss processes, the band gap of a single oxide having an adequate $\Delta\mu_{ex}$ to directly carry out the overall water splitting precludes utilization of a large portion of the visible light spectrum. For this reason the identification of a material suitable for drive S2 water splitting with high solar-to-chemical efficiencies has not yet been achieved.

Instead of pursuing the demanding identification of a semiconductor with the band gap straddling the water oxidation and reduction potentials, it seems better to use the alternative approach of dividing the overall water splitting in the two separate half reactions, using two different narrow band gap light absorbers, respectively as a photoanode for oxygen evolution and a photocathode for hydrogen evolution. The schematic for this strategy is shown in Figure 3.1b. Here the two semiconductors have band gaps energy E_{g1} and E_{g2} that absorb complementary portions of the solar light spectrum. The photoanode is an n-type semiconductor. For such materials, because the band edges are favorably bent upward in proximity to the liquid junction, upon band gap excitation the holes can diffuse at the SCLJ and oxidize water to O_2. On the contrary the photocathode is a p-type semiconductor the band edges of which, after equilibration with the electrolyte redox couple (H^+/H_2) at the semiconductor/electrolyte junction, are bended downward allowing electrons to flow to the SCLJ and reduce water to H_2. In photoelectrocatalytic

devices, the two reactions are carried out on the two separate photoelectrodes by the photoexcited minority carriers. The majority carriers, electrons in the photoanode and holes in the photocathode, recombine through the ohmic contact. This two dual-absorbing tandem cell needs the absorption of four photons to produce a molecule of H_2 (D4 approach). Likewise in the two photocatalytic water splitting approaches described in Chapter 2, despite the D4 strategy needs twice the photons of a single semiconductor PEC cell, the former strategy offers the great advantage of allowing use of narrow band gap materials and consequently leads to a more efficient solar light utilization. Moreover, a wider range of semiconductor materials are available to be applied as photoanode or photocathode.

In the next Section the effects of the application of an external bias on the photoelectrode are examined in detail focusing the attention on n-type materials for water oxidation.

2. EVENTS FOLLOWING THE APPLICATION OF AN EXTERNAL BIAS IN A PHOTOELECTRODE

As discussed in the previous Chapter, while hydrogen evolution can be efficiently attained with the use of a co-catalyst, water oxidation is the major limitation for overall photocatalytic water splitting. Similarly, in PEC water splitting the large oxygen production overpotential η_{ox} still represents the major drawback for such application while the hydrogen evolution overpotential η_{red} at the photocathode is a minor issue. For that reason massive efforts have been put forth to overcome the limitations of water oxidation at the photoanode in PEC devices.

In the usual method for characterizing semiconductor materials for water oxidation, the photoanode and the counter electrode are connected to a potentiostat together with a

reference electrode in a three-electrode device. Without an external applied bias the potential of the electrons in the counter electrode is in equilibrium (identical) to the quasi-Fermi level of the electrons in the photoirradiated photoelectrode. The application of an external anodic bias has the dual scope to shift the Fermi level of the metal counter electrode upward and thus the quasi-Fermi level of the conduction band (which is in equilibrium with the counter electrode through the external circuit) above the H^+/H_2 potential and to increase the space-charge field, enhancing charge separation. Most of the studied photoanode materials such as WO_3, $BiVO_4$ and Fe_2O_3 are not able to directly undergo overall water splitting because their conduction bands are more positive than the water reduction potential. The external voltage, applied between the photoelectrode and the metal counter electrode, can be used to compensate the potential deficiency and allow water oxidation even if the Fermi level of the semiconductor oxide has an unfavorable potential.

As well as for photocatalytic Z-scheme systems it is possible to study only one half reaction materials at a time using appropriate electron donors (see Chapter 2). The application of an external bias allow the study of water oxidation on the photoanode alone, without the complexity of having a full assembled tandem device. As described in the next Section, in a complete dual absorber D4 tandem device it is not necessary to apply external electrical bias as the potential needed to drive the reduction reaction is supplied by a photovoltaic cell or hydrogen evolution takes place directly over the irradiated photocathode.

We now consider the effects of the application of a bias V on the energy scheme of a semiconductor as outlined in Figure 3.3 using Fe_2O_3 as an example material. When the electrode is polarized by a potentiostat and its potential moves more negatively (cathodic

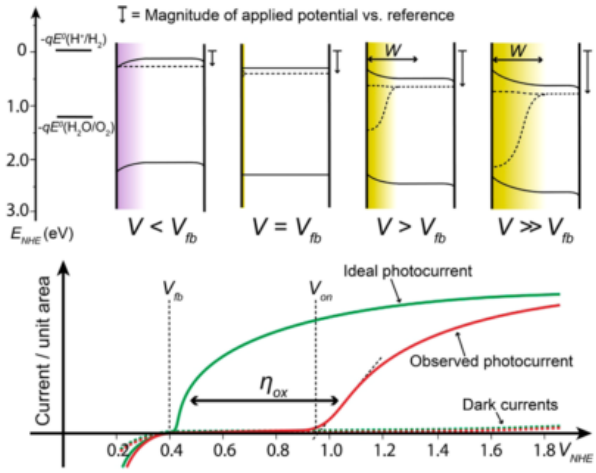

Figure 3.3: (top) energy level scheme of an n-type semiconductor photoanode, here Fe_2O_3, under polarization with cathodic and anodic potential. (bottom) Idealized and observed photocurrent density for the anodic reaction of oxygen evolution.[47]

shift or cathodic polarization) or more positively (anodic shift or anodic polarization) with respect to the initial conditions (the semiconductor not in contact with the electrolyte solution), the energy levels at the SCLJ stay fixed while the conduction and valence band potentials (E_{Fh} and E_{Fe}) move along with the reference potential. When the photoelectrode is polarized at the flat band potential V_{fb}, the current passing through the system is zero. By applying a cathodic potential ($V < V_{fb}$) a negative current appears and leads to an accumulation of majority carriers (electrons) at the SCLJ. Is it worth noting that in Fe_2O_3 the negative photocurrent is due to the accumulation of photopromoted electrons in the liquid interface; in WO_3 and in other oxide semiconductors this charging process leads to the electrochromic effect (shortly discussed in Chapter 7). On the other hand an accumulation of minority carriers occurs when the photoelectrode is polarized with an anodic potential ($V > V_{fb}$) and causes the formation of the depletion layer. The V_{fb} can be determined experimentally through impedance spectroscopy measurements or, less rigorously, as the potential where the current in the external circuit is zero (usually in the presence of electron donor species). The flat band potentials of the most studied photoanode materials Fe_2O_3, WO_3 and $BiVO_4$ are anodic to the H^+/H_2 potential and are 0.5 V, 0.4 V and 0.0 vs RHE respectively, using a semiconductor with positive V_{fb} (for example Fe_2O_3 in Figure 3.3,

bottom) means that the application of the external bias first shifts the Fermi level of the counter electrode at the water reduction potential. Once the potential at the flat band is raised, in an ideal situation the oxygen evolution reaction (OER) should take place with the application of a potential slightly anodic to the V_{fb}. In a real photoanode an overpotential (η_{ox}) has to be applied in order to allow accumulation of photoexcited holes at the SCLJ and overcome the oxygen evolution kinetics (red curve in Figure 3.3, bottom).

The effects of overpotential have been studied by carrying out PEC experiments in the presence of an electron donor in the electrolyte solution. The electron donors can be oxidized more easily, because their redox potential is more negative than water oxidation potential and so the chemical potential between the E_{Fh} and the redox couple is larger. Dotan et al. used as H_2O_2 hole scavenger, in order to understand the effects of the overpotential and to probe the factors limiting water oxidation in hematite electrodes made of two different techniques (Figure 3.4a).[2] In the presence of H_2O_2 at a potential only slightly greater than the V_{fb}, the oxidation of the hole scavenger takes place, indicating

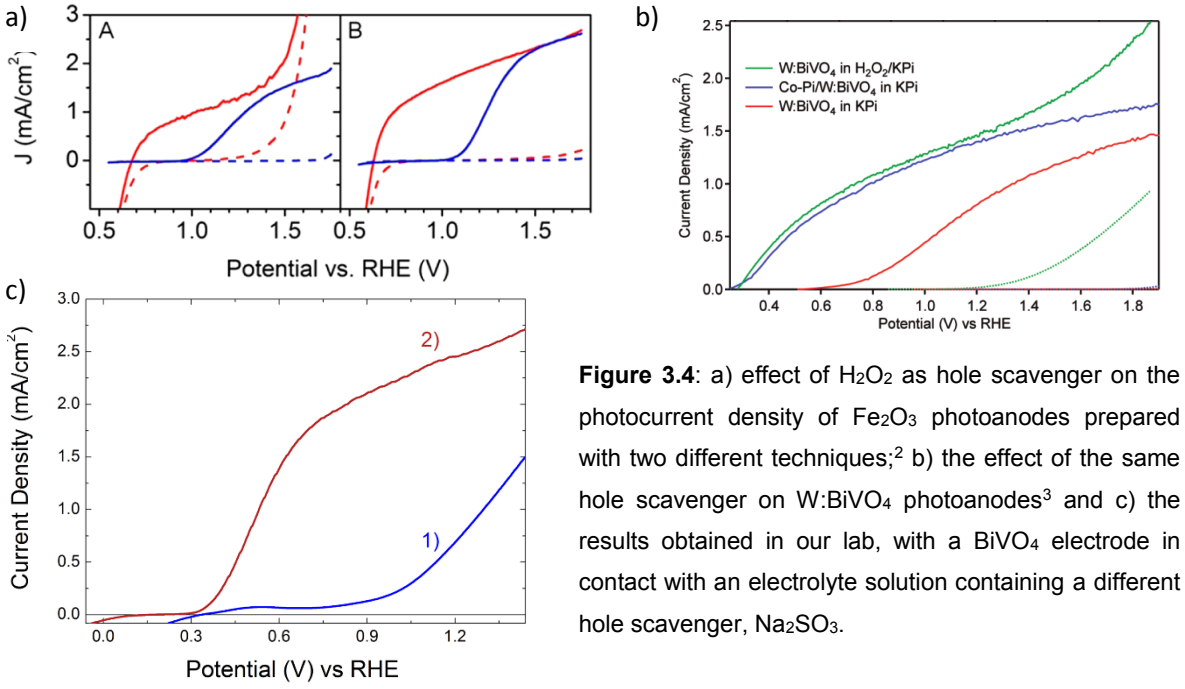

Figure 3.4: a) effect of H_2O_2 as hole scavenger on the photocurrent density of Fe_2O_3 photoanodes prepared with two different techniques;[2] b) the effect of the same hole scavenger on W:$BiVO_4$ photoanodes[3] and c) the results obtained in our lab, with a $BiVO_4$ electrode in contact with an electrolyte solution containing a different hole scavenger, Na_2SO_3.

that holes are indeed present at the SCLJ for the oxidation process. The O_2/H_2O_2 redox couple has a more negative oxidation potential with respect to that of O_2/H_2O. Therefore the chemical potential for the oxidation reaction is considerably larger and hole filling by the electron donor species becomes extremely favored. Surface electron/hole recombination is completely suppressed and photopromoted electrons can efficiently travel through the photoanode toward the counter electrode. Typically, water oxidation is not observed with hematite until about 1.0 V vs RHE, the cathodic shift in the presence of H_2O_2 suggest a η_{ox} of 0.5-0.6 V. Zhong et al. studied the photoresponse of $BiVO_4$ in the presence of H_2O_2. The PEC experiments reported in Figure 3.4b (red and green traces) show that the photocurrent onset is cathodically shifted for $BiVO_4$ as well, but, contrarily to Fe_2O_3, the oxidation of the electron donor species needs an overpotential of 300 mV to take place (in hematite the photocurrent rise almost at the V_{fb}).[3] The authors suggested that for $BiVO_4$, hydrogen peroxide suppresses surface charge recombination while bulk recombination is still an issue. We carried out similar experiments with a $BiVO_4$ photoanode in contact with an electrolyte solution containing Na_2SO_3 as hole scavenger. Also in our study we found that the photocurrent onset is more negative that using an inert electrolyte such as Na_2SO_4 (Figure 3.4c, trace 1) but it is still anodically shifted of ca. 300 mV with respect to V_{fb} (Figure 3.4c trace 2), a value consistent with that reported by Zhong et al. Moreover the SO_3^{2-}/SO_4^{2-} redox couple is more easily oxidizable than O_2/H_2O_2 (+0.17 V, +0.68 V vs RHE respectively) and surface charge recombination should be reasonably completely suppressed with such hole scavenger. This strengthens the possibility that the 300 mV overpotential is caused by bulk recombination and that the overpotential is necessary to build up a sufficient depletion layer to allow holes accumulation at the SCLJ.

In the following Section the most studied photoanode materials for the oxygen evolution reaction are described on the basis of their solar light harvesting properties, band gap position and state of the art achieved efficiency.

3. OXIDE SEMICONDUCTORS FOR PEC WATER OXIDATION

Transition metal oxide materials have been considered for the water oxidation reaction because of their narrow band gap and high stability in the harsh environment required for such reaction. The band gap of a metal oxide semiconductor is formed by O_{2p} orbitals for the valence band, while the conduction band is formed by the metal orbitals.

The prototype material is TiO_2, with the rutile and anatase phases having band gap energies in the range of 3.0-3.2 eV, which limits to 2-3% the solar conversion of the solar spectrum (see Figure 3.5 for an intuitive correlation between photoanodes band gap and solar to hydrogen efficiency).[4] Despite the intense effort focused on developing strategies, including C, S, N, F and B-doping, nanostructuration or dye sensitization, to decrease its band gap and allow visible light absorption and exploitation (refer to the Chaper 2 for a detailed bibliography), after over 40 years of investigations, a method that guarantees the absorption of a large portion of solar light by TiO_2, durability and industrially interesting

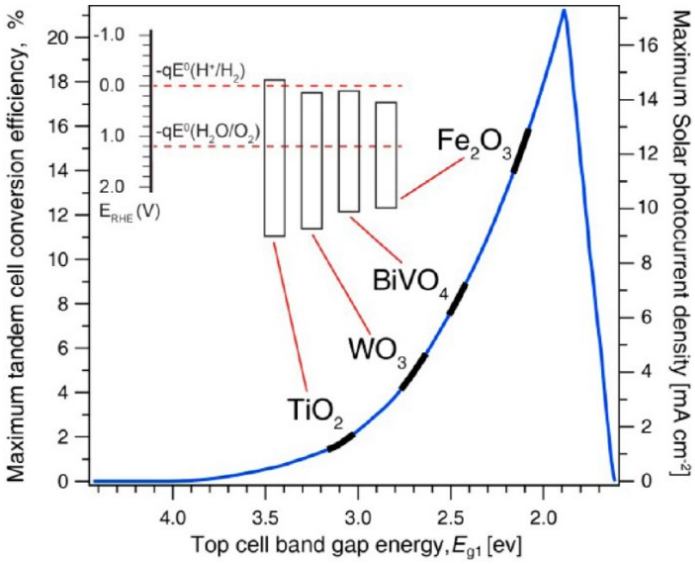

Figure 3.5: Maximum solar-to-hydrogen conversion efficiency and the corresponding photocurrent density, as a function of the energy gap of the photoanode material in a tandem device. The band gap and the maximum efficiency for the most studied oxide photoanodes are also shown.[4]

conversion efficiencies has not been found, neither with the most promising strategies (*i.e.* dye sensitization or N, C doping).

An intriguing alternative to TiO_2 modification to harness solar light consists in the use different semiconductor oxide materials with narrow band gap. Since the valence band in such materials is formed only by oxygen orbitals, a good approximation is that in metal oxides with smaller band gap the conduction band becomes more positive in energy. Thus for smaller band gap materials a larger overpotential is required to increase the photopromoted electrons and drive H^+ reduction.

Researchers typically try to increase the reaction efficiency focusing on attaining higher photocurrents in terms of mA cm^{-2}, under light conditions closest to the real AM1.5G solar irradiation both for power density (100 mW cm^{-2}) and spectral composition (Xe lamp equipped with an AM1.5G filter), see Figure 1.2 for the standard solar irradiance spectra. Since the need of an applied bias, customarily scientists report photocurrents at the water oxidation potential, 1.23 V vs RHE. Because with such potential direct electrolysis does not proceed, the current observed can be thought as the oxidation gain due two light assisted oxidation.

Tungsten trioxide has been reported as a possible alternative to TiO_2, shortly after the first demonstration of the photocatalytic properties of the latter material.[5] WO_3 has a 2.6 - 2.8 eV band gap that allows harvesting 6% of the solar spectrum and consequently potential photocurrents of 3-4.5 mA cm^{-2}. WO_3 has been extensively studied, though not as well TiO_2, and many groups developed synthetic routes to obtain optimized photoanodes. This material in the monoclinic structure showed excellent solar-to-chemical efficiency mainly because of its high charge conduction properties and long lived charge

carriers. Trapped electrons in W^{5+} are stable from minutes to hours even in air and the hole counterpart benefices of such long lifetime.

Augustynski and co-workers were between the first to optimize the solution-based synthesis of photoanodes allowing incident photon to current efficiency (IPCE) amongst the highest reported so far.[6] The optimized photoanode has 90% IPCE at 400 nm in 3M H_2SO_4 and a tale extending in the visible up to 470 nm. Such electrode produces stable photocurrents of 3.0 mA cm^{-2} close to the limit of the material and allowing a solar to hydrogen efficiency of 3.0% (1 cm^2 of photoanode surface under AM 1.5G irradiation leads to a corresponding H_2 cogeneration at the counter electrode of ca. 50 μmol of H_2 per hour or 0.5 mol_{H2} h^{-1} m^{-2}). Metal oxide materials have usually low absorption coefficients hence complete light absorption can be achieved only with micrometer thick films. The synthetic route adopted by Augunstynski's group allows the attainment of thick semi-transparent films that show the optimized photocurrent for a 2.5 μm thickness. On the other hand film thickness is limited by charge carrier mobility. While the mobility of photoexcited electrons is excellent in WO_3, hole diffusion is an issue. In WO_3 hole diffusion distance is only 0.15 μm; this limitation is attenuated in porous films because particle grains size does not exceed the hole diffusion length.[7] In that way holes generated in the bulk can diffuse to the surface trapping sites. Moreover the porous architecture allows the solution to completely feel the film. The reported efficiency is close to the limit of the material, suggesting that further developments are limited.

More recently researches started to examine and to exploit $BiVO_4$ in PEC water oxidation. Monoclinic scheelite face $BiVO_4$ has an E_g of 2.4 eV.[8] Its band gap is defined by the O_{2p} and Bi_{6s} orbitals for the CB, while its VB is assigned to the hybridization between O_{2p} and V_{3d} orbitals.[9] This material could potentially reach photocurrents up to 6–7 mA

cm^{-2} and conversion efficiency up to 9% of the solar spectrum. Nevertheless $BiVO_4$ activity as photoanode has been reported only in 1999.[10] The massive research boosted quickly its performances and, only after 15 years of investigation, photoanodes showing activities close to its limit have been recently published. Despite the low IPCE initially reported with this material many strategies have been adopted to drive photogenerated charges to efficiently split water. The poor charge carrier mobility is the major problem of such material, doping with positively charged substitutional W and Mo increases the majority carrier mobility (electrons) and leads to IPCE close to 30% between 350 and 450 nm.

Due to the high overpotential for the water oxidation reaction (OER) needed for $BiVO_4$, and more in general for all metal oxides photoanodes, a co-catalyst such as IrO_2 or Co-Pi (cobalt phosphate) and more recently FeOOH/NiOOH, can be loaded at its surface to allow oxygen evolution at lower applied potentials.[11,12] Recently photocurrents up to 4 mA cm^{-2} were achieved with photoanodes obtained with the combination of the described strategies. For example the combination of FeOOH/NiOOH as OER co-catalyst allows a 4.3 mA cm^{-2} current in phosphate buffer under AM1.5G irradiation at 1.23 V vs RHE. A gradient doped $BiVO_4$ photoanode coupled with a doubled junction silicon solar cell led to a stable current of 4.3 mA cm^{-2} (5% solar-to-hydrogen efficiency) without any efficiency loss during 60 minutes under irradiation with AM1.5G in 0.1M potassium phosphate buffer at pH 7.3.[13] The rapid improvement and stabilization of the photoelectrocatalytic properties of this material suggest that also for $BiVO_4$ optimal conditions should be reached in the next few years.

Another successfully approach is coupling with WO_3.[14,15] The two semiconducting materials have band gap position allowing the injection of photoexcited electrons from the CB of $BiVO_4$ to the CB of WO_3 while holes can flow from WO_3 VB to the VB of $BiVO_4$. Most

of the work of the last 18 months of my PhD has been spent on investigating this coupled system, especially focusing on its charge carriers dynamics. In Chapters 6 and 7 a detailed description can be found of such system and the results of the above mentioned investigations.

Iron oxide (α-Fe_2O_3) is one of the most interesting photoanode material.[16] The hematite 2.1 eV E_g is very interesting for scientists because it corresponds to a maximum solar-to-hydrogen efficiency of 15%, that is exceeding the lower limit of 10% for widespread commercialization. Iron abundance and global distribution, as well its extreme stability under harsh basic pH condition, make this material a good candidate. On the other hand low mobility (10^{-2} – 10^{-1} cm^2 V^{-1} $s^{-1}$and short hole diffusion length (2 - 4 nm or 20 nm) highly limit the conversion efficiency in this material.[2] Moreover such low minority carriers diffusion length preclude the possibility to have thick Fe_2O_3 films unless with particles grain size of *ca.* 10 nm.

Hardee and Bard in 1976 were the first to report the use of Fe_2O_3 as photoanode,[17] but decent photocurrents have been attained only during the last 10 years, thanks to the development of new gas-phase synthetic routes,[18] of nanostructuring, [19] of Nb and Al doping,[20] of the use of underlayers[21] or surface passivation[22] and lastly of the surface deposition of OER catalysts.[23] Despite so many efforts (Fe_2O_3 is the second photocatalytic oxide material studied after TiO_2 on the basis of the number of paper published) the best performing hematite photoanode reported so far showed a photocurrent exceeding only 3.0 mA cm^{-2}. This report is dated 2010.[24] No more substantial improvement has been reported to date, showing how the low minority charge carrier mobility severely limits the obtainment of higher solar light conversion efficiencies.

Tantalum oxynitride, TaON, is a quite recent material that gained attention among the researchers in the PEC field because of its 2.5 eV band gap (corresponding to the absorption up to 500 nm).[25] This material is a great example of the extension to other oxides (*i.e.* Ta_2O_5) of the strategy to achieve band gap narrowing through intra-bandgap nitrogen doping, originally developed for TiO_2. The presence of structural nitrogen is also the weak point of TaON, because during irradiation oxygen evolution could lead to the exchange of N-doping atoms with oxygen atoms and lead to Ta_2O_5 (that is inactive under visible light). The deposition of catalysts for OER reaction prevents the short term loss of nitrogen but long term durability has not been achieved yet.

Tantalum nitride Ta_3N_5 is one of the only non oxide materials used for such application. Its band gap of ~ 2.1 eV is very promising and allows light conversion up to 590 nm. Moreover, its stability is better than that of TaON.[26] Recently, a record photocurrent of ~ 7.0 mA cm^{-2} with a 1.23 V vs RHE applied bias has been reported using a barium doped Ta_3N_5 nanostructured electrode modified with CoPi catalyst for OER.[27] The PEC experiment was carried out under simulated solar light irradiation in contact with a 0.5 M K_2HPO_4 solution adjusted to pH 13 with KOH. Moreover stability tests on this material over 20 minutes irradiation showed substantially steady photocurrents. Up to now this is one of the best results obtained and a 9% light-to-hydrogen conversion efficiency can be estimated for a tandem cell using a second light absorber photocathode with E_g of 1.9 eV.

In the next Section, the two different tandem cell configurations are presented and a detailed evaluation of the theoretical upper solar-to-hydrogen efficiency is described. Finally the most promising results concerning modern photocathodic materials are reported.

4. D4 TANDEM CELLS AND PHOTOCATHODE MATERIALS

Photoanode metal oxide materials need a large applied bias in order to overcome the overpotential for OER, charge separation and others side reactions. Therefore their utilization in solar harvesting reactions can be seen as counterproductive. However, coupling with a photocathode for H_2 evolution reaction that harvests the complementary portion of the solar spectrum, would avoid the need to apply such large bias. Photocathodes are p-type semiconductors; so when the electrode is immersed in the electrolyte solution, photopromoted electrons (the minority carriers in p-type materials) are driven to the SCLJ at the surface. Here they carry out the water reduction reaction. Majority carriers recombine at the ohmic contact, with electrons coming from the n-type photoanode.

Since it is important to know the maximum expected solar-to-hydrogen efficiency (η_{STH}), the analysis for the S2 and D4 approaches are here reported. For the S2 approach the calculation are quite simple and, by assuming reasonable losses of 1 eV, a band gap of 2.23 eV should be the lowest limit for a semiconductor able to undergo complete water splitting. The maximum efficiency of the S2 approach is therefore 11,6 %.[4]

The double semiconductor approach can be achieved in two ways: with the photoanode and the photocathode coupled side-by-side and in a tandem configuration with the two half-cell placed one on top of the other. The first D4 approach has evidently lower η_{STH} respect to the second, because coupling the cells side-by-side leads to a net loss in the irradiated area. On the other hand smaller band gap materials can be used because there is not the problem of maximizing light transmission through the first photoanode. With such system, in the upper limit situation, where two 1.4 eV materials are employed, a 16.6%

η_{STH} is predicted. Anyway this conversion efficiency is much better than the 11.6 % η_{STH} allowed through the single semiconductor approach.

The determination of the upper limit for a tandem cell is more complicated because the estimation needs to take in account the absorption of the first photoelectrode and thus the second absorber is limited by this factor. In such approach the two photoelectrodes are placed one in front of the other. The first absorber has energy gap E_{g1} that is larger in energy than the band gap of the second absorber E_{g2} ($E_{g1} > E_{g2}$) in order to allow enough light to reach the second absorber. Of course the first photoelectrode has to be transparent and with minimal scattering losses. For this reason opaque photoelectrodes or nanomaterials grown on non-transparent substrates should be avoided because the light not absorbed by the first absorbed is harvested by the second one. Since most of the photoanode materials have a band gap lager than 2.1 eV, while photocathode semiconductors have narrower band gaps, it seems reasonable that the upper absorber with the larger E_g is the photoanode. Bolton and co-workers plotted the maximum of η_{STH} against E_{g1} and E_{g2}, accounting for realistic losses of 1 eV for each absorber (mainly due to η_{ox} and η_{red} overpotentials and charge separation processes) and considering the solar light spectrum composition (the solar flux, photons $m^{-2}s^{-1}nm^{-1}$).

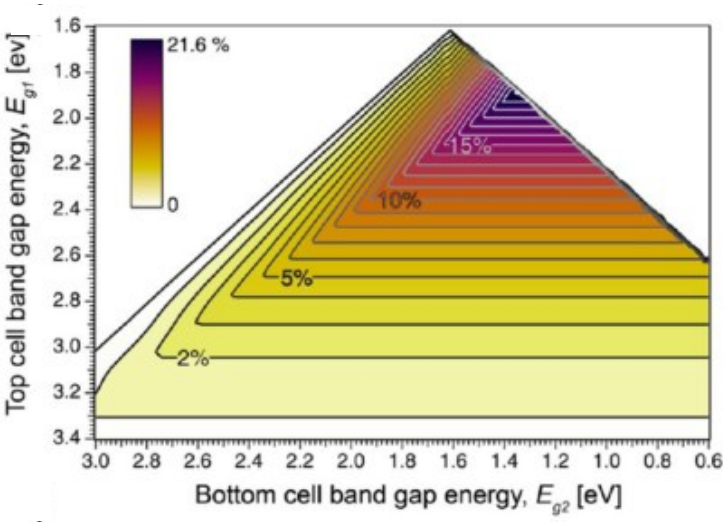

Figure 3.6: Contour plot showing the maximum predicted solar to hydrogen efficiency under AM 1.5G irradiation, total losses of 2.0 eV. The η_{STH} depends on the energy gaps of the two semiconductors.

The resulting contour plot, reported in Figure 3.6, gives a good estimation of the highest η_{STH} efficiency given the band gap of one of the two semiconductors. A limit efficiency of 21.6 % for a value of E_{g1} = 1.89 eV and E_{g2} = 1.34 eV is predicted with the model developed by Bolton.[28]

More recently Lewis and co-workers published a new model including more reliable calculations of the potential losses in the overall cell and found that the limit η_{STH} using materials with of E_{g1} = 1.6 eV and E_{g2} = 0.95 eV is 29.7 %.[29] Anyway if we think that the present alternative is to combine a standard single crystal photovoltaic panel (with efficiency of 12%) with a high pressure electrolyzer (with efficiency 80%), an overall solar-to-hydrogen efficiency of only 9.6% is achievable and a tandem cell with a minimum η_{STH} of 10% is a reasonable target to be reached in the next years.

While the individuation of an oxide photoanodes material for OER with a band gap as narrow as 1.9 or 1.6 eV is still a challenge, different small band gap semiconductors have been studied for the photocathodic reaction. While the first material employed for H_2 evolution was GaP in 1976 (E_g = 2.38 eV), the ideal material should be p-Si with a band gap E_g = 1.12 eV, close the lower limit of E_{g2} = 0.95 eV; its combination with a photoanode with E_{g1} > 2.2 eV allows a η_{STH} of 15%. Furthermore, also for its high abundance and low cost p-Si is today the perfect candidate as photocathode material.

The first study of p-Si for the water reduction reaction has been reported in 1976 and also the successively early studies pointed out the extreme instability of such material in contact with water.[30] A step forward to a greater stability has been done in 1984, when Tsubomura and co-workers reported that phosphor doping of p-Si led to an enhancement in the photostability of the Pt covered photocathode in 3M HBr solution.

More recently stability of p-Si has been improved through nanostructuration and doping. In 2013 a brake through in p-Si stabilization has been achieved by coating the surface with a thin TiO_2 layer.[31] This strategy has been successfully improved and in 2014 Lewis and co-workers reported a record H_2 production efficiency with p-Si covered with a TiO_2 and a NiO layers.[32]

Other narrow band gap photoanode materials have been investigated. Among them p-WSe (E_g = 1.2 eV) led to a 7% efficiency,[33] p-WS_2 (E_g = 1.3 eV) showed 6-7 % conversion efficiency under 50 mW cm^{-2} irradiation at 633 nm in 6 M H_2SO_4.[34] In 1982 InP (E_g = 1.35 eV) passivated by an oxide layer and coated with Rh and Re as co-catalyst has been reported to achieve photoconversion efficiencies of 13,3% and 11,4%, respectively, in 1 M $HClO_4$.[35]

$GaInP_2$ (E_g = 1.83 eV) showed in 1998 the best performance in H_2 production. A monolithic p-n GaAs PV cell connected with a p-$GaInP_2$ photocathode gave a 12.4% conversion efficiency in the overall water splitting reaction, using as electrolyte 3 M H_2SO_4 solution.[36] However such photocathode does not have a sufficient stability and also the cost and scarcity of Ga and As represent two major drawbacks for this material.

CdTe and ZnTe (E_g = 1.5 eV and 2.25 eV) are good candidates especially for their good stability. $CuIn_{1-x}Ga_xSe_2$, CIGS, is an extremely interesting chalcogenide because it offers the possibility to tune the band gap precisely between 1.0 and 1.7 eV by varying the Ga:In ratio. Domen's group reported an optimized cathodic photocurrent of 12 mA cm^{-1} obtained with a CIGS photoelectrode covered with a CdS layer at pH 9.5. Recently p-CIS ($CuInS_2$, E_g = 1.5 eV) was reported to carry out PEC water reduction in acidic media.[37]

Finally, also p-type metal oxides have been studied as photoanode materials. Initially Hardee and Bard showed in 1977 that p-CuO (E_g = 1.35 eV) and p-Bi_2O_3 were able to undergo the cathodic reaction, but stability was the major problem.[38] Also p-Fe_2O_3, p-$CaFe_2O_4$ and p-Cu-Ti-O composite nanotubes showed to be active as cathodic semiconductor under illumination but with poor efficiency. In 2003 Mc Farland's team reported the stabilization of a Cu_2O (E_g = 2.0 eV) with the deposition of a thin n-TiO_2 layer.[39] TiO_2 protects the photocathode material from photocorrosion, probably accepting photoexcited electrons from the higher CB of Cu_2O, without decreasing the performance of the cuprous oxide. This semiconductor is most likely the state of the art metal oxide p-type material, with a record photocurrent as high as 7.6 mA cm^{-2}. This performance has been reported in 2011 for a Cu_2O electrode protected with the atomic layer deposition of Al-doped ZnO and TiO_2 and coated with Pt.[40]

In the next section, the possibility to use a photovoltaic panel, instead of a photocathode, is discussed as well as a small overview of the most promising full assembled tandem devices reported to date.

5. FULL ASSEMBLED D4 TANDEM CELLS

The minor research interest devoted to the improvement of the photocathodic material should also be explained considering the possibility to use a photovoltaic device to generate the potential required to drive the water reduction half reaction. Photopromoted electrons at the PV cell travel to a Pt cathode, where H_2 evolution take place (see Figure 3.7). In the photoanode/photovoltaic cell configuration the current voltage curves of the two photoelectrodes have to cross at the an adequate voltage, the operating potential U_{op}. The photocurrent related to the U_{op} (J_{op}) represents the majority carrier flowing between

the two photoelectrodes (electrons from the n-type photoanode and holes from the p-type photocathode or PV cell).

The solar to hydrogen conversion efficiency in a tandem device is calculated from the following equation

$$\eta_{STH} = \frac{J_{op}\,\Delta G^{\circ}_{H_2}\,\eta_{fard}}{2qE_s}$$

where $\Delta G^{\circ}_{H_2}$ is the standard free energy of the hydrogen produced (2.46 eV per H_2 molecule, considering the lower heating value), η_{fard} is the Faradaic efficiency for the water splitting reaction, q represents the elementary charge (1.6022 10^{-19} C = 1 eV V^{-1} and E_s is the standard solar flux (1kW m^{-2}).[4]

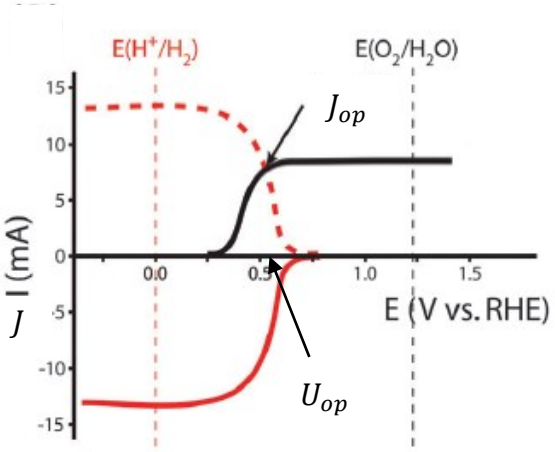

Figure 3.7: Graphical sweep voltammetry analysis for a tandem architecture showing the photocurrent responses of a photoanode (black line, positive current) and a photocathode (red line, negative current). The intersection between the black line and the red dotted line, that is the photocathodic photocurrent changed in sign, gives J_{op}, the bias free operating current.[48]

Because of its low open circuit potential U_{op}, a Si-based device requires a double junction in tandem to produce a potential exceeding μ_{ex} and the two overpotentials η_{ox} and η_{red}. An outstanding recent example is again the gradient-doped W-$BiVO_4$ tandem device reported by Van de Kroel's group, using both a single and a double junction a-Si photovoltaic device.[13] In Figure 3.8a and 3.8b the anodic shift of the U_{op} for the double junction a-Si panel respect to the single PV junction is exemplified, as well as the resultant

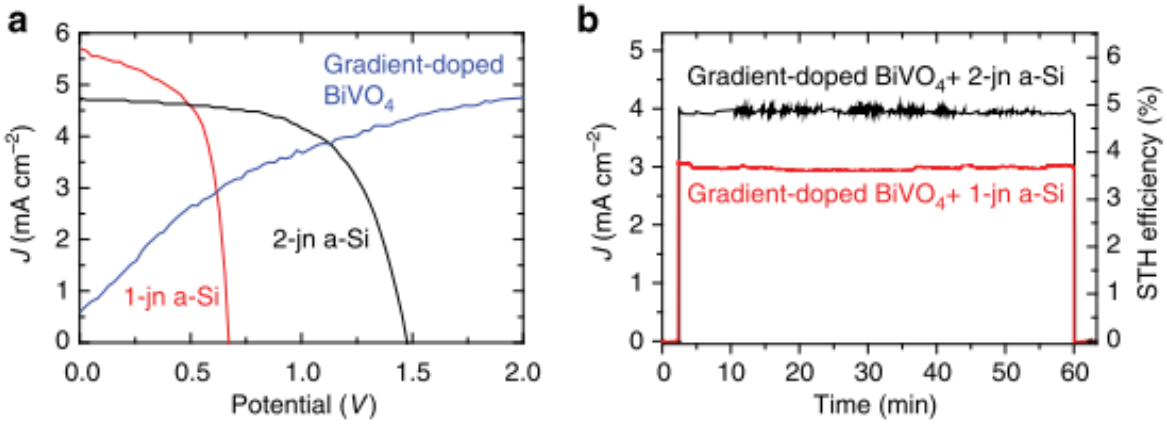

Figure 3.8: a) two electrode AM1.5 sweep voltammetry J-V curve of the gradient doped-$BiVO_4$ photoanode (blue line) and the single junction (red line) and double junction (black line) a-Si solar cells placed behind the photoanode. The intersection between the gradient doped-$BiVO_4$ curve and the J-V curves of the two a-Si cells indicates the operating density current of the fully assembled tandem device. b) The experimental current *vs* time plot for complete tandem assembly with both single and double junction a-Si solar cells. The two photocurrents are in good correlation with those expected from Figure 3.8a.[13]

effect on both J_{op} and η_{STH}. On the other hand using expensive a-Si double junction electrodes is not so economically sustainable. For this reason the combination of state of the art photoanodes with next generation, low cost solar cells represents a natural evolution of the photoanode/PV tandem approach. Grätzel's group has been the first to develop WO_3/DSSC and Fe_2O/DSSC tandem devices. However as for the a-Si PV based tandem device, two DSSC cells in series were necessary to provide a sufficient potential to drive the overall water splitting. A photoanode/2X DSSC device studied by Grätzel and co-workers, with the two DSSC dyes absorbing complementary portions of the solar spectrum, reported to allow 1.36% solar-to-hydrogen efficiency using Fe_2O_3 as photoanode.[41] Unless this value is not so impressive the Fe_2O_3/Squaraine DSSC/Ruthenium-based DSSC trilevel tandem cell, it is a great example of how modern solar cell technology can be flexibly tuned to overcome precise limitations. More recently, a new dye with U_{oc} greater than 1.0 V have been reported. The new dye allowed the

assembly of the first single-DSSC tandem device; WO_3 and Fe_2O_3 have been used as photoanodes (with 3.10 % and 1.17 % η_{STH} respectively).[42]

More recently, after the rise of the perovskite-based solar cell technology, Kamat and co-workers reported the assembly of a $BiVO_4$ tandem assembly for overall water splitting.[43] Perovskite $CH_3NH_3PbI_3$ have a high open circuit voltage, which enable the use of only one photovoltaic cell to produce a sufficient photocurrent density at the U_{op} with $BiVO_4$. Therefore the complete device is simpler than for the photoanode/2X DSSC device described above. The tandem CoPi-$BiVO_4$/perovskite-based PV cell assembly reported a decent 2 mA cm^{-2} photocurrent density corresponding to a 2.5% η_{STH}. However the device performance decreased of 20% after 150 s of AM 1.5G irradiation, probably because of the instability of the perovskite solar cell. Moreover, the presence of lead constitutes a big environmental and safety issue.

As we previously discussed, encouraging examples of photoanode/PV cell have been reported. On the other hand few photoanode/photocathode devices have been published, probably because a stable material for water reduction has not yet been found. Very recently an overall tandem cell using n-$BiVO_4$ as photoanode and p-Cu_2O as photocathode has been described.[44] Unless it is the first demonstration of such photoelectrode combination, the promising photocurrent of ~ 1 mA cm^{-2}, obtained with the optimized $BiVO_4$ thickness and using CoPi as OER catalyst, quickly decreases of more than 60% of the initial value after 100 s. A tandem device using W/Mo-doped $BiVO_4$ and $Zn_xCd_{1-x}Se$ has been published in 2013 by Bard's group.[45] The authors studied a cell configuration using two shuttle redox systems (I^-/IO^{3-} and S^{2-}/S_n^{2-}), separated by a proton conductive membrane and in contact with the photoanode (Pt-W/Mo-$BiVO_4$-Pt) and the

photocathode ($Zn_{0.2}Cd_{0.8}Se$-CoS), respectively. However, the overall device led to a conversion of only less than 1% of the irradiation generated by a 150 W Xenon lamp equipped with a 420 nm filter.

Many steps has been done toward economically interesting devices and, furthermore, the research effort seems exponentially increased during the last 15 years. As a matter of fact, many complete tandem water splitting devices showed up in the recent literature,[46] evidencing that the scientific community is becoming ready for succeed in the attainment of the complete device exiting a 10% η_{STH}.

REFERENCES

(1) Nozik, A. J.; Memming, R. Physical Chemistry of Semiconductor−Liquid Interfaces. *J. Phys. Chem.* **1996**, *100*, 13061–13078.

(2) Dotan, H.; Sivula, K.; Grätzel, M.; Rothschild, A.; Warren, S. C. Probing the Photoelectrochemical Properties of Hematite (α-Fe_2O_3) Electrodes Using Hydrogen Peroxide as a Hole Scavenger. *Energy Environ. Sci.* **2011**, *4*, 958.

(3) Zhong, D. K.; Choi, S.; Gamelin, D. R. Near-Complete Suppression of Surface Recombination in Solar Photoelectrolysis by “Co-Pi” Catalyst-Modified W:$BiVO_4$. *J. Am. Chem. Soc.* **2011**, *133*, 18370–18377.

(4) Prévot, M. S.; Sivula, K. Photoelectrochemical Tandem Cells for Solar Water Splitting. *J. Phys. Chem. C* **2013**, *117*, 17879–17893.

(5) Butler, M. A. Photoelectrolysis and Physical Properties of the Semiconducting Electrode WO_2. *J. Appl. Phys.* **1977**, *48*, 1914–1920.

(6) Santato, C.; Odziemkowski, M.; Ulmann, M.; Augustynski, J. Crystallographically Oriented Mesoporous WO_3 Films: Synthesis, Characterization, and Applications. *J. Am. Chem. Soc.* **2001**, *123*, 10639–10649.

(7) Alexander, B. D.; Kulesza, P. J.; Rutkowska, I.; Solarska, R.; Augustynski, J. Metal Oxide Photoanodes for Solar Hydrogen Production. *J. Mater. Chem.* **2008**, *18*, 2298.

(8) Tokunaga, S.; Kato, H.; Kudo, A. Selective Preparation of Monoclinic and Tetragonal $BiVO_4$ with Scheelite Structure and Their Photocatalytic Properties. *Chem. Mater.* **2001**, *13*, 4624–4628.

(9) Cooper, J. K.; Gul, S.; Toma, F. M.; Chen, L.; Glans, P.-A.; Guo, J.; Ager, J. W.; Yano, J.; Sharp, I. D. Electronic Structure of Monoclinic $BiVO_4$. *Chem. Mater.* **2014**, *26*, 5365–5373.

(10) Kudo, A.; Omori, K.; Kato, H. A Novel Aqueous Process for Preparation of Crystal Form-Controlled and Highly Crystalline $BiVO_4$ Powder from Layered Vanadates at Room Temperature and Its Photocatalytic and Photophysical Properties. *J. Am. Chem. Soc.* **1999**, *121*, 11459–11467.

(11) Kim, T. W.; Choi, K.-S. Nanoporous $BiVO_4$ Photoanodes with Dual-Layer Oxygen Evolution Catalysts for Solar Water Splitting. *Science* **2014**, *343*, 990–994.

(12) Seabold, J. A.; Choi, K.-S. Efficient and Stable Photo-Oxidation of Water by a Bismuth Vanadate Photoanode Coupled with an Iron Oxyhydroxide Oxygen Evolution Catalyst. *J. Am. Chem. Soc.* **2012**, *134*, 2186–2192.

(13) Abdi, F. F.; Han, L.; Smets, A. H. M.; Zeman, M.; Dam, B.; Van de Krol, R. Efficient Solar Water Splitting by Enhanced Charge Separation in a Bismuth Vanadate-Silicon Tandem Photoelectrode. *Nat. Commun.* **2013**, *4*, 2195.

(14) Su, J.; Guo, L.; Bao, N.; Grimes, C. A. Nanostructured $WO_3/BiVO_4$ Heterojunction Films for Efficient Photoelectrochemical Water Splitting. *Nano Lett.* **2011**, *11*, 1928–1933.

(15) Hong, S. J.; Lee, S.; Jang, J. S.; Lee, J. S. Heterojunction $BiVO_4/WO_3$ Electrodes for Enhanced Photoactivity of Water Oxidation. *Energy Environ. Sci.* **2011**, *4*, 1781–1787.

(16) Bora, D. K.; Braun, A.; Constable, E. C. “In Rust We Trust”. Hematite - the Prospective Inorganic Backbone for Artificial Photosynthesis. *Energy Environ. Sci.* **2013**, *6*, 407.

(17) Kohl, P. A.; Bard, A. J. Semiconductor Electrodes. *J. Electrochem. Soc.* **1979**, *126*, 59–67.

(18) Kay, A.; Cesar, I.; Grätzel, M. New Benchmark for Water Photooxidation by Nanostructured α-Fe_2O_3 Films. *J. Am. Chem. Soc.* **2006**, *128*, 15714–15721.

(19) Sivula, K.; Formal, F. Le; Brillet, J. New Nanostructures Enhance Solar Water Splitting with Hematite. 2–4.

(20) Souza, F. L.; Lopes, K. P.; Nascente, P. a. P.; Leite, E. R. Nanostructured Hematite Thin Films Produced by Spin-Coating Deposition Solution: Application in Water Splitting. *Sol. Energy Mater. Sol. Cells* **2009**, *93*, 362–368.

(21) Steier, L.; Herraiz-Cardona, I.; Gimenez, S.; Fabregat-Santiago, F.; Bisquert, J.; Tilley, S. D.; Grätzel, M. Understanding the Role of Underlayers and Overlayers in Thin Film Hematite Photoanodes. *Adv. Funct. Mater.* **2014**, *24*, 7681–7688.

(22) Liu, R.; Zheng, Z.; Spurgeon, J.; Yang, X. Enhanced Photoelectrochemical Water-Splitting Performance of Semiconductors by Surface Passivation Layers. *Energy Environ. Sci.* **2014**, *7*, 2504.

(23) Zhong, D. K.; Cornuz, M.; Sivula, K.; Grätzel, M.; Gamelin, D. R. Photo-Assisted Electrodeposition of Cobalt–phosphate (Co–Pi) Catalyst on Hematite Photoanodes for Solar Water Oxidation. *Energy Environ. Sci.* **2011**, *4*, 1759.

(24) Sivula, K.; Zboril, R.; Formal, F. Le; Robert, R.; Weidenkaff, A.; Tucek, J.; Frydrych, J.; Gra, M. Photoelectrochemical Water Splitting with Mesoporous Hematite Prepared by a Solution-Based Colloidal Approach. *J. Am. Chem. Soc.* **2010**, *132*, 7436–7444.

(25) Abe, R.; Higashi, M.; Domen, K. Facile Fabrication of an Efficient Oxynitride TaON Photoanode for Overall Water Splitting into H_2 and O_2 under Visible Light Irradiation. *J. Am. Chem. Soc.* **2010**, *132*, 11828–11829.

(26) Tabata, M.; Maeda, K.; Higashi, M.; Lu, D.; Takata, T.; Abe, R.; Domen, K. Modified Ta_3N_5 Powder as a Photocatalyst for O_2 Evolution in a Two-Step Water Splitting System with an Iodate/iodide Shuttle Redox Mediator under Visible Light. *Langmuir* **2010**, *26*, 9161–9165.

(27) Li, Y.; Zhang, L.; Torres-Pardo, A.; González-Calbet, J. M.; Ma, Y.; Oleynikov, P.; Terasaki, O.; Asahina, S.; Shima, M.; Cha, D.; et al. Cobalt Phosphate-Modified Barium-Doped Tantalum Nitride Nanorod Photoanode with 1.5% Solar Energy Conversion Efficiency. *Nat. Commun.* **2013**, *4*, 2566.

(28) Bolton, J. R. Solar Photoproduction of Hydrogen: A Review. *Sol. Energy* **1996**, *57*, 37–50.

(29) Hu, S.; Xiang, C.; Haussener, S.; Berger, A. D.; Lewis, N. S. An Analysis of the Optimal Band Gaps of Light Absorbers in Integrated Tandem Photoelectrochemical Water-Splitting Systems. *Energy Environ. Sci.* **2013**, *6*, 2984.

(30) Candea, R. M.; Kastner, M.; Goodman, R.; Hickok, N. Photoelectrolysis of Water: Si in Salt Water. *J. Appl. Phys.* **1976**, *47*, 2724–2726.

(31) Smith, R. D. L.; Prévot, M. S.; Fagan, R. D.; Zhang, Z.; Sedach, P. a; Siu, M. K. J.; Trudel, S.; Berlinguette, C. P. Photochemical Route for Accessing Amorphous Metal Oxide Materials for Water Oxidation Catalysis. *Science* **2013**, *340*, 60–63.

(32) Hu, S.; Shaner, M. R.; Beardslee, J. A.; Lichterman, M.; Brunschwig, B. S.; Lewis, N. S. Amorphous TiO_2 Coatings Stabilize Si, GaAs, and GaP Photoanodes for Efficient Water Oxidation. *Science (80-.).* **2014**, *344*, 1005–1009.

(33) McKone, J. R.; Pieterick, A. P.; Gray, H. B.; Lewis, N. S. Hydrogen Evolution from Pt/Ru-Coated P-Type WSe2 Photocathodes. *J. Am. Chem. Soc.* **2013**, *135*, 223–231.

(34) Baglio, J. A.; Calabrese, G. S.; Harrison, D. J. Electrochemical Characterization of P-Type Semiconducting Tungsten Disulfide Photocathodes: Efficient Photoreduction Processes at Semiconductor/liquid Electrolyte Interfaces. *J. Am. Chem. Soc.* **1983**, *105*, 2246–2256.

(35) Aharon-Shalom, E.; Heller, A. Efficient p-InP (Rh-H Alloy) and p-InP (Re-H Alloy) Hydrogen Evolving Photocathodes. *J. Electrochem. Soc.* **1982**, *129*, 2865–2866.

(36) Khaselev, O. Electrochemical Stability of P-$GaInP_2$ in Aqueous Electrolytes Toward Photoelectrochemical Water Splitting. *J. Electrochem. Soc.* **1998**, *145*, 3335.

(37) Yokoyama, D.; Minegishi, T.; Maeda, K.; Katayama, M.; Kubota, J.; Yamada, A.; Konagai, M.; Domen, K. Photoelectrochemical Water Splitting Using a Cu(In,Ga)Se_2 Thin Film. *Electrochem. commun.* **2010**, *12*, 851–853.

(38) Hardee, K. L.; Bard, A. J. Semiconductor Electrodes. *J. Electrochem. Soc.* **1976**, *123*, 1024–1026.

(39) Siripala, W.; Ivanovskaya, A.; Jaramillo, T. F.; Baeck, S. H.; McFarland, E. W. A Cu_2O/TiO2 Heterojunction Thin Film Cathode for Photoelectrocatalysis. *Sol. Energy Mater. Sol. Cells* **2003**, *77*, 229–237.

(40) Paracchino, A.; Laporte, V.; Sivula, K.; Grätzel, M.; Thimsen, E. Highly Active Oxide Photocathode for Photoelectrochemical Water Reduction. *Nat. Mater.* **2011**, *10*, 456–461.

(41) Brillet, J.; Cornuz, M.; Formal, F. Le; Yum, J.-H.; Grätzel, M.; Sivula, K. Examining Architectures of Photoanode–photovoltaic Tandem Cells for Solar Water Splitting. *J. Mater. Res.* **2010**, *25*, 17–24.

(42) Kim, H.; Seol, M.; Lee, J.; Yong, K. Highly Efficient Photoelectrochemical Hydrogen Generation Using Hierarchical ZnO/WO_x Nanowires Cosensitized with CdSe/CdS. **2011**, 25429–25436.

(43) Chen, Y.-S.; Manser, J. S.; Kamat, P. V. All Solution-Processed Lead Halide Perovskite-$BiVO_4$ Tandem Assembly for Photolytic Solar Fuels Production. *J. Am. Chem. Soc.* **2015**, *137*, 974–981.

(44) Bornoz, P.; Abdi, F. F.; Tilley, S. D.; Dam, B.; Van De Krol, R.; Graetzel, M.; Sivula, K. A Bismuth Vanadate-Cuprous Oxide Tandem Cell for Overall Solar Water Splitting. *J. Phys. Chem. C* **2014**, *118*, 16959–16966.

(45) Park, H. S.; Lee, H. C.; Leonard, K. C.; Liu, G.; Bard, A. J. Unbiased Photoelectrochemical Water Splitting in Z-Scheme Device Using W/Mo-Doped $BiVO_4$ and $Zn_xCd_{1-x}Se$. *Chemphyschem* **2013**, *14*, 2277–2287.

(46) Ager III, J. W.; Shaner, M.; Walczak, K.; Sharp, I. D.; Ardo, S. Experimental Demonstrations of Spontaneous, Solar-Driven Photoelectrochemical Water Splitting. *Energy Environ. Sci.* **2015**, *2*, 1–3.

(47) Sivula, K. Metal Oxide Photoelectrodes for Solar Fuel Production, Surface Traps, and Catalysis. *J. Phys. Chem. Lett.* **2013**, *4*, 1624–1633.

(48) Bonke, S. A.; Wiechen, M.; MacFarlane, D. R.; Spiccia, L. Renewable Fuels from Concentrated Solar Power: Towards Practical Artificial Photosynthesis. *Energy Environ. Sci.* **2015**, *8*, 2791–2796.

Chapter 4

Pump-probe Transient Absorption Technique as a tool to track the dynamics following photoexcitation

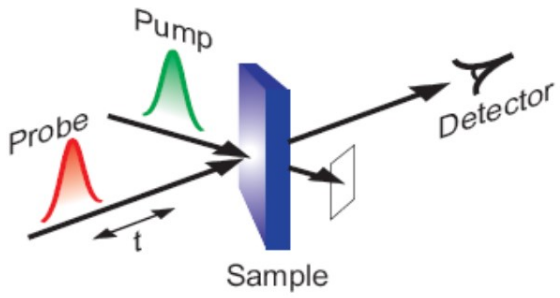

Schme 4.1: simplified scheme for a standard pump and probe experiment.[5]

Many biological photo-induced processes, such as those related to photosynthesis or vision, start with extremely fast structural changes, translation or rotation of portions of a molecule, energy and charge transfer or cleavage or formation of a chemical bond. These individual events take place with short timescales in the range of 10^{-14} or 10^{-12} s, *i.e.* a timescale characteristic of nuclei motion over interatomic distances. The individual steps sum in much longer events, such those involving macromolecules and the interaction between macromolecules. Ultrafast processes, successive to photon absorption, occur also in semiconductor materials used in photovoltaics or as photocatalysts. The exciton evolution, the separation and recombination of photogenerated electron/hole couples, the injection and trapping of electrons and holes, usually take place with sub-ps and ps timescales. The study of such extremely fast processes has been for long time limited by the availability of analytical techniques with adequate time resolution.

Ultrafast optical spectroscopy is a unique tool to directly track the dynamics of such elementary reactions. Since the development of femtosecond laser pulses (early 80s) and especially after the availability of mode-locked Ti:sapphire lasers in the 90s, time-resolved spectroscopy techniques have been employed to follow an increasing number of processes and reactions. More recently, optical parametric amplifiers (OPAs) have been used to extend the wavelength range studied with this technique.[1]

The basic principle of time-resolved femtosecond transient spectroscopy are illustrated in Figure 4.1. In this technique a first intense laser pulse, the so called pump, causes a photoinduced process; then the system evolution is monitored by a delayed weaker probe pulse. The time resolution of the system depends on the widths of the pump and probe pulses. Very short pulses allow the resolution of extremely fast processes (below 1 ps), while for longer processes (longer than 1 ps), pulse compression is not necessary and the 100-200 fs pulse width supplied by mode-locked lasers can be directly employed to generate the two lasers beams. Moreover, both pulses can be tuned in frequency (wavelength) to allow the selective excitation of single optical transitions and the detection over a wide range of the UV-Vis-IR spectrum.

1. PRINCIPLES OF FS-TRANSIENT ABSORPTION SPECTROSCOPY

Pump and probe techniques basically follow the difference in the optical absorption coefficient of a molecular system before pump excitation and after a variable delay, τ. The first energetic pump pulse promotes a fraction of the molecules to their excited state, (the fraction of excited molecules ranges from different tens of percents to 0.1%). The

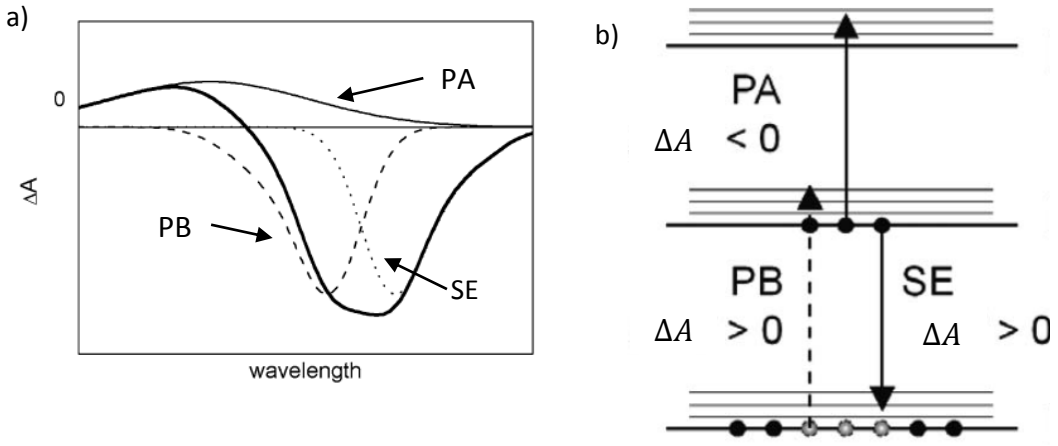

Figure 4.2: a) example of a possible ΔA transient absorption spectrum[14] and b) energy level scheme of a molecular system and its possible transitions, including: photobleaching (PB), stimulated emission (SE) and photoinduced absorption (PA).[1]

ground state population results depleted, while now the first excited state results partially populated. A weak probe pulse, with an intensity not sufficient to excite a large portion of molecules, is sent through the sample with a delay, τ. At the probed wavelengths (λ) a difference absorption can be calculated as

$$\Delta A(\tau, \lambda) = A(\tau, \lambda) - A_0(\lambda)$$

where $A_0(\lambda)$ is the absorbance before pump excitation (absorbance of the sample in its completely relaxed state). The plot of ΔA values at all the wavelengths of the probe pulse gives the transient absorption spectrum (see Figure 4.2a). By varying τ and recording a ΔA spectrum at each time delay, a ΔA profile as a function of time and probe wavelength, *i.e.* a $\Delta A(\tau, \lambda)$ transient absorption dynamic profile, is obtained. $\Delta A(\tau, \lambda)$ contains information on the dynamics of the evolution of the photoexcited system studied.

In general ΔA can be either positive or negative depending on the different processes involved (see Figure 4.2b). The ground state bleaching induces, at wavelengths equal or shorter than the ground state optical transition energy, a negative ΔA signal, the so called induced ground state photobleaching (PB); the absorbance of the excited sample is less than the absorbance before pump excitation because of ground state depopulation. The bleaching signal is always present in transient spectroscopy. A different kind of signal involves the excited state that, after pump excitation, is populated. A probe photon can stimulate the excited state to emit back to the ground state with the overall emission of a photon larger in energy than the pump. This stimulated emission, SE, is responsible of a negative ΔA, because, at the wavelengths emitted through this transition the absorbance after excitation is less than in the ground state. The stimulated emission has a spectral

profile that is Stokes shifted with respect to the ground state photobleaching (at longer wavelengths). This kind of signal is not always observed.

Finally the excited state can absorb some probe photons and be excited to another higher energy level. This photoinduced absorption, PA, leads to a positive ΔA signal, because after pump excitation a new absorption process becomes possible and thus the absorbance results increased. The photoinduced absorbance can occur at any wavelength, depending on the density of states of the studied molecule, and often can overlap with the two negative signals. At difference with respect to photobleaching, both SE and PA absorbance are not always observed.

Pump and probe techniques allow to observe the evolution in time of many photogenerated excited states and determine the dynamics of such transient species. After pump photoexcitation the overall system tends to relax to its original state. The first process occurring is the vibrational relaxation of the excited state to the lowest possible excited level (within a timescale of 10-13 s). Then many different paths are possible. A photoinduced molecule can relax to the ground state losing radiatively the energy stored in the excited state with a typical timescale of 10^{-10}-10^{-8} s; this effect is called photo-luminescence, PL. One positive aspect of time-resolved absorption spectroscopy respect to time-resolved fluorescence is that the first allows the observation also of non-emissive states. Alternatively it can decay non-radiatively to the ground state or to a lower laying state, through an internal conversion (IC) process, and the energy remains localized to the molecule as increased vibrational states. The IC process takes place with even shorter timescales (10^{-13}-10^{-12} s) A slower process, occurring in 10^{-10}-10^{-9} s, is intersystem crossing; in this case the system undergoes a change in its spin multiplicity (for example from a singlet to a triplet state). Other excited state deactivation processes are energy

transfer between an excited molecule (or part of molecule) and a second molecule that simultaneously gets excited, or charge transfer that leads to charge separation.

2. PUMP-PROBE EXPERIMENTAL SETUP

Figure 4.3 reports a scheme of a typical pump-probe apparatus for two-color experiments where pump is monochromatic while the probe is obtained by white light generation. The laser source is a single wavelength femtosecond Ti:sapphire laser (CPA – Ti sapphire 780 nm, 150 fs, at 1 KHz). The incoming beam is divided in two fractions (usually 90-95% and 10-5%) with a beam splitter (BS). The more intense fraction is changed in frequency by means of a second harmonic generator (SHG) or an optical parametric amplifier (OPA). In the first case the fundamental wave is focused in a nonlinear β-Barium Borate crystal and doubled in frequency to 390 nm, in the latter case the OPA allows to obtain a pump of substantially any wavelength over the visible spectrum (this technique is treated shortly in the next section). Successively the pump passes through the optical modulator (chopper), which is set at the same frequency of the laser pulse repetition rate (1 KHz); then the pump is delayed in the delay line and focused to the sample. The less intense laser beam is focused in a thin sapphire plate, with a thickness of 1-2 mm, to generate the white light polychromatic probe. For example a CaF_2 crystal can generate white light extending from

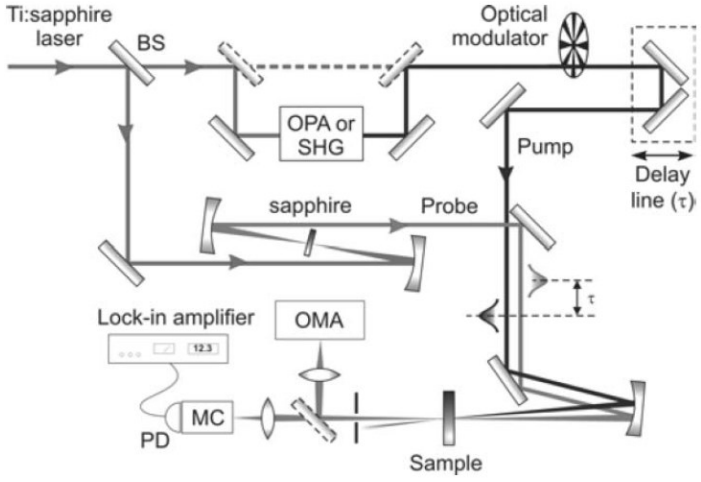

Figure 4.3: femtosecond pump-probe experimental setup for a two colours experiment. The system uses as a pump the first harmonic of the Ti:sapphire laser (dotted path) or the frequency doubled beam or a different frequency selected through the optical paramagnetic amplifier OPA and as a probe the white broadband light beam, obtained through focusing part of the fundamental frequency in a sapphire crystal.[15]

320 nm to 850 nm, while different crystals can extend the probe up to 1600 nm. The white light generation gives rise to the chirp effect: the blue light is generated later with respect to the longer wavelength photons. Therefore the white light is defocused in time. Because different wavelengths travel with different velocity in dense materials (i.e. in the glass of the optics or cuvettes), the chirp readily increases to picoseconds. To prevent chirping effects only reflective optics are used between the point where white light is generated and the sample.

Upon pump excitation, the focalized broadband probe traverses the sample and then its attenuated spectrum is measured by an optical multichannel analyzer (OMA) while other detectors are available for experiments in the near-IR (HgCdTe array) and in the UV. The detector is connected to a computer that records each experiments (500 experiments per second plus 500 blanks per second). More in detail: the optical modulator (chopper) blocks half of the pump shots (500 shots per second get stopped and 500 pass through the chopper), while all the probe pulses reach the sample. Therefore, the sample is alternatively excited and not excited and consequently the probe at the detector alternately corresponds to an excited and unexcited sample. The corresponding ΔA (absorbance of the excited sample minus the absorbance of the unexcited sample) is recorded every 2 ms, 500 times per seconds. In order to decrease the background noise each delay time is averaged for 2 or 3 seconds and so for each delay time the experiment is repeated at least 1000-1500 times.

Moreover, in order to check the sample stability, the test reproducibility and the laser stability and to increase the quality of the measures, several complete scans are repeated and averaged. The collection of successive spectra (100-200), recorded at different delay times, allows the creation of a tridimensional spectrum $\Delta A(\tau, \lambda)$. The ΔA map represents

a massive collection of data (100-200 spectra for hundreds wavelengths) and its rationalization is quite time consuming, especially when the sample is analyzed for the first time and its transient signal is unknown. In order to extract significant information it is possible to take one delay time and look at the transient absorption spectra (the ΔA at the different wavelengths) or one could plot the ΔA evolution for a selected wavelength as a function of the delay time (the so called kinetic trace).

The sensitivity of transient absorption measurements ranges from 10^{-4} to 10^{-6} unit of absorbance depending on the pulse repetition rate (1 kHz and 100 MHz respectively). The temporal resolution is limited by the white light chirp (at least 100 fs) and depends also on the laser pulse width. In order to allow the resolution of optical transitions that occur in shorter timescales, pulse compression and the limitation of the chirp are needed. In order to allow excitation with wavelengths others than the fundamental or second harmonic, the optical parametric amplification (OPA) can be used to obtain pump with tunable frequency.

3. GENERATION OF PUMP WITH DIFFERENT WAVELENGTHS WITH OPTICAL PARAMETRIC RESONANCE AMPLIFICATION

In Figure 4.4a the scheme of a simplified femtosecond pump-probe equipment using OPA is described. The principle of OPA are quite simple: the high intensity, high frequency pump pulse (ω_p) is focused on an appropriate nonlinear crystal and amplify a lower intensity, lower frequency beam (the seed pulse ω_s); a third signal (the idle beam ω_i) is generated as a resultant of the difference in energy between the pump and the seed (see Figure 4.4b for the frequency balance in the OPA process).[2] The seed can be the white light generated in a sapphire plate, in that case the chirp can be used to selectively amplify

a specific wavelength by overlapping in time that wavelength with the pump. The amplified signal is several orders of magnitude more intense than the seed signal and therefore can be focused on the sample and used as a pump or frequency doubled in a nonlinear crystal. The idler is shifted to longer wavelengths respect to the amplified seed pulse and therefore can be used as a tunable pump in the IR region. Using the SH (~ 400 nm) of a Ti:Sapphire laser it is thus possible to amplify the seed signal in the range of 450-800 nm and obtain an idler signal, that can be used as pump pulse, ranging from 800 to 2500 nm.[1]

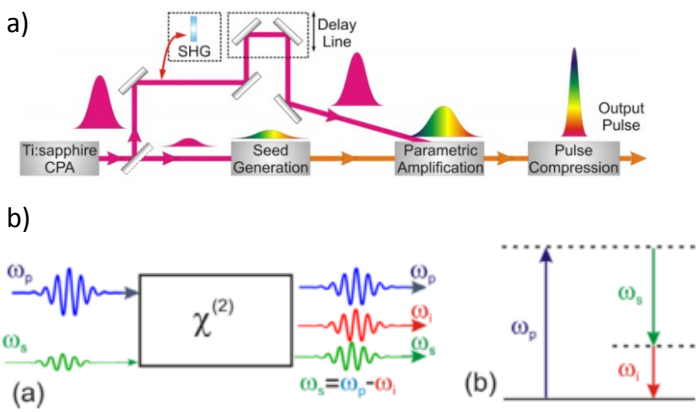

Figure 4.4: a) Schematic femtosecond pump-probe experimental setup using OPA to generate broadband or narrower amplified signal from the fundamental or frequency doubled Ti:sapphire laser beam. Pulse compression of the OPA beam allow shorter pulsewidths b) Scheme of the frequency balance between pump, seed and idler signal in an OPA process.[2]

In a collinear OPA operation condition such as the one described in Figure 4.5b, to avoid the spatial overlap between the idler and the signal it is possible to adopt a non collinear interaction geometry (NOPA). In that way the idler, that is generated with a higher group velocity respect to the amplified signal, and the amplified signals propagate along different directions (see Figure 4.5c). For the optimal pump-seed angle (α = 3.82°) the amplified signal has broadband extending on most of the visible spectrum (see Figure 4.6). On the other hand, pulses with narrower bandwidths can be achieved detuning the pump-signal angle to its optimal value, doing that a still Gaussian dispersed ~ 100 nm broad signal centered at a frequency tunable across the visible range can be obtained.

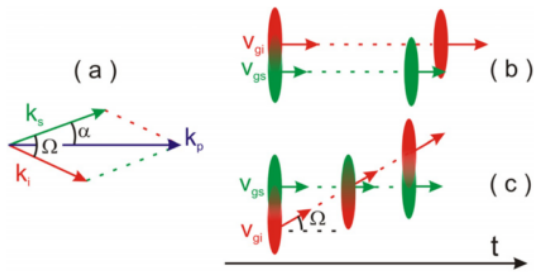

Figure 4.5: a) Phase matching angle between the pump and seed beams and the resultant idler angle in an OPA process. b) representation of the signal and idler pulses in a collinear geometry and c) non-collinear geometry.[2]

After having accurately controlled the different variables in the NOPA (spatial and temporal pump and seed overlap, phase matching and pump-seed angle) the so obtained pulses have a FWHM duration of approximately 70 fs. Therefore, starting from the first harmonic generated by a Ti:Sapphire laser having a 150-200 fs pulse width, through NOPA it is possible to obtain a much shorter pulse. The duration of the pulse is essentially due to the chirp arising from white light generation and the amplification in the BBO crystal. Therefore it is possible to de-chirp the signal using appropriate compression reflective optics. Using prism-grating and prism-chirped mirrors, it is possible to compress the pulse duration and generate 6-7 fs pulse in the broadband visible region (white light probe) and 10-15 fs narrowband pump, covering the visible and IR region (see Figure 4.6). Such high temporally compressed pulses can be employed in high time resolution pump-probe setup and allow to track sub-picosecond processes following light-matter interaction in physics, chemical and biological fields. Few examples of the utilization of such innovative technique are reported in the next section.

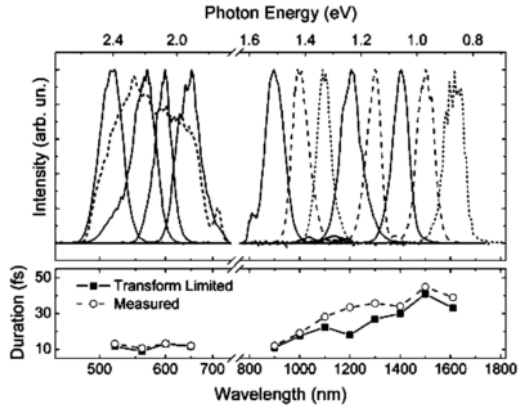

Figure 4.6: Upper panel: broadband amplified signal from an optimized NOPA process (dashed line) and narrower amplified signal centred at different visible frequencies obtained tuning the pump-signal angle. Lower panel: corresponding pulse duration after temporal compression.[15]

4. SOME FS-TAS APPLICATIONS

Pump and probe techniques offer the possibility to study the time evolution of reactions involving light-matter interaction and give the opportunity to understand many fundamental processes occurring in biological systems, organo-metallic and inorganics compounds. This knowledge could be used to further explain more complex phenomena such as the photosynthesis and vision or to drive scientists to design new materials and achieve better results in light energy conversion application such as photovoltaics, photoelectrocatalysis and photocatalysis.

Between the many applications of ultrafast transient absorption spectroscopy, the study of light harvesting complexes in photosynthetic organisms is one of the most exciting. The purpose of these complexes is to absorb sunlight energy and, through a series of thermodynamically allowed energy transfer processes, lead the energy to the reaction center where it is used to photosynthetic reactions. During the evolution, these complexes and their assembly in the overall photosynthetic center, increased their solar energy conversion efficiency. While the overall reaction process (for example CO_2 fixation) occurs in the microsecond-second timescale, the first individual events are extremely fast with time scale even below hundreds of fs. However, such extremely fast charge transfer processes permit, through spatial separation, to avoid early recombination between photogenerated charges and ultimately make possible all the overall, extremely complex, photosynthetic reactions.

Only in recent years pump pulses with duration of 10-20 fs have been available and have been used in transient absorption studies of the excited states of light harvesting organic pigments such as carotenoids and chlorophylls. For example a fs-TAS study comparing the excited states dynamics on rhodopin glucoside (a carotenoid absorbing up to 590 nm)

in benzyl alcohol and embedded in the LH2 complex showed that in the latter case two more relaxation channels are available (with 140 fs and 80 ps time constants). The first process, with an energy transfer efficiency of ~ 50%, allows the delocalization of the excited state from the rhodopin to the bacterio-chlorophyll in the LH2 complex and thus decrease the chance of recombination of the excited states.

Ultrafast transient absorption spectroscopy is also used in the research of new generation photovoltaics. For example P3HT:PCBM based polymeric solar cell, that are emerging for their low production cost and the production of flexible devices, have been widely investigated with such techniques.[3–5] A more recent study pointed out that interfacial charge transfer between the two components is generated in the first tens of fs after photoexcitation and that hot states due to the absorption of photons with an energy excess are beneficial to charge separation.[6] Hot states are more delocalized and therefore are more prone to ultrafast charge separation than fully relaxed species.

Quantum dot nanocrystals has been another family of compound heavily studied through pump and probe spectroscopy.[7] CdSe QDs have a quite simple electronic structure with the first excitonic peak ranging from 450 nm to the deep visible (650 nm for the bulk material) increasing the diameter size respectively from 2.1 nm to 5.6 nm. Moreover the due to the CdSe electronic structure an increase in the band gap reflects only in the shift of the conduction band to more negative energy. For such reasons CdSe QDs have been extremely useful to study the energy dependence of the injection of electrons photoexcited in the QDs conduction band to the conduction band of an appropriate wide band gap semiconducting oxides in quantum dot sensitized solar cells.[8–10] In a recent work Kamat and coworkers measured electron transfer rates from four different sizes of CdSe QDs to three different wide band gap oxides (ZnO, TiO_2 or SnO_2) correlating the

injection rates with the ΔG between the QDs and oxides CB.[11] The trends found agreed with Marcus theory, highlighting the accuracy of such model.

More recently transient absorption techniques has been applied to follow charge carriers dynamics in semiconducting oxide materials employed as photoanodes materials. Hematite is by far the photoanode oxide most studied through fs-TAS.[12,13]

BIBLIOGRAPHY

(1) Cerullo, G.; De Silvestri, S. Ultrafast Optical Parametric Amplifiers. *Rev. Sci. Instrum.* **2003**, *74*, 1–18.

(2) Brida, D.; Manzoni, C.; Cirmi, G.; Marangoni, M.; Bonora, S.; Villoresi, P.; de Silvestri, S.; Cerullo, G. Few-Optical-Cycle Pulses Tunable from the Visible to the Mid-Infrared by Optical Parametric Amplifiers. *J. Opt.* **2009**, *12*, 013001.

(3) Banerji, N.; Bhosale, S. V; Petkova, I.; Langford, S. J.; Vauthey, E. Ultrafast Excited-State Dynamics of Strongly Coupled Porphyrin/core-Substituted-Naphthalenediimide Dyads. *Phys. Chem. Chem. Phys.* **2011**, *13*, 1019–1029.

(4) Banerji, N.; Cowan, S.; Leclerc, M.; Vauthey, E.; Heeger, A. J. Exciton Formation, Relaxation, and Decay in PCDTBT. *J. Am. Chem. Soc.* **2010**, No. 12, 17459–17470.

(5) Raavi, S.; Grancini, G.; Lanzani, G. Transient Absorption Spectroscopic Techniques for Organic Photovoltaics: Tracking the Photogenerated Charges. *Opt. Instrum.* **2012**, No. 1, 3–5.

(6) Grancini, G.; Maiuri, M.; Fazzi, D.; Petrozza, a; Egelhaaf, H.-J.; Brida, D.; Cerullo, G.; Lanzani, G. Hot Exciton Dissociation in Polymer Solar Cells. *Nat. Mater.* **2013**, *12*, 29–33.

(7) Klimov, V.; McBranch, D.; Leatherdale, C.; Bawendi, M. Electron and Hole Relaxation Pathways in Semiconductor Quantum Dots. *Phys. Rev. B* **1999**, *60*, 13740–13749.

(8) Brown, P.; Kamat, P. V. Quantum Dot Solar Cells. Electrophoretic Deposition of CdSe-C60 Composite Films and Capture of Photogenerated Electrons with nC60 Cluster Shell. *J. Am. Chem. Soc.* **2008**, *130*, 8890–8891.

(9) Robel, I.; Kuno, M.; Kamat, P. V. Size-Dependent Electron Injection from Excited CdSe Quantum Dots into TiO_2 Nanoparticles. *J. Am. Chem. Soc.* **2007**, *129*, 4136–4137.

(10) Kongkanand, A.; Tvrdy, K.; Takechi, K.; Kuno, M.; Kamat, P. V. Quantum Dot Solar Cells . Tuning Photoresponse through Size and Shape Control of CdSe - TiO_2 Architecture. *J. Am. Chem. Soc.* **2008**, *130*, 4007–4015.

(11) Tvrdy, K.; Frantsuzov, P. A.; Kamat, P. V. Photoinduced Electron Transfer from Semiconductor Quantum Dots to Metal Oxide Nanoparticles. *Proc. Natl. Acad. Sci. U. S. A.* **2011**, *108*, 29–34.

(12) Cherepy, N. J.; Liston, D. B.; Lovejoy, J. A.; Deng, H.; Zhang, J. Z. Ultrafast Studies of Photoexcited Electron Dynamics in γ- and α-Fe_2O_3 Semiconductor Nanoparticles. *J. Phys. B* **1998**, *102*, 770–776.

(13) Cowan, A. J.; Durrant, J. R. Long-Lived Charge Separated States in Nanostructured Semiconductor Photoelectrodes for the Production of Solar Fuels. *Chem. Soc. Rev.* **2013**, *42*, 2281–2293.

(14) Berera, R.; van Grondelle, R.; Kennis, J. T. M. Ultrafast Transient Absorption Spectroscopy: Principles and Application to Photosynthetic Systems. *Photosynth. Res.* **2009**, *101*, 105–118.

(15) Cerullo, G.; Manzoni, C.; Lüer, L.; Polli, D. Time-Resolved Methods in Biophysics. 4. Broadband Pump–probe Spectroscopy System with Sub-20 fs Temporal Resolution for the Study of Energy Transfer Processes in Photosynthesis. *Photochem. Photobiol. Sci.* **2007**, *6*, 135–144.

Chapter 5

Size-dependent performance of CdSe quantum dots in the photocatalytic evolution of hydrogen under visible light irradiation

ABSTRACT

Nanocrystalline materials are widely employed as photocatalysts for water splitting applications. In particular, cadmium selenide quantum dots (QDs) attracted growing interest for their superior photon to H_2 conversion efficiency and their stability under irradiation. A direct insight is here presented on the effects that CdSe QDs size have on their photoactivity in hydrogen evolution from Na_2SO_3 – containing aqueous solutions under visible light irradiation, based on the results obtained with four highly monodisperse CdSe quantum dots with different nanocrystal diameters, which were synthesized in the present work. After exchange of the capping ligand, each sample was employed as photocatalyst in H_2 production in the absence of any co-catalyst. Their size-dependent photocatalytic activity is discussed considering their absorption properties, their conduction band energy and the recombination probability of the photogenerated charges inside the nanocrystals. High quantum efficiency in H_2 generation results from a balance among these three QDs features, their activity scale being not dominated exclusively by the photocatalyst valence band position.

1. INTRODUCTION

Efficient solar light conversion into fuels, such as H_2 or hydrocarbons, requires the use of photoactive materials combining good visible light absorption properties, suitable band gap energy position and low electron-hole pair recombination. Semiconductor nanocrystals are emerging as effective photocatalysts because of their size and band gap tenability,[1,2] wide range of employed elements,[3–6] high

energy conduction band,[7,8] stability [9–11] and shape control possibility.[12–14] Moreover the combination of different semiconductor materials in nano-heterostructures offers the possibility to host the light absorber, hole acceptor, electron acceptor and co-catalyst in the same nanoparticle.[15–18]

Among all nanostructures, quantum dots (QDs) nanocrystals are by far the most studied in recent years. Because of their high conduction band position, size and band gap tunability, and excellent visible light absorption properties, chalcogenide QDs are amongst the most studied nanostructures for solar energy conversion applications. In particular, cadmium selenide quantum dots, CdSe QDs, have conduction band edges higher in energy than that of TiO_2. Thus, when they are used as photocatalysts, high energy electrons photopromoted in their conduction band are able to produce thermodynamically up-hill reactions, such as CO_2 reduction or hydrogen production from water and/or electron donors.[9,10,19–21] On the other hand, chalcogenide quantum dots can also be employed in combination with wide band gap semiconductor, such as TiO_2 or ZnO, in quantum dot solar cells.[22–24] Electrons photoexcited in the QD conduction band are injected in this case in the conduction band of the semiconductor oxide and used in photovoltaic and photocatalytic applications.[25–27]

Aiming at better understanding the effect of CdSe QDs size on their photoactivity and at determining the optimal nanocrystal size for photocatalytic H_2 production, we synthesized highly monodisperse quantum dots with different size and performed a systematic investigation on their performances in H_2 evolution from aqueous solutions. The experimental results are discussed on the basis of the optical

properties of the photocatalyst nanoparticles, their photocatalytic efficiency scale resulting from an optimized balance of their band gap value, conduction band position and rate of photogenerated charges recombination.

2. Experimental

2.1 Materials

All reagents and solvents, *i.e.* trioctylphosphine (TOP), trioctylphosphine oxide (TOPO), selenium metal powder, cadmium acetate, 3-mercaptopropionic acid (MPA), tetramethylammonium hydroxide pentahydrate, sodium sulphite, toluene, methanol and acetyl acetate, were highest purity chemicals purchased from Sigma Aldrich. Milli-Q grade water was used to prepare aqueous solutions in all experiments.

2.2 Synthesis and characterization of CdSe QDs

CdSe QDs were prepared under nitrogen atmosphere using the synthetic route proposed by Peng et al.,[28] with slight modifications. In a typical synthesis the selenium metal powder (0.117 g) was dissolved at 160 °C in a TOP and toluene mixture (2.90 g and 0.5 g, respectively). Cadmium acetate (0.0726 g) was dissolved in 2.9 g of TOPO at 180 °C. The resulting selenium-containing solution was then added to the Cd precursor-containing solution at 300 °C. In order to prevent multiple nucleation, a Se/Cd stoichiometric excess was employed. The temperature of the so obtained mixture rapidly dropped to *ca.* 270 °C and was maintained at this temperature as long as the desired CdSe nanocrystal size was reached. Once the desired colour (*i.e.* nanocrystals size) was obtained, to crystal growth was

immediately quenched by rapidly pouring the hot solution into a becker containing 30 mL of toluene immersed in an ice bath. The so obtained QDs were then washed three times by precipitating and re-dissolving the nanocrystals in methanol and ethyl acetate.

The TOPO capping the CdSe QDs was exchanged for mercaptopropionic acid (MPA), in order to make the CdSe QDs soluble in protic solvents such as methanol and water. According to a widely employed procedure,[29] MPA was dissolved in methanol and the pH was adjusted to 11 by addition of tetramethylammonium hydroxide. The TOPO-capped QD solutions were thus added to the basic solution. Exchange of the capping ligand takes place immediately. The MPA-capped CdSe QDs were precipitated by adding ethyl acetate and the collected precipitate was washed several times with ethyl acetate to remove residual MPA and TOPO. The so prepared QDs were soluble in protic solvents and were stored in methanol solutions in the dark, before being employed in photocatalytic hydrogen production tests.

The colloidal CdSe QDs suspensions were characterized through UV-Vis absorption measurements employing a Jasco V650 spectrophotometer. The estimation of the QDs size was obtained from the maximum of the first excitonic peak of the QDs using an empirical equation reported by Jasieniak et al.[30] (see Section 2.3 for details). The XRD analysis was performed using a Philips PW1820 with Cu Kα radiation at 40 mA and 40 kV.

2.3 Estimation of QDs particle size and concentration of the colloidal solution

The synthetized colloidal solutions, after capping ligand exchange for mercapto-propionic acid, were characterized through UV-Vis absorption spectroscopy. In order to estimate the nanoparticle size and the concentration of the colloidal solutions a set of empirical relations developed by Jasieniak et al. were employed. The diameter of the QDs was obtained using equation 1, which correlates the energy of the first absorption peak to the size of the QDs.

$$D(nm) = 59.60816 - 0.54736\lambda + 1.8873 \times 10^{-3}\lambda^2 - 2.85743 \times 10^{-6}\lambda^3 + 1.62974 \times 10^{-9}\lambda^4 \quad \text{(Eqn. 1)}$$

Here $D(nm)$ is the QDs diameter and λ is the maximum wavelength of the first excitonic peak.

To calculate the concentration of the QDs solution, we first estimated the band-edge molar extinction coefficient (ϵ_{1S}) using equation 2:

$$\epsilon_{1S}\,(M^{-1}cm^{-1}) = 155507 + 6.67054 \times 10^{13} \exp(-\frac{E_{1S}}{0.10551}) \quad \text{(Eqn. 2)}$$

where E_{1S} is the first absorption peak energy obtained by the Planck law: $\Delta E = hc\lambda^{-1}$. Then we used the so obtained ϵ_{1S} value to calculate the QDs concentration according to equation 3:

$$[QDs]\ (M) = \frac{A_{1S,max}}{l(cm)\varepsilon_{1S}(M^{-1}cm^{-1})} \times \frac{\Delta E_{1S}(eV)}{0.06} \quad \text{(Eqn. 3)}$$

where $A_{1S,max}$ is the absorption maximum of the first absorption peak and *l* is the path length of light through the sample.

2.4 Photocatalytic H_2 production from irradiated QDs in aqueous solution

Photocatalytic activity tests were performed using a bench-scale apparatus connected to a liquid phase recirculating closed system.[31–33] As methanol can notoriously act as an electron donor, it was removed from the stored QDs methanol solutions by drying the nanocrystals employing a vacuum rotary evaporator system (Heidolph Hei-Vap Value, G1) in the dark. Once methanol was completely removed the QDs were dissolved in a 0.1 M Na_2SO_3 aqueous solution.

The so obtained photoactive colloidal suspension (0.003 g of CdSe in 30 mL of 0.1 M Na_2SO_3 aqueous solution) was placed in a 45 mL cylindrical quartz vessel, which was magnetically stirred during the runs. The photoreactor was connected to a closed stainless steel recirculation system, in which an inert gas (N_2) was continuously fluxed by means of a bellow pump (Metal Bellows, MB41E). The gaseous species evolving from the aqueous suspension under irradiation accumulated in the gas phase, which was analyzed on line by sampling at regular time intervals and injection into an Agilent 6890N gas chromatograph (GC), equipped with two capillary columns (MolSieve 5A and HP-Plot Q), a flame ionization detector (FID) and a thermoconductivity detector (TCD). N_2 was used as carrier gas.

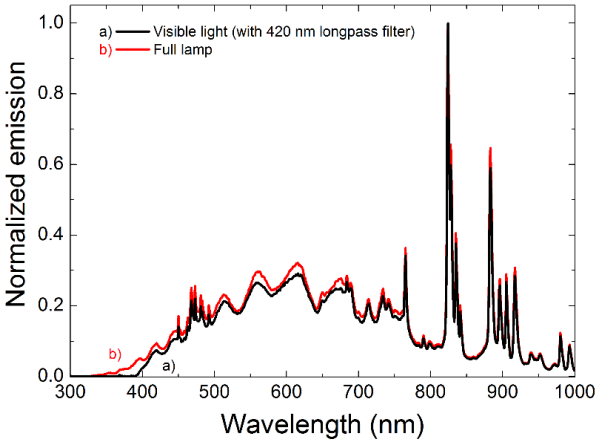

Figure 5.1. Spectra of the emitted photon flux of the xenon lamp, with and without the 20 nm longpass filter.

The GC response was first calibrated by injecting known volumes of H_2 into the recirculation system through a six ways sampling valve.

A Lot Oriel, 300 W xenon lamp (emitting in the 200-1100 nm range) was used as light source. The photon flux was used both as generated by the lamp and after removal of the high energy photons in the UV region by means of a 420 nm longpass filter, hereafter recalled as full and visible light irradiation conditions. The emission spectra of the xenon lamp with and without the filter were collected with a Thorlab CCS200M spectrometer (**see Figure 5.1**). The power intensity of light, measured by means of a Thorlab PM200 power meter equipped with a S130VC power head with Si detector, was 170 W cm^{-2} for the full lamp emission and 160 W cm^{-2} for the filtered visible light emission.

Each QDs solution was tested during three days-long kinetic runs, which were repeated twice, to check reproducibility. The nanocrystals were activated under full lamp irradiation during the first day and then the stability in hydrogen evolution under visible light was tested during the following two days. Prior to the beginning of irradiation, the undesired gaseous species (air on the first day and mainly H_2 on the second and third day) were completely removed by purging the photocatalyst suspension with N_2 for 40 min.

2.5 Evaluation of the quantum efficiencies of the QDs

We evaluated the photocatalytic performance of the here studied four quantum dots samples in terms of their quantum efficiency ϕ. This parameter takes into account the amount of photons absorbed by the colloidal solution and thus describes more rigorously the photon to hydrogen efficiencies showed by the different samples studied. We calculated ϕ from Equation 4

$$\phi = \frac{2\, r_{H_2}\,(mol_{H_2}\, h^{-1})}{r_{ph}\,(mol_{ph}\, h^{-1})} \qquad \text{Eq. 4}$$

r_{H_2} is the photocatalytic H_2 generation rate (the slope of the H_2 accumulation over time) reported in Table 1 and r_{ph} is the photon absorption rate. To calculate the latter parameter we first evaluated the photon flux (the number of photons emitted by the light source per nm^{-1} and cm^{-2}). The total power density of 0.160 W cm^{-2} (P_{tot}) impinging on the sample was obtained combining the measurements made with the Thorlab PM200 power meter equipped with a Si detector with the emission spectra (with intensity in counts nm^{-1}) recorded with the Thorlab CCS200M spectrometer. Using equation 5, we then evaluated P_λ (W nm^{-1} cm^{-2}), the contribution of each wavelength λ to the overall power density

$$P_\lambda = P_{tot}\, \frac{I_\lambda}{I_{\mathrm{tot}}} \qquad \text{Eq. 5}$$

where P_{tot} was multiplied by $\frac{I_\lambda}{I_{\mathrm{tot}}}$, the ratio between the intensity of the emitted light at each wavelength I_λ and the total intensity I_{tot} (namely the contribution of each wavelength on the overall emission).

The photon density emitted by the light source at each wavelength (photons s^{-1} cm^{-2} nm^{-1}) was calculated by dividing P_λ by the photon energy $E_\lambda = h\,\frac{c}{\lambda}$, where *h* is the Planck constant (J s), *c* is the speed of light (m s^{-1}) and λ is the photon wavelength (m). By dividing the number of emitted photons by the Avogadro's number we get the moles of emitted photons and finally we obtain the rate of absorbed photons r_{ph} $(mol_{ph}\ h^{-1})$, by multiplying the moles of emitted photons by (1 – T%), where T% is the transmittance of the QDs solution and with the irradiated surface area (cm^2).

3. RESULTS AND DISCUSSION

3.1 UV-Vis absorption properties of the synthesized QDs

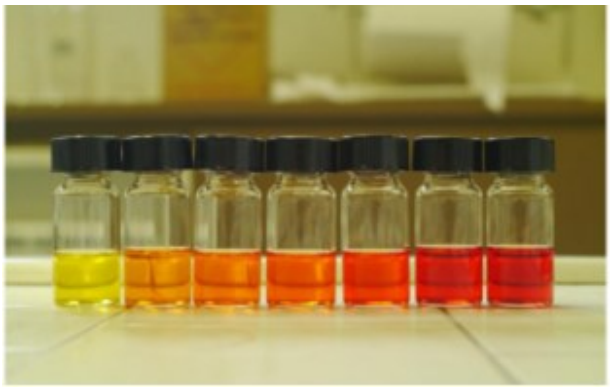

Figure 5.2. Vials containing a series of CdSe QDs of different sizes obtained by taking aliquots of the reactant solution 5, 15, 30, 45, 60, 120, 240 s after the beginning of the crystallization growth (from the left).

CdSe QDs of different sizes were successfully obtained by taking aliquots of the crystallization solution at different times. As shown in Figure 5.2, their color monotonously changed with the ageing time in the hot crystal growth solution.

The UV-Vis absorption properties of the colloidal solutions in methanol of the four CdSe QDs investigated in detail are reported in Figure 5.3. All of them show a sharp and well defined first excitonic peak (with relatively small half width at half maximum) that reflects a narrow size distribution.[34,35] The energy of the first absorption peak increases with decreasing

the QD size.[36] Very useful empirical equations, correlating the absorption maxima of the first excitonic peak to their size, have been reported, which has been profitably employed to calculate the size of CdSe, CdTe and CdS QDs,[30,37] instead of determining them through expensive and time consuming techniques, such as transmission electron microscopy. Thus, the size of the CdSe nanocrystals studied in the present work were found to be 2.5 nm, 2.8 nm, 3.1 nm and 3.4 nm, respectively, using the empirical equations developed by Jasieniak et al.[30], on the basis of their absorption features (Figure 5.3) as described in the next Section.

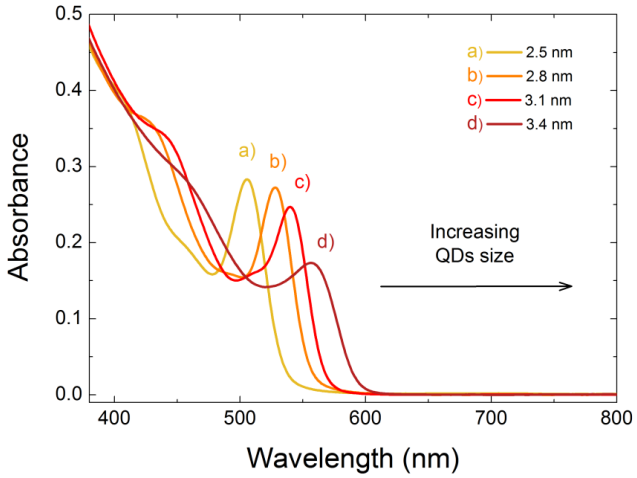

Figure 5.3. UV-Vis absorption spectra of four QDs samples with different nanocrystal size: a) 2.5 nm, b) 2.8 nm C) 3.1 nm and d) 3.4 nm.

3.2 Photocatalytic H_2 production with the four different sized QDs

The photocatalytic tests were carried out in the presence of a hole scavenger as electron donor. Methanol and ethanol are the most widely employed sacrificial reagents for TiO_2 and other wide band gap semiconductor photocatalysts.[38] On the other hand, due to their higher valence band energy, chalcogenides such as CdS and CdSe, maximize their electron transfer properties under irradiation in the presence of electron donors with higher (*i.e.*, less positive) redox potentials.[15,18,39] For instance, ascorbic acid is one of the most popular electron donors employed in the case of CdSe and CdS nanoparticles. In the present investigation photocatalytic

hydrogen evolution tests were performed in aqueous solutions containing 0.1 M Na_2SO_3 as electron donor, because of its higher redox potential (0.17 V *vs.* NHE at pH = 0) and low number of species resulting from its oxidation. Despite its higher redox potential, we avoided the use of sulphide ions, because they were reported to lead to QDs deterioration.[21] Due to the low redox potential of MPA, this capping ligand is not likely to be involved as CdSe QDs hole scavenger in the photocatalytic H_2 evolution reaction.

Figure 5.4 shows the H_2 production results obtained in a typical irradiation test performed with the 2.8 nm-sized nanocrystal sample. Very limited photocatalytic hydrogen production was observed in the first 6 h, although full lamp irradiation was used. This activation period can be attributed to the photodegradation of the MPA capping ligand covering the CdSe QDs and to the removal of metallic selenium, used in excess during the synthesis. Evidence of metallic selenium removal was provided by the formation of a metallic coating on the internal wall of the reactor during the first 6 h irradiation. No significant CO_2 amount was detected by GC analysis during the activation step, in line with the fact that the capping ligand is not expected to be an efficient electron donor. Moreover, the progressive capping ligand decomposition led to a

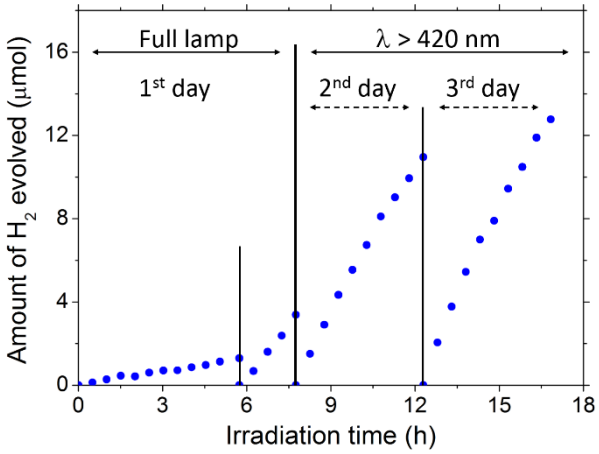

Figure 5.4. Hydrogen evolution in a typical three days long photocatalytic test carried out with 2.8 nm QDs. In the first day, the pre-treatment was performed, consisting in the full lamp irradiation of the photoreactor front for 6 h. Then the photoreactor was turned by 180° and full lamp irradiated for 2 h. Irradiation was continued in the next two days, employing only visible light (λ > 420 nm).

decreased QDs solubility. QDs were found to coalesce in small flakes that tended to sink when stirring was stopped. This did not imply any substantial modification in the crystal structure of QDs, as verified by comparing their XRD patterns measured before and at the end of the photocatalytic test.

In order to verify that the nanocrystals (NCs) did not undergo any irreversible degradation or did not change in size, we compared the XRD patterns measured with fresh 2.8 nm QDs and the NCs recovered by centrifugation from the reaction solution at the end of the photocatalytic test. In **Figure 5.5** we report the XRD analysis of the 2.8 nm sized QDs sample before and after the photocatalytic test (trace a and b, respectively). In the latter case, the NCs were collected from the Na_2SO_3 solution by centrifugation and before, performing the measurement, the sample were washed three times with 40 mL milli-Q water in order to remove any trace of reaction products and of unreacted Na_2SO_3. Both patterns show broad features typical of non-constructive scattering due to the QDs nanometer size28. The highest reflection signal in both samples peaks at 22.8 2θ degree and fits well with CdSe standard card reported in the literature (JCPDS No. 77-2307). Because the XRD pattern of the nanocrystals collected after the photocatalytic test does not show any shift to higher angles and no detectable extra

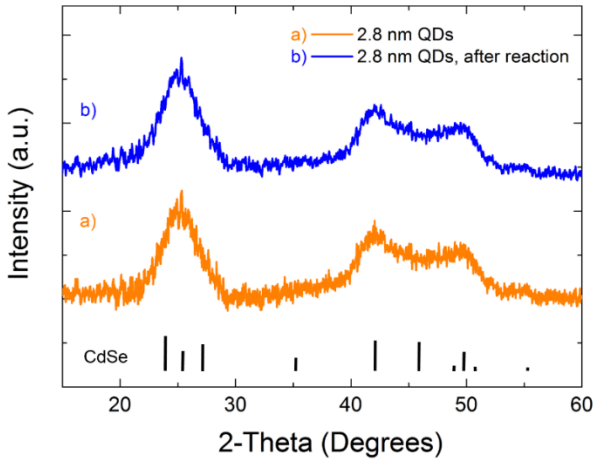

Figure 5.5. XRD patterns of 2.8 nm QDs recorded before and after a full (three days long) photocatalytic

peaks, we rule out the formation of a CdS layer (reference card No. 77-2306) due to the use of a sulfur containing hole scavenger. Moreover, the QDs size seems to be not affected by the prolonged irradiation, as suggested by the similar peak width of the two patterns.

At the end of this activation step the quartz photoreactor was turned by 180° in order to allow full irradiation through the transparent back side of the reactor and the gas species evolved during the pre-treatment were removed by purging the photocatalytic closed system with N_2 for 40 min. No more metallic selenium deposition on the photoreactor inside walls took place in the following irradiation steps. During the last 2 h – long full lamp irradiation performed in the first day the amount of evolved hydrogen increased linearly with time, indicating that successful activation of the QDs was attained.

During the following two days the samples were irradiated with visible light, for 5 h each day. Under these conditions H_2 was found to linearly accumulate in the recirculating gas system under irradiation, evidencing that the CdSe QDs photocatalyst retains its activity also under prolonged irradiation. After the overall 25 h irradiation on the same 2.8 nm QDs solution, 40.3 μmol of H_2 were evolved under the here adopted test conditions. From the extinction coefficient calculated using the set of equations employed to determine the QDs size[30] (see Section 3.2), we estimated the QDs concentration in the reaction solutions and evaluated the photocatalytic performance in terms of turnover number. By considering that the irradiated solution of 2.8 nm QDs contains 0.08 μmol of nanocrystals (or 15.7 μmol of bulk CdSe) a turnover number of ~ 530 hydrogen moles per mole of QD catalyst

(or 2.6 hydrogen moles per CdSe mole) could be evaluated. Clearly, such a high turnover number confirms that H_2 was produced catalytically, without any substantial semiconductor deactivation.

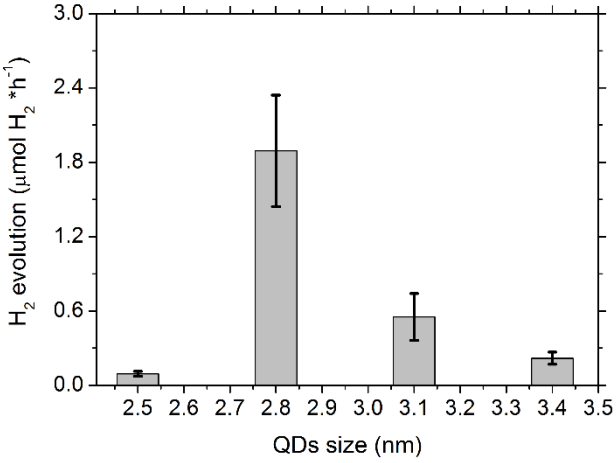

Figure 5.6. Hydrogen evolution rate vs. CdS QDs size.

The same three days-long experiments were carried with the four CdSe QDs samples investigated in detail. All nanocrystal colloidal solutions showed the same activation feature during the first full lamp irradiation day and linear H_2 evolution vs. irradiation time plots in the 5 h-long photocatalytic tests performed in the next two days. The chart reported in Figure 5.6 evidences how the rate of photocatalytic H_2 evolution correlates with the size of the CdSe QDs. The highest hydrogen production rate was obtained with the 2.8 nm sample, that performed far better than both smaller and larger-sized QDs (see Table 1).

Present results can be compared with those obtained with the same experimental set up under similar experimental conditions,[40] employing benchmark TiO_2 P25 photocatalyst from Degussa (Evonik) in contact with water-methanol vapors. A H_2 production rate of 0.61 mmol H_2 h^{-1} g_{cat}^{-1} was obtained[40], which is very similar to the 0.63 mmol H_2 h^{-1} g_{cat}^{-1} obtained in the present work with the 2.8 nm-sized CdSe QDs under full lamp irradiation. However, no hydrogen was produced under visible light irradiation when employing Degussa P25, whereas an only slightly lower H_2 production rate was obtained under visible light only, in the case of CdSe QDs.

Table 1 reports the photodriven H_2 quantum efficiencies (ϕ) calculated from the rates of photocatalytic H_2 generation and the rate of photon absorption, *i.e.* by considering only the number of photons which were effectively absorbed by the CdSe QDs under visible light irradiation. This latter was evaluated by taking into account the emission spectrum of the filtered lamp and the absorption spectrum of the differently sized CdSe QDs, and of course it increased with increasing the QDs size (see Table 1). In fact, larger quantum dots extend their absorption ability deep in the visible region and consequently a larger number of photoexcited charge couples are produced in CdSe QDs under irradiation, with a consequent better exploitation of solar radiation for solar hydrogen production. However, as shown in Table 1, the highest quantum efficiency ϕ of 0.23 % was obtained with the 2.8 nm nanocrystals. This value is in good agreement with previous reports for CdSe QDs employed under similar conditions without using any co-catalyst.[21]

Table 1. Photocatalytic H_2 production rates, absorbed photons and quantum yields obtained with the semiconductors studied.

QDs size (nm)	Absorbed photons[a] (%)	H_2 production rate (μmol H_2 h^{-1})	Quantum efficiency, ϕ[b] (%)
2.5	10.6	0.09 ± 0.02	0.012 ± 0.003
2.8	11.6	1.9 ± 0.7	0.23 ± 0.05
3.1	12.7	0.6 ± 0.2	0.06 ± 0.02
3.4	16.0	0.22 ± 0.05	0.019 + 0.004

[a] Percent amount of absorbed photons over the total number of emitted photons

[b] Quantum efficiency values were calculated from the rates of hydrogen production (moles of H2 per hour) divided by the rate of absorbed photons (moles of photons per hour).

Although the conduction band energy of CdSe QDs decreases with decreasing their size, leading to a higher driving overpotential to carry out the photocatalytic

production of H_2, the smallest–sized CdSe QDs investigated in the present work surprisingly was not the best performing colloidal photocatalyst. This is in contrast with the results obtained by A. Holmes et al.,[21] who found a good correlation between the QDs size and the H_2 evolution rate, with the latter increasing with decreasing the QDs size. In the present work we found that amongst the here investigated four highly monodisperse-sized samples (with diameters in the 2.5-3.4 nm range) the 2.8 nm-sized one was the most active. Although the conduction band lies at an energy higher than those of the other here investigated quantum dots, the smallest-sized sample allowed for the lowest H_2 production rate. The two bigger size colloidal solutions showed intermediate rates, probably also as a consequence of their higher conduction band energies.

The nonlinear dependence of the QDs efficiencies on the nanocrystals size can be explained by taking into account that in small QDs the probability that photogenerated electron-hole pairs recombine is higher than in larger QDs [41]. On the other hand, due to their relatively larger band gap, smaller QDs harvest a smaller portion of the visible spectrum. The best match between relatively low recombination rate, good efficiency in the solar light harvesting and band gap position is attained for 2.8 nm-sized CdSe QDs.

4. CONCLUSIONS

By investigating the size-dependent performance of CdSe QDs in photocatalytic hydrogen evolution under visible light irradiation we found that, after an initial induction period, all samples were able to carry out protons reduction to hydrogen,

with a linear H_2 accumulation *vs.* the irradiation time and no substantial deactivation. The 2.8 nm-sized CdSe nanocrystals showed the highest H_2 production rate with a quantum yield of 0.23% under polychromatic visible irradiation, in the absence of any co-catalyst. Though having a more negative conduction band, *i.e.* a larger overpotential for photocatalytic hydrogen production, smaller 2.4 nm-sized QDs were the least effective here investigated photocatalyst. This may be ascribed mainly to electron-hole recombination, which more readily occurs in smaller-sized QDs, where photoproduced charge carriers are confined in a tight volume. On the other hand, electron-hole recombination is less probable in larger QDs, but their photoactivity may be limited by a less negative conduction band energy position. Therefore larger size nanocrystals such as the 3.1 and 3.4 nm-sized ones showed intermediate photoactivity in hydrogen production.

The 2.8 nm-sized nanocrystals meet all the necessary requirements for exhibiting highest activity, having a lower probability of charge carriers recombination with respect to 2.4 nm QDs, higher conduction band edge than the 3.1 and 3.4 nm QDs and good visible light harvesting properties. We have thus demonstrated that CdSe nanocrystals with this optimal size are able to efficiently drive water reduction to hydrogen by photopromoted conduction band electrons and therefore are excellent candidates to be employed as photocatalysts for H_2 evolution in Z-scheme applications.

REFERENCES

(1) Battaglia, D.; Peng, X. Formation of High Quality InP and InAs Nanocrystals in a Noncoordinating Solvent. *Nano Lett.* **2002**, *2*, 1027–1030.

(2) Jara, D. H.; Yoon, S. J.; Stamplecoskie, K. G.; Kamat, P. V. Size-Dependent Photovoltaic Performance of $CuInS_2$ Quantum Dot-Sensitized Solar Cells. *Chem. Mater.* **2014**, *26*, 7221–7228.

(3) Yu, X.; Shavel, A.; An, X.; Luo, Z.; Cabot, A.; Ibáñez, M. Cu_2ZnSnS_4-Pt and Cu_2ZnSnS_4-Au Heterostructured Nanoparticles for Photocatalytic Water Splitting and Pollutant Degradation. *J. Am. Chem. Soc.* **2014**, *136*, 9236–9239.

(4) Bao, N.; Shen, L.; Takata, T.; Domen, K. Self-Templated Synthesis of Nanoporous CdS Nanostructures for Highly Efficient Photocatalytic Hydrogen Production under Visible Light. *Chem. Mater.* **2008**, *20*, 110–117.

(5) Vogel, R.; Hoyer, P.; Weller, H. Quantum-Sized PbS, CdS, Ag_2S, Sb_2S_3, and Bi_2S_3 Particles as Sensitizers for Various Nanoporous Wide- Bandgap Semiconductors. *J. Phys. Chem.* **1994**, *98*, 3183–3188.

(6) Jin-nouchi, Y.; Hattori, T.; Sumida, Y.; Fujishima, M.; Tada, H. PbS Quantum Dot-Sensitized Photoelectrochemical Cell for Hydrogen Production from Water under Illumination of Simulated Sunlight. *Chemphyschem* **2010**, *11*, 3592–3595.

(7) Robel, I.; Kuno, M.; Kamat, P. V. Size-Dependent Electron Injection from Excited CdSe Quantum Dots into TiO_2 Nanoparticles. *J. Am. Chem. Soc.* **2007**, *129*, 4136–4137.

(8) Tvrdy, K.; Frantsuzov, P. A.; Kamat, P. V. Photoinduced Electron Transfer from Semiconductor Quantum Dots to Metal Oxide Nanoparticles. *Proc. Natl. Acad. Sci. U. S. A.* **2011**, *108*, 29–34.

(9) Han, Z.; Qiu, F.; Eisenberg, R.; Holland, P. L.; Krauss, T. D. Robust Photogeneration of H_2 in Water Using Semiconductor Nanocrystals and a Nickel Catalyst. *Science* **2012**, *338*, 1321–1324.

(10) Wang, G.; Li, Y. Nickel Catalyst Boosts Solar Hydrogen Generation of CdSe Nanocrystals. *ChemCatChem* **2013**, *5*, 1294–1295.

(11) Li, Z.-J.; Wang, J.-J.; Li, X.-B.; Fan, X.-B.; Meng, Q.-Y.; Feng, K.; Chen, B.; Tung, C.-H.; Wu, L.-Z. An Exceptional Artificial Photocatalyst, Ni_h-CdSe/CdS Core/Shell Hybrid, Made In Situ from CdSe Quantum Dots and Nickel Salts for Efficient Hydrogen Evolution. *Adv. Mater.* **2013**, *25*, 6613–6618.

(12) Peng, X.; Manna, L.; Yang, W.; Wickham, J.; Scher, E.; Kadavanich, A.; Alivisatos, A. Shape Control of CdSe Nanocrystals. *Nature* **2000**, *404*, 59–61.

(13) Shieh, F.; Saunders, A. E.; Korgel, B. a. General Shape Control of Colloidal CdS, CdSe, CdTe Quantum Rods and Quantum Rod Heterostructures. *J. Phys. Chem. B* **2005**, *109*, 8538–8542.

(14) Elmalem, E.; Saunders, A. E.; Costi, R.; Salant, A.; Banin, U. Growth of Photocatalytic CdSe-Pt Nanorods and Nanonets. *Adv. Mater.* **2008**, *20*, 4312–4317.

(15) Huang, J.; Mulfort, K. L.; Du, P.; Chen, L. X. Photodriven Charge Separation Dynamics in CdSe/ZnS Core/shell Quantum Dot/cobaloxime Hybrid for Efficient Hydrogen Production. *J. Am. Chem. Soc.* **2012**, *134*, 16472–16475.

(16) Wang, X.; Liu, G.; Wang, L.; Chen, Z.-G.; Lu, G. Q. M.; Cheng, H.-M. ZnO-CdS@Cd Heterostructure for Effective Photocatalytic Hydrogen Generation. *Adv. Energy Mater.* **2012**, *2*, 42–46.

(17) Wang, X.; Liu, G.; Lu, G. Q.; Cheng, H.-M. Stable Photocatalytic Hydrogen Evolution from Water over ZnO–CdS Core–shell Nanorods. *Int. J. Hydrogen Energy* **2010**, *35*, 8199–8205.

(18) Wu, K.; Chen, Z.; Lv, H.; Zhu, H.; Hill, C. L.; Lian, T. Hole Removal Rate Limits Photodriven H_2 Generation Efficiency in CdS-Pt and CdSe/CdS-Pt Semiconductor Nanorod-Metal Tip Heterostructures. *J. Am. Chem. Soc.* **2014**, *136*, 7708–7716.

(19) Frame, F. A.; Carroll, E. C.; Larsen, D. S.; Sarahan, M.; Browning, N. D.; Osterloh, F. E. First Demonstration of CdSe as a Photocatalyst for Hydrogen Evolution from Water under UV and Visible Light. *Chem. Commun.* **2008**, No. 19, 2206–2208.

(20) Bang, J. U.; Lee, S. J.; Jang, J. S.; Choi, W.; Song, H. Geometric Effect of Single or Double Metal-Tipped CdSe Nanorods on Photocatalytic H_2 Generation. *J. Phys. Chem. Lett.* **2012**, *3*, 3781–3785.

(21) Holmes, M. A.; Townsend, T. K.; Osterloh, F. E. Quantum Confinement Controlled Photocatalytic Water Splitting by Suspended CdSe Nanocrystals. *Chem. Commun.* **2012**, *48*, 371–373.

(22) Kamat, P. V. Quantum Dot Solar Cells . The Next Big Thing in Photovoltaics. *J. Phys. Chem. Lett.* **2013**, *4*, 908–918.

(23) Kongkanand, A.; Tvrdy, K.; Takechi, K.; Kuno, M.; Kamat, P. V. Quantum Dot Solar Cells . Tuning Photoresponse through Size and Shape Control of CdSe - TiO_2 Architecture. *J. Am. Chem. Soc.* **2008**, *130*, 4007–4015.

(24) Leschkies, K. S.; Divakar, R.; Basu, J.; Enache-Pommer, E.; Boercker, J. E.; Carter, C. B.; Kortshagen, U. R.; Norris, D. J.; Aydil, E. S. Photosensitization of ZnO Nanowires with CdSe Quantum Dots for Photovoltaic Devices. *Nano Lett.* **2007**, *7*, 1793–1798.

(25) Nguyen, A. T.; Lin, W. H.; Lu, Y. H.; Chiou, Y. De; Hsu, Y. J. First Demonstration of Rainbow Photocatalysts Using Ternary Cd 1-xZnxSe Nanorods of Varying Compositions. *Appl. Catal. A Gen.* **2014**, *476*, 140–147.

(26) Wang, P.; Li, D.; Chen, J.; Zhang, X.; Xian, J.; Yang, X.; Zheng, X.; Li, X.; Shao, Y. A Novel and Green Method to Synthesize CdSe Quantum Dots-Modified TiO_2 and Its Enhanced Visible Light Photocatalytic Activity. *Appl. Catal. B Environ.* **2014**, *160-161*, 217–226.

(27) Zhang, X.; Tang, Y.; Li, Y.; Wang, Y.; Liu, X.; Liu, C.; Luo, S. Reduced Graphene Oxide and PbS Nanoparticles Co-Modified TiO_2 Nanotube Arrays as a Recyclable and Stable Photocatalyst for Efficient Degradation of Pentachlorophenol. *Appl. Catal. A Gen.* **2013**, *457*, 78–84.

(28) Qu, L.; Peng, Z. A.; Peng, X. Alternative Routes toward High Quality CdSe Nanocrystals. *Nano Lett.* **2001**, *1*, 333–337.

(29) Aldana, J.; Wang, Y. A.; Peng, X. Photochemical Instability of CdSe Nanocrystals Coated by Hydrophilic Thiols. *J. Am. Chem. Soc.* **2001**, *123*, 8844–8850.

(30) Jasieniak, J.; Smith, L.; Embden, J. Van; Mulvaney, P.; Califano, M. Re-Examination of the Size-Dependent Absorption Properties of CdSe Quantum Dots. *J. Phys. Chem. C* **2009**, *113*, 19468–19474.

(31) Chiarello, G. L.; Forni, L.; Selli, E. Photocatalytic Hydrogen Production by Liquid- and Gas-Phase Reforming of CH_3OH over Flame-Made TiO_2 and Au/TiO_2. *Catal. Today* **2009**, *144*, 69–74.

(32) Chiarello, G. L.; Dozzi, M. V.; Scavini, M.; Grunwaldt, J.-D.; Selli, E. One Step Flame-Made Fluorinated Pt/TiO_2 Photocatalysts for Hydrogen Production. *Appl. Catal. B Environ.* **2014**, *160-161*, 144–151.

(33) Dozzi, M. V.; Chiarello, G. L.; Selli, E. Effects of Surface Modification and Doping on the Photocatalytic Activity of TiO_2. *J. Adv. Oxid. Technol.* **2010**, *13*, 305–312.

(34) Yu, W. W.; Falkner, J. C.; Shih, B. S.; Colvin, V. L. Preparation and Characterization of Monodisperse PbSe Semiconductor Nanocrystals in a Noncoordinating Solvent. *Chem. Mater.* **2004**, *16*, 3318–3322.

(35) Dai, Q.; Li, D.; Chen, H.; Kan, S.; Li, H.; Gao, S.; Hou, Y.; Liu, B.; Zou, G. Colloidal CdSe Nanocrystals Synthesized in Noncoordinating Solvents with the Addition of a Secondary Ligand: Exceptional Growth Kinetics. *J. Phys. Chem. B* **2006**, *110*, 16508–16513.

(36) Wang, C.; Wang, C.; Shim, M.; Shim, M.; Guyot-Sionnest, P.; Guyot-Sionnest, P. Electrochromic Nanocrystal Quantum Dots. *Science* **2001**, *291*, 2390–2392.

(37) Yu, W. W.; Qu, L.; Guo, W.; Peng, X. Experimental Determination of the Extinction Coefficient of CdTe, CdSe, and CdS Nanocrystals. *Chem. Mater.*

2003, *15*, 2854–2860.

(38) Chiarello, G. L.; Aguirre, M. H.; Selli, E. Hydrogen Production by Photocatalytic Steam Reforming of Methanol on Noble Metal-Modified TiO_2. *J. Catal.* **2010**, *273*, 182–190.

(39) Berr, M. J.; Wagner, P.; Fischbach, S.; Vaneski, A.; Schneider, J.; Susha, A. S.; Rogach, A. L.; Jäckel, F.; Feldmann, J. Hole Scavenger Redox Potentials Determine Quantum Efficiency and Stability of Pt-Decorated CdS Nanorods for Photocatalytic Hydrogen Generation. *Appl. Phys. Lett.* **2012**, *100*, 2013–2016.

(40) Dozzi, M. V.; Saccomanni, A.; Altomare, M.; Selli, E. Photocatalytic Activity of NH4F-Doped TiO_2 Modified by Noble Metal Nanoparticle Deposition. *Photochem. Photobiol. Sci.* **2013**, *12*, 595–601.

(41) Klimov, V.; McBranch, D.; Leatherdale, C.; Bawendi, M. Electron and Hole Relaxation Pathways in Semiconductor Quantum Dots. *Phys. Rev. B* **1999**, *60*, 13740–13749.

Chapter 6

Dynamics of photogenerated charge carriers in $WO_3/BiVO_4$ heterojunction photoanodes

ABSTRACT

Bismuth vanadate ($BiVO_4$) with a band gap of ~2.4 eV has emerged as one of the visible photocatalysts that can absorb light below 520 nm. The electron/hole pairs that are generated following $BiVO_4$ band gap excitation are effective for water splitting, especially when $BiVO_4$ is combined with other metal oxides such as WO_3. The present Chapter deals with the results of a solution processed method employed for designing transparent $WO_3/BiVO_4$ heterojunction electrodes, we observed a synergistic effect on the photoelectrochemical activity of $WO_3/BiVO_4$, with the combined system performing dramatically better than either individual components. Using ultrafast transient absorption spectroscopy the electronic interaction between WO_3 and excited $BiVO_4$ has been elucidated. Moreover, the photocatalytic reduction of thionine by $WO_3/BiVO_4$ as well as by each individual oxide component was used to track electron injection processes and determine the energetics of the studied systems. In the composite $WO_3/BiVO_4$ film a shifted quasi-Fermi level resulted, due to electronic equilibration between the two materials. The better performance of $WO_3/BiVO_4$ heterojunction electrodes was thus found to be consequence of the electron injection from $BiVO_4$ into WO_3, followed by back electron transfer from WO_3 to the holes in $BiVO_4$.

1. INTRODUCTION

Conversion and storage of solar energy in the form of fuels, such as photocatalytic splitting of water to generate hydrogen, have attracted increasing interest during the last two decades.[1,2] Semiconductor materials that are active under visible light[3] and other narrow band gap oxide semiconductors[4,5] have been extensively studied as possible photocatalysts. However, the stability and conversion efficiency that are needed for commercial application have not yet been achieved.

The stability of metal oxides such as $BiVO_4$ and WO_3 over a wide pH range and their ability to absorb high energy visible photons, have attracted the attention of researchers to explore their photocatalytic properties towards the water splitting reaction.[6–8] These two semiconductors have band gaps of ~ 2.7[9] and 2.4[10,11] eV, respectively. Continued efforts to improve the photoelectrochemical performance of these materials have been made through surface modification,[12,13] doping[14,15] or nanostructured morphology,[16–18] as well as by using them in conjunction with oxygen evolution catalysts.[19–21]

Coupling of $BiVO_4$ with WO_3 offers an interesting approach to achieve better charge separation and thus improve the overall performance of the photocatalytic system.[22–25] Type II band alignment in these two semiconductor systems allows electrons from photoexcited $BiVO_4$ to be transferred into WO_3 and holes getting accumulated at $BiVO_4$. The decreased charge carrier recombination in the coupled system ensures better photoelectrochemical properties, similar to the spatial charge separation that occurs in natural photosynthetic systems.[26] Efforts are continuing to achieve photoconversion efficiencies close to the theoretical limit of these two materials.[27] On the other hand, little work was done on understanding the charge carrier dynamics occurring in $BiVO_4$ and the interfacial charge separation in WO_3/$BiVO_4$ heterojunction electrodes.

Transient absorption spectroscopy has been employed to investigate the dynamics of photogenerated holes and electrons in TiO_2, Fe_2O_3, WO_3 and $BiVO_4$ photoanodes. For example, Durrant and co-workers[28–31] found that the application of an anodic bias allows the generation of holes with lifetime on the order of 100 ms to seconds, long enough to allow four-electron water oxidation. Although the dynamics of charge carriers with shorter timescale has been investigated in single oxide electrodes,[32,33] charge separation in coupled systems needs to be explored fully.[34]

In the present Chapter, we describe the results which were obtained by employing femtosecond transient absorption spectroscopy to investigate the electron injection dynamics from photoexcited $BiVO_4$ to WO_3 in the $WO_3/BiVO_4$ coupled system. Transparent WO_3 films were obtained by a citrate-based synthesis, which allowed us to achieve sufficient transparency for spectroscopic investigation. Furthermore, the effective charge separation in the coupled system was also probed through thionine reduction and the estimation of the apparent Fermi level of the photocatalyst assembly.

2. EXPERIMENTAL SECTION

2.1. Materials

The following chemicals were employed: tungsten(VI) ethoxide 99.8% (5% w/v in ethanol), ammonium vanadium oxide, bismuth(III) nitrate pentahydrate ACS 98%, benzyl alcohol ACS 99% (Alpha Aesar); ethyl cellulose (MP Biomedics); poly(vinyl alcohol) >99%, citric acid 99% (Aldrich); glacial acetic acid, anhydrous sodium sulfate and sodium sulphite (Fisher Scientific).

2.2. Photoelectrodes preparation

WO_3 was prepared as follows. 1.0 mL of tungsten ethoxide, 5 wt% in ethanol, was added to 42 mg of citric acid acting as stabilizer. Once citric acid was completely dissolved, benzyl alcohol (0.3 mL) and ethyl cellulose (40 mg) were added to the solution and stirred overnight to allow the complete dissolution of ethyl cellulose. The so obtained paste resulted stable for several weeks. Fluorine-doped tin oxide (FTO) glass (Pilkington Glass, TEC-7, thickness 2 mm) was coated with the paste by spin coating at 6000 rpm for 30 s. Prior to deposition, the FTO glass was cleaned by 30

min-long sonication in a soap solution, in ethanol and finally in water. After coating, the film was dried for 1 h at 80°C and then annealed for 8 h at 500°C.

Bismuth vanadate films were prepared according to a recent literature report.[35] In a typical synthesis, 0.002 mol of $Bi(NO_3)_3$ and NH_4VO_3 were added to 6 mL of HNO_3 23.3% containing 0.004 mol of citric acid. The mixture was stirred overnight to allow dissolution of the precursor. A denser paste was obtained by adding 0.04 g of polyvinyl alcohol and 0.25 mL of acetic acid to 1.0 mL of the above solution. A $BiVO_4$ layer was obtained by spin coating the paste at 4000 rpm for 30 s on clean FTO. The so obtained film was then dried for 1 h at 80°C and annealed for 8 h at 500°C.

The WO_3/$BiVO_4$ combined films were prepared by coating with the $BiVO_4$ dense paste a WO_3 electrode (prepared as described before, dried for 1 h at 80°C and annealed for 1 h at 500°C). Then the composite films underwent the same thermal treatment used for single material films.

2.3. Optical, morphological and photoelectrochemical measurements

Images showing the morphology and the cross section of the electrodes were obtained using a FEI Magellan-400 field emission scanning electron microscope (FESEM). UV-visible absorption spectra were recorded using a Varian Cary 50 Bio spectrophotometer. The crystalline phase of the materials was determined through XRPD analysis using a Philips PW1820 with Cu Kα radiation at 40 mA and 40 kV. Photoelectrochemical (PEC) measurements were carried out using a three electrode cell with an Ag/AgCl (3.0 M NaCl) reference electrode, a platinum gauze as a counter electrode and a Princeton Applied Research 2263 (PARstat) potentiostat. The light source was a 300 W Xe lamp with an AM 1.5G illumination (1 sun). A 0.5 M Na_2SO_4 aqueous solution was used in electrochemical measurements. The potential *vs.*

Ag/AgCl was converted into the RHE scale using the following equation: $E_{RHE} = E_{AgCl} + 0.059\ pH + E^{o}_{AgCl}$, with E^{o}_{AgCl} (3.0 M KCl) = 0.210 V at 25°C.

Incident photon to current efficiency (IPCE) measurements were carried out with a set-up similar to that of PEC experiments, with a Bausch and Lomb grating monochromator placed between the Xe lamp and the sample. A 1.23 V bias *vs.* RHE was applied and the current was measured with a 10 nm step, within the 350 and 600 nm range. The incident light power was measured at each wavelength using a calibrated photodiode connected to a Keithley 617 electrometer. The IPCE was calculated at each wavelength λ (nm) using the following equation:

$$IPCE = \frac{[1240 \times J]}{P_{\lambda} \times \lambda} \times 100$$

where J is the photocurrent density (mA cm^{-2}) and P_{λ} (mW cm^{-2}) is the power of the monochromatic light at λ. All the here reported characterization measurements were performed in the laboratories of Professor Kamat, Radiation Laboratory, Notre Dame University, Indiana (USA).

2.4. Transient absorption spectroscopy

Femtosecond transient absorption spectroscopy was used to follow the early evolution of photogenerated charge carriers in the two separate semiconductors and to track charge transfer in the WO_3/$BiVO_4$ heterojunction. Transient absorption measurements were recorded at the Professor Kamat laboratories in the Radiation Laboratory, Notre Dame University, Indiana (USA) using a system based on a Ti:sapphire laser source (Clark MXR CPA-2010) generating pulses centered at 775 nm with a FWHM of 130 fs and 1 kHz repetition rate. 95% of the laser pulse was frequency doubled to λ = 387 nm and used as pump, while the remaining 5% was

focused on a CaF_2 crystal to generate the white light probe. The detector used was a Helios transient absorption system from Ultrafast Systems. A pump energy density of 40 μJ cm^{-2} was used during all experiments. Transient absorption spectra were recorded within a 1400 ps scale in the 400-800 nm range and fitted with different models discussed in detail in the text.

2.5. Photocatalytic thionine reduction

Monochromatic light at 400 nm and 8 mW intensity was used in thionine (TH) reduction experiments, which were performed at the Professor Kamat Laboratories in the Radiation Laboratory of Notre Dame University, Indiana (USA). The light source was a 200 W Xe lamp equipped with a water filter and a monochromator (the same used for IPCE measurements). The light power intensity was always checked using a Thorlab PM100A power meter with a S120VC photodiode. The irradiated area (30 mm^2) was controlled using an iris. The irradiation wavelength was chosen to minimize TH self-reduction from its excited state. The absorption spectrum of TH has a minimum at 400 nm; on the other hand WO_3 and $BiVO_4$ have similar photoelectrochemical properties in this wavelength region. The films were placed in a 10 mm quartz cuvette containing 5 mL of ethanol and 25 μL of 5 mM TH solution in ethanol. Before starting irradiation, the solution was purged for 2 h with N_2, which was previously saturated with ethanol vapors in order to prevent evaporation of the solvent from the solution in the cuvette.

3. RESULTS AND DISCUSSION

3.1. Characterization of oxide films deposited on transparent electrodes

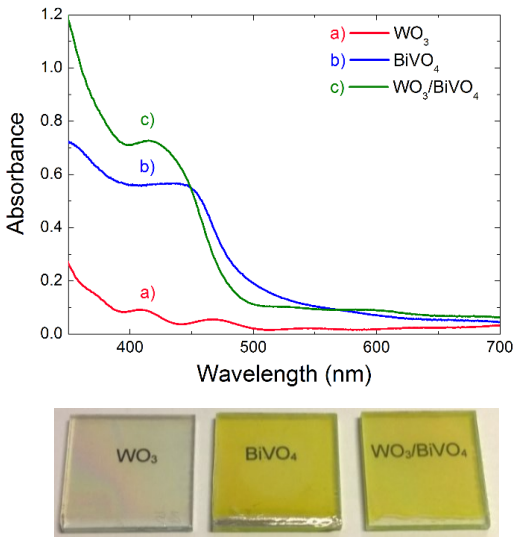

Figure 6.1. Absorption spectra (top) and photographs (bottom) of the oxide films deposited on conducting glass (FTO) electrodes: a) WO_3, b) $BiVO_4$ and c) $WO_3/BiVO_4$ films.

The absorption spectra of the three oxide films that were employed in the investigation reported in the present Chapter are shown in Figure 6.1. The WO_3 film with its band gap of ~ 2.7 eV showed good transparency in the visible. Relatively small absorption was seen below 450 nm. The $BiVO_4$ film and the $WO_3/BiVO_4$ coupled film exhibited an absorption onset around 500 nm (Figure 6.1). Residual absorption was seen above 550 nm, mainly due to light scattering.

These films were further characterized with Scanning Electron Microscopy (SEM). The WO_3 films (top view) is composed of *ca.* 17 nm diameter particles (Figure 6.2A). The cross section analysis (Fig. 6.2C) showed the mesoporous architecture of the WO_3 layer with a thickness of ~ 210 nm. The top view of the $WO_3/BiVO_4$ film in SEM analysis (Figure 6.2B) showed an aggregated network of particles, with morphological features similar to those reported for $BiVO_4$ films earlier.[36] The cross section of the $WO_3/BiVO_4$ coupled film (Figure 6.2D) showed sequential layering of WO_3 and $BiVO_4$. The thickness

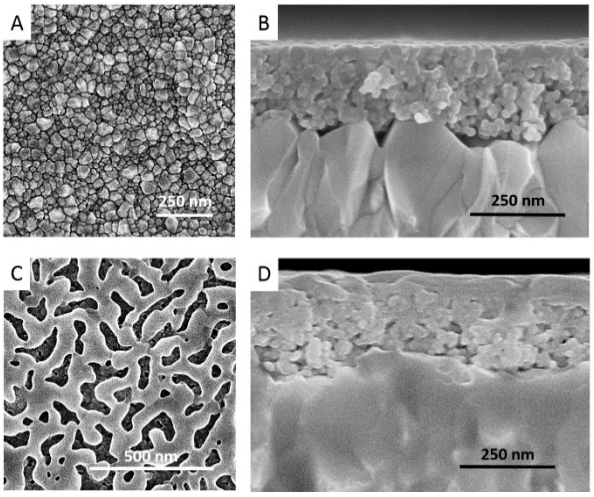

Figure 6.2. FESEM images of (A,C) WO_3 and (B,D) $WO_3/BiVO_4$ films deposited on conducting glass electrodes The images are presented as top view (A,B) and cross sectional view (C,D).

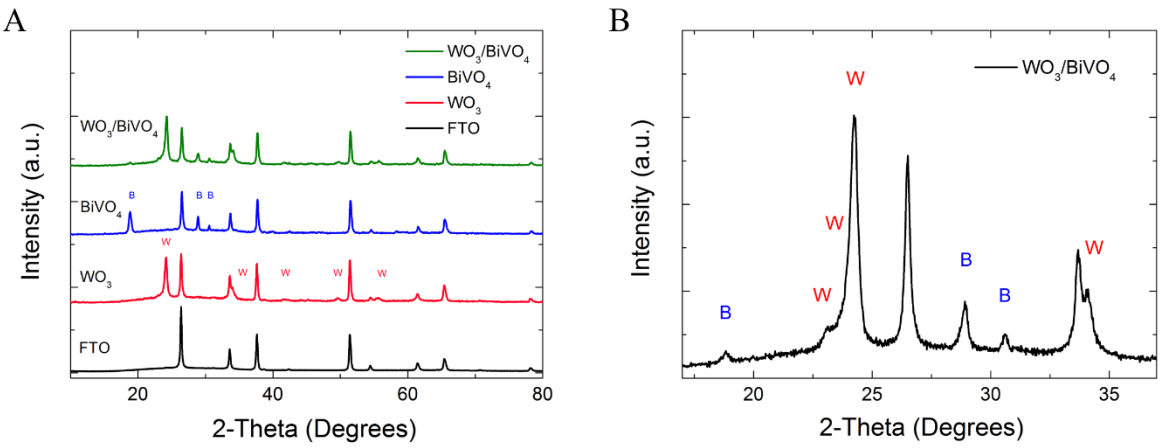

Figure 6.3. (A) XRPD patterns of the materials. From the bottom: FTO glass and WO_3, $BiVO_4$ and $WO_3/BiVO_4$ electrodes on FTO after 8 h annealing at 500°C. (B) Magnification of the XRPD patterns of the composite $WO_3/BiVO_4$ material, exhibiting patterns of both WO_3 and $BiVO_4$, labelled as W and B, respectively.

of $BiVO_4$ in this film was *ca.* 40 nm. The cross section image further ensures that the surface of the underlying WO_3 layer was fully covered by the $BiVO_4$ layer.

In Figure 6.3A the XRPD patterns are reported for the three here investigated films; the diffraction pattern recorded with FTO alone is also shown for comparison. The patterns of both individual materials fit well with monoclinic structures (JCPDS 05-0363 for WO_3 and JCPDS 75-1867 for $BiVO_4$). WO_3 patterns didn't match completely in the 23-25 degrees 2θ region, where the three closely spaced peaks typical of the monoclinic structures overlap. Peak broadening could be probably attributed to non-constructive scattering due to the small crystallite size of the WO_3 film.[37,38] The combined $WO_3/BiVO_4$ electrode showed peaks of both monoclinic materials. The $BiVO_4$ peak at 18.6 degrees was much lower in magnitude with respect to those of single material films (a magnification of the four XRPD patterns in the 17-37 degrees 2θ region is reported in Figure 6.3B). A possible explanation is that the $BiVO_4$ layer grows with a preferential orientation on the underlying WO_3.

3.2. Photoelectrochemical properties of individual and combined films

The photoresponse of the three oxide electrodes was first evaluated in a photoelectrochemical (PEC) cell by employing them individually as a photoanode. The

Pt electrode served as a counter electrode, Ag/AgCl served as reference along with 0.5 M Na_2SO_4 (pH 7) as electrolyte medium. The photoanode was subjected to backside irradiation (through FTO) with AM 1.5G simulated solar light. Both $BiVO_4$ and WO_3 semiconductors were found to be stable at neutral pH and no noticeable degradation was observed during irradiation. The linear sweep voltammetry profiles obtained with the three electrodes under irradiation are shown in Figure 6.4.

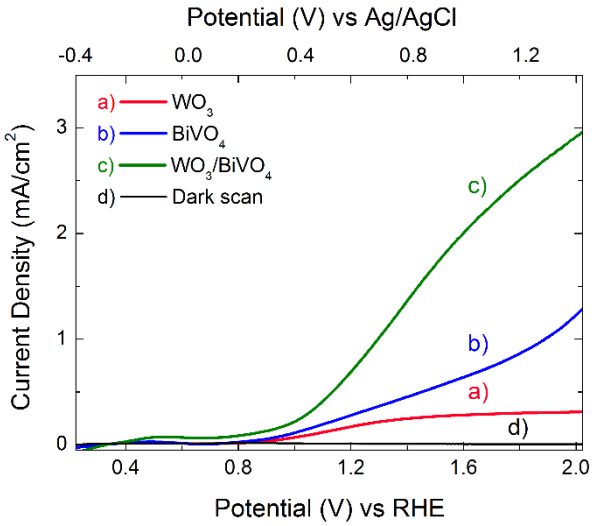

Figure 6.4. Linear sweep voltammetry under AM 1.5G irradiation of the a) WO_3, b) $BiVO_4$ and c) $WO_3/BiVO_4$ photoanodes, recorded in Na_2SO_4 0.5 M aqueous solution, with a scan rate of 10 mV s^{-1}; d) dark current (black line) measured with the $WO_3/BiVO_4$ film.

This figure evidences that the electrodes require an external bias (>1 V *vs*. RHE) to exhibit photocurrent. The photocurrent recorded with the $WO_3/BiVO_4$ electrode was greater than those seen with the two individual WO_3 and $BiVO_4$ electrodes. At 1.23 V (*vs*. RHE) the current density was 0.35 mA cm^{-2} for $BiVO_4$, 0.25 mA cm^{-2} for WO_3 and 1.0 mA cm^{-2} for the $WO_3/BiVO_4$ electrode. At this fixed applied potential, the WO_3 electrode generated slightly lower current than the $BiVO_4$ electrode. Considering that $BiVO_4$ harvests more light than WO_3, since the band gap of $BiVO_4$ is narrower, the WO_3 photoelectrode showed higher efficiency in converting light into current. The low photocurrent generated by the $BiVO_4$ photoanode alone is attributed to the poor charge separation and interfacial charge transfer properties of this semiconductor material.[24]

A significant increase in the photocurrent was obtained when $BiVO_4$ was coupled with WO_3. The enhanced photocurrent of the $WO_3/BiVO_4$ electrode arose from the improved charge separation as the electrons were transferred from $BiVO_4$ to WO_3. The

conduction and valence bands of $BiVO_4$, which are more negative in energy than those of WO_3 (see Scheme 2), facilitate such charge separation. This in turn decreased the recombination rate typical of h^+- e^- couples within $BiVO_4$.[39,40] Similarly, photogenerated holes from excited WO_3 were transferred into the valence band of $BiVO_4$, thus improving the charge separation properties within the $WO_3/BiVO_4$ coupled system.

Figure 6.5 shows the photoresponse of photoanodes measured in terms of IPCE (incident photon to current efficiency) spectra. The photocurrents obtained at different irradiation wavelengths were measured using a three electrodes cell and an applied potential of 1.23 V *vs*. RHE. Individual WO_3 and $BiVO_4$ electrodes exhibit a photocurrent onset at 470 nm and 520 nm, respectively, in line with their absorption spectra (Figure 6.1) and their band gap energy. Despite the higher absorption of the $BiVO_4$ film, the conversion efficiency was lower compared to that of WO_3, in agreement with the results of linear sweep voltammetry experiments (Figure 6.5). The results of both types of measurement confirm that the low photoactivity of $BiVO_4$ is due to the poor charge carrier mobility of this material.[24,39,40] The combined $WO_3/BiVO_4$ electrode possesses the positive characteristics of both single semiconductors, *i.e.* the high conversion efficiency and charge carrier mobility typical of WO_3[41] and the good visible light harvesting properties of $BiVO_4$.

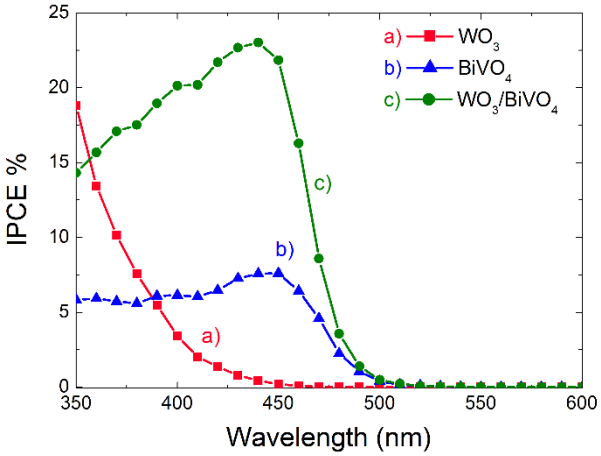

Figure 6.5. Incident photon to current efficiency (IPCE) measured with the a) WO_3, b) $BiVO_4$ and c) WO_3-$BiVO_4$ electrodes, in 0.5 M Na_2SO_4 aqueous solution, at 1.23 V *vs.* RHE.

IPCE measurements were performed under low light intensity (hundreds of μW cm^{-2} nm^{-1}). In order to compare these values with the photocurrents recorded under AM

1.5G conditions in PEC experiments we integrated[42,43] the monochromatic quantum efficiency over the global sunlight spectral irradiance.[44] The integration gave values of 0.22, 0.33 and 0.89 mA cm^{-2} for WO_3, $BiVO_4$ and $WO_3/BiVO_4$ photoanodes, respectively, which are lower than photocurrents measured under simulated solar light irradiation (0.25, 0.35 and 1,0 mA cm^{-2}). With respect to the solar spectrum, the difference can be ascribed to the higher photon flux in the UV region typical of the xenon lamp. On the other hand photogenerated charges undergo the water oxidation reaction efficiently in the studied films also under high light intensity as indicated by the comparable experimental and integrated photocurrent values.

3.3. Estimation of the extinction coefficient of trapped electrons in WO_3 films

The optical properties of trapped electrons in the WO_3 films were evaluated in order to explain why this material does not show any transient species in the time range studied with our fs-TAS experiments. Many works have been published on the electro- and photo-chromic properties of tungsten-based materials. Therefore we initially expected to see a positive absorption feature extending over 450 nm, due to electrons trapped as W^{5+}.[45–48] Moreover transient studies on the μs timescales have also been reported on WO_3 as well as TiO_2 colloidal suspensions and films.[49] However no transient species were detected when carrying out fs-TAS measurements with WO_3 films. Therefore we calculated the extinction coefficient of trapped electrons in WO_3 and we obtained a value comparable to that reported for trapped electrons in TiO_2 or WO_3 colloidal suspensions. However, we found that the buildup of the positive signal due to W^{5+} species is extremely long. For example, in the case of the results shown in Figure 6.6, the sample was irradiated for 6 h with a high photon flux to obtain an absorbance of 0.9 at 800 nm. Therefore, we suggest that the absence of a detectable transient signal in our fs-TAS experiments with WO_3 films is mainly due to the slow

kinetic of electron trapping in the here studied WO_3 films rather than to a small extinction coefficient of W^{5+}.

The extinction coefficient $\epsilon_{W(e^-)}$ of trapped electrons in a blue WO_3 film was calculated using the Lambert Beer equation (eqn 1):

$$A = \epsilon_{W(e^-)} \times C_e \times T \qquad \text{eqn (1)}$$

where C_e is the concentration of trapped electrons in the film and T is the thickness of the film (in cm).

Blue WO_3 was obtained by irradiating a WO_3 20x10 mm film, sealed in a 10 mm cuvette containing 5 mL of ethanol. After purging with N_2 for 2 h the film was irradiated with a 300 W Xe lamp equipped with a 300 nm long pass filter and a water filter. A light power intensity of 250 mW cm^{-2} was used. The light intensity was measured with a PM100A Thorlab power meter equipped with a S302C thermal power sensor. Trapped electrons in WO_3 absorb light in the blue region. The absorption growth under irradiation was monitored by UV-Vis absorption spectroscopy (see Figure 6.6).

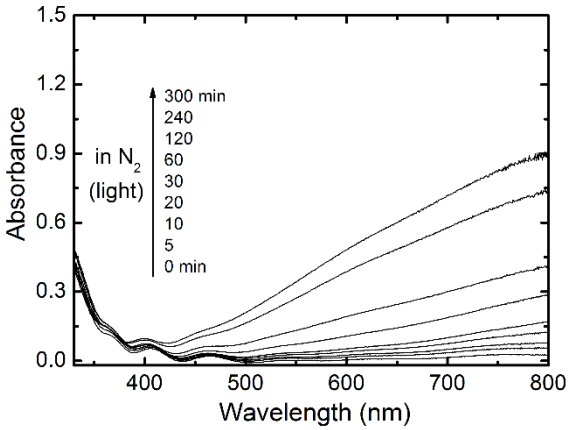

Figure 6.6. Growth of trapped electrons absorption in a WO_3 film under irradiation with light from a 250 W Xe lamp equipped with a 300 nm long pass filter.

Thionine (TH) reduction was used to titrate the electrons stored in the WO_3 film.[50] Reduction of thionine is a two-step reaction that produces the colorless leucothionine product (reaction 1 and 2).

$$2\ WO_3(e^-) + 2\ TH \longrightarrow 2\ WO_3 + 2\ TH^{-\bullet} \qquad \text{reaction 1}$$

$$2\ TH^{-\bullet} \longrightarrow TH^{2-} + TH \qquad \text{reaction 2}$$

The semireduced $TH^{-\cdot}$ dye is metastable and quickly undergoes disproportionation to the colorless leuco form of the dye, TH^{2-}. The blue coloration of TH can be restored after exposure of the reduced colorless form to air.

Reduction of TH over reduced blue WO_3 was performed in the same cuvette after injection of 20 µL of a deaerated 5 mM TH solution in ethanol and was followed by UV-Vis absorption spectroscopy (see Figure 6.7A). The absorption spectra were recorded through the WO_3 film in order to monitor both TH reduction and blue WO_3 bleaching (oxidation of reduced WO_3). Almost complete oxidation of blue WO_3 was obtained after 7 h. At the end of the kinetic test, recovery of the blue TH color was observed after purging with air the bleached solution (containing the reduced colorless TH^{2-} form). The complete TH recovery demonstrates that bleaching was due to the transfer of the electrons stored in blue WO_3 to the dye. Kinetic results of TH bleaching (absorbance monitored at 606 nm) are reported in Figure 6.7B.

An estimation of the number of electrons (n_e) stored in the WO_3 layer was obtained according to the Lambert Beer equation from the amount of reduced TH, by considering that 2 electrons are required to reduce one TH molecule. The amount of reduced TH after 4 h in the dark was calculated by taking into account that the extinction coefficient of TH at 606 nm is ϵ_{TH} = 60000 M^{-1} cm^{-1}, the optical path within

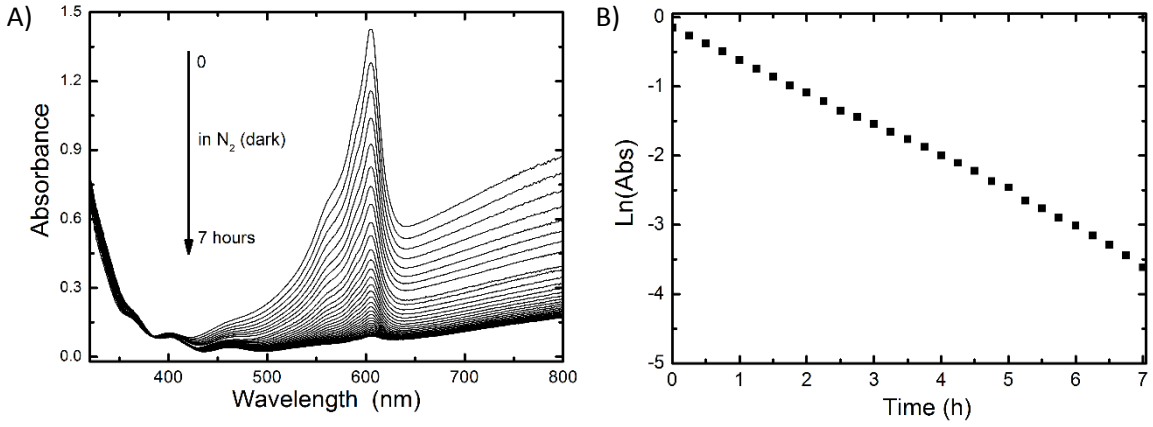

Figure 6.7. TH reduction tests by a reduced blue WO_3 film. A) Absorption spectra recorded with the reduced WO_3 film in contact with a deaerated ethanol TH solution during 7 h-long experiments in the dark. B) Thionine reduction over time, monitored as absorbance decrease at 606 nm.

the solution in the presence of the FTO electrode was 0.78 cm and that an absorbance difference at 606 nm equal to 0.826 was attained in the first 4 h during TH reduction. The concentration of trapped electrons in the film, C_e (mol dm^{-3}), was then obtained from equation 2:

$$C_e = \frac{n_e}{Vol_{film}} = \frac{n_e}{L \times h \times T} \qquad \text{eqn (2)}$$

where L and h are length and height of the WO_3 film, respectively, and T is the thickness of the employed WO_3 film obtained from FESEM measurements (210 nm). From the so obtained C_e value and the ΔA value for the W^{5+} spectra at 800 nm (0.63 attained after 4 h), an extinction coefficient $\epsilon_{W(e^-)}$ of 7300 M^{-1} cm^{-1} at 800 nm was thus estimated for trapped electrons in the blue WO_3 film.

3.4. Transient absorption studies

Transient absorption spectroscopy allowed us to probe the initial charge separation and charge transfer events from the changes in absorption following band gap excitation. This technique has been widely employed to investigate the dynamics of photogenerated charge carriers in photovoltaic,[43,44] photochemical[53] and photoelectrochemical materials. The samples were placed in an evacuated quartz cell and excited at 387 nm by a 130 fs FWHM laser pump pulse with 40 μJ cm^{-2} energy density.

Previous studies revealed that electron trapping in WO_3 colloidal systems occurs rapidly,[46] when subjected to band gap excitation. As already mentioned, no detectable signals were observed in transient absorption experiments with WO_3 films, thus confirming that the 387 nm excitation wavelength is not energetic enough to induce

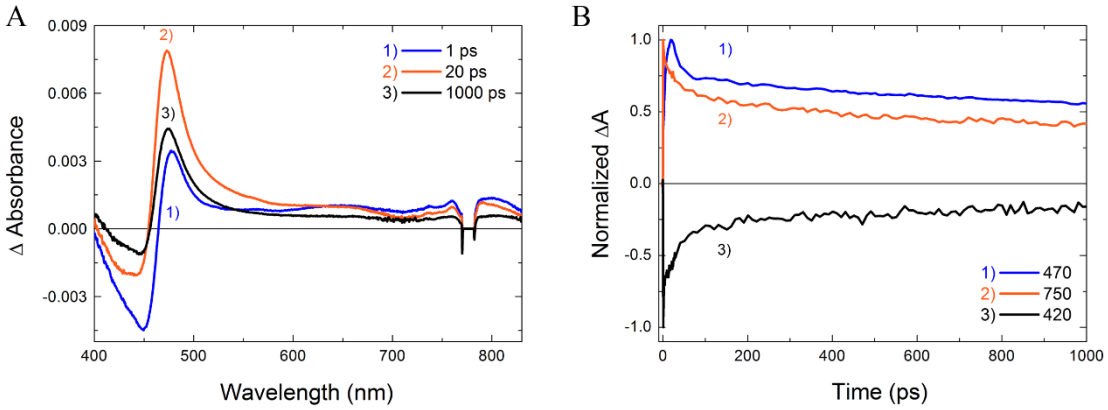

Figure 6.8. (A) Transient absorption spectra of the $BiVO_4$ film recorded 1) 1 ps, 2) 20 ps and 3) 1000 ps after the pump pulse. The spectra could be divided into two regions: 400-460 nm (bleaching due to ground state depopulation); 460-850 nm (absorption assigned to holes). (B) Transient absorption decay of the $BiVO_4$ film. Traces 1) and 2) correspond to the decay of trapped holes, monitored at 470 and 750 nm, respectively, line 3) corresponds to the bleaching recovery recorded at 420 nm.

charge separation in WO_3 films. In a separate experiment we also verified that electron trapping in compact WO_3 films is much slower than in colloidal systems.[47]

Difference absorption spectra recorded following the excitation of the $BiVO_4$ film at different time delays after the pump pulse are presented in Figure 6.8A. These spectra exhibit a bleaching maximum at 450 nm corresponding to the depletion of ground state absorption. Two induced absorption bands are also observed in the 460-550 and 700-800 nm regions. The absorption-time profiles recorded at 420, 470 and 750 nm, corresponding to the three above-mentioned spectral regions, are shown in Figure 6.8B. All these three traces show initial fast recovery followed by a long-lived transient signal.

The transient absorption features of $BiVO_4$ at 470 and 750 nm were also investigated to identify the charge carriers contributing to absorption. An aqueous 0.5 M Na_2SO_3 solution was used as a hole scavenger. The film was immersed in the solution for 24 h, then transient absorption measurements were recorded in contact with the electron donor solution. The ΔA signals recorded at 470 nm and 750 nm with $BiVO_4$ films under vacuum and in contact with an aqueous solution containing 0.5 M Na_2SO_3, as electron donor, are reported in Figure 6.9A and 6.9B.

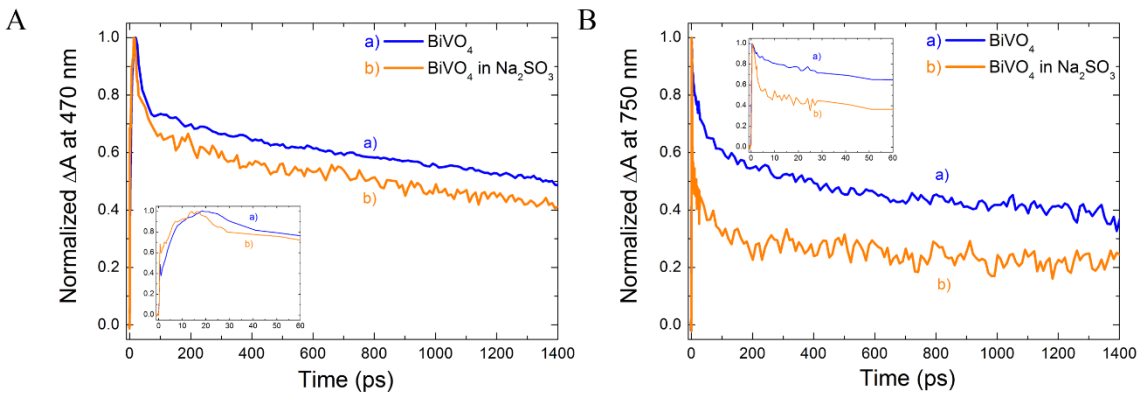

Figure 6.9. Absorption decay profiles recorded at (A) 470 nm and (B) 750 nm for the $BiVO_4$ film, a) under vacuum and b) in the presence of 0.5 M Na_2SO_3 aqueous solution, as electron donor. The insets show the magnification of the signals in the first 60 ps after excitation.

The decay signal recorded under vacuum at 750 nm was fitted by a biexponential decay model (eqn (3)).

$$\Delta A_{decay} = A_1\, e^{(-t/\tau_1)} + A_2\, e^{(-t/\tau_2)} + \Delta A_0 \qquad \text{eqn. (3)}$$

where τ_1 and τ_2 are the time constants of the two decay components, A_1 and A_2 are their weights and ΔA_0 is the offset (set as zero in the fitting).

The decay at 750 nm recorded in the presence of a Na_2SO_3 solution was fitted by a triexponential decay model (eqn (4)).

$$\Delta A_{decay} = A_{\mathrm{hs}}\, e^{(-t/\tau_{hs})} + A_1\, e^{(-t/\tau_1)} + A_2\, e^{(-t/\tau_2)} + \Delta A_0 \qquad \text{eqn. (4)}$$

In the presence of a hole scavenger a new decay pathway is open, due to hole filling by Na_2SO_3, with a decay time τ_{hs} of 1.8 ± 0.1 ps and a A_{hs} weight. The calculated fitting parameters are summarized in Table 6.1. Only the short components of the decay (τ_{hs} and τ_1) are affected by the presence of Na_2SO_3, indicating that such signal decay can be ascribed to holes. Almost the same long time component τ_2 was found both under vacuum and in the presence of the Na_2SO_3 solution. Therefore holes can be filled by the electron donor before being trapped, while trapped holes decay only by slow recombination with trapped electrons.

Table 6.1. Fitting parameters of the DA signals recorded at 750 nm with the $BiVO_4$ film under vacuum and in the presence of Na_2SO_3 as hole scavenger

	$BiVO_4$	$BiVO_4$ in Na_2SO_3
A_{hs}		0.51 ± 0.02
τ_{hs} (ps)		1.85 ± 0.15
A_1	0.38 ± 0.02	0.201 ± 0.013
τ_1 (ps)	38 ± 2	54 ± 9
A_2	0.620 ± 0.006	0.288 ± 0.008
τ_2 (ps)	3373 ± 128	3377 ± 433
χ^{2a}	$4.8\ 10^{-4}$	$8.3\ 10^{-4}$

[a] The χ^2 (chi square) term is used to estimate the reliability of the fitting model and the experimental data, the fit is good if χ^2 is minimized.

The faster decay in the presence of Na_2SO_3 solutions confirms the ability of Na_2SO_3 to scavenge photogenerated holes. Thus, we attribute the transient absorption with maxima at 470 and 750 nm to trapped holes in $BiVO_4$. This assignment is in agreement with earlier work in which the induced absorbance in the transient spectrum was also attributed to trapped holes in $BiVO_4$.[31,48,49] The decrease in magnitude of ΔA with time in the present investigation corresponds to the loss of holes through electron-hole recombination. It is therefore possible to gain information on the electron relaxation dynamics by analyzing the decay kinetics at 470 nm (Figure 6.10).

A model of carrier dynamics that includes relaxation and trapping rates for electrons and holes in $BiVO_4$ was recently proposed by Ravensbergen *et al.*[49] Photogenerated holes, associated with the rise of a pronounced absorption at 475 nm and a broad absorption extending beyond 700 nm, were found to trap with a time constant of 5 ps. After the initial formation of trapped holes, Ravensbergen *et al.* observed a biexponential decay of this induced

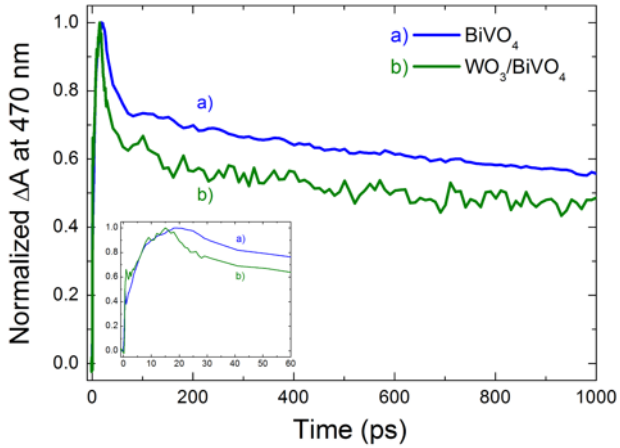

Figure 6.10. Transient absorption decay at 470 nm monitored for a) the $BiVO_4$ and b) the $WO_3/BiVO_4$ heterojunction electrodes. In the case of the coupled system the faster decay is due to holes filling by back transferred electrons from the conduction band of WO_3 to the valence band of $BiVO_4$. Inset: magnification of the ΔA signal at short time after the laser pulse.

absorbance with time constants of 40 ps and 2.5 ns, attributed to the recombination of electrons and holes.

Consistent with these results, we analyzed the transient ΔA signal (monitored at 470 nm) obtained after 387 nm excitation with a monoexponential growth and biexponential kinetic decay by fitting the transient absorption with (eqn. (5)):

$$\Delta A = C\left[-e^{\left(-\frac{t}{\tau_{TR}}\right)} + A_1\, e^{\left(-\frac{t}{\tau_r}\right)} + A_2\, e^{\left(-\frac{t}{\tau_t}\right)}\right] \qquad \text{eqn. (5)}$$

where C is the magnitude of the transient absorption signal due to hole trapping and τ_{TR} is the hole trapping time constant, τ_r and τ_t are the shorter and longer decay components with weights A_1 and A_2, respectively. The growth of ΔA with a time constant τ_{TR} of 6.9 ± 0.6 ps and two decay components, of 24 ± 4 ps and 3.7 ± 0.2 ns were obtained (Table 6.2). The two decay lifetimes labeled τ_r and τ_t in eqn. 5 are ascribed to the depletion of trapped holes due to electron-hole recombination competing with hot electron cooling and electron trapping, respectively.[49] As shown in Table 6.2, the initial decay process was responsible for *ca.* 50% of the decay. The relatively long-lived tail absorption corresponds to recombination between the trapped charge carriers.[49]

Table 6.2. Fitting parameters eqn. (5)) for the ΔA signals at 470 nm recorded with the $BiVO_4$ and $WO_3/BiVO_4$ films

	$BiVO_4$	**$WO_3/BiVO_4$**
τ_{TR} (ps)	6.9 ± 0.6	6.2 ± 1.3
A_1	0.51 ± 0.04	0.63 ± 0.07
τ_r (ps)	24 ± 4	18 ± 5
A_2	0.49 ± 0.06	0.37 ± 0.13
τ_t (ps)	3708 ± 163	3907 ± 379
χ^{2a}	$7.0\ 10^{-4}$	$2.2\ 10^{-3}$

[a] The χ^2 (chi square) term is used to estimate the reliability of the fitting model and the experimental data, the fit is good if χ^2 is minimized.

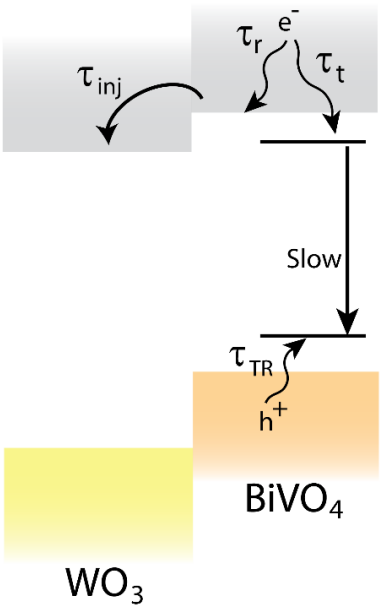

Scheme 6.1. Proposed charge carrier transitions involving $BiVO_4$ and WO_3. For the different time constants labelling, please refer to the text.

The 470 nm transient absorption decay of the $WO_3/BiVO_4$ composite system (Figure 6.10) was also fitted according to eqn. (5) and the fitting parameters are also reported in Table 6.2. By comparing these parameters with the corresponding ones obtained in the case of the single $BiVO_4$ film, first of all we notice that hole trapping occurs on a similar timescale (τ_{TR} = 6-7 ps). The shorter lifetime component τ_r exhibits a value of 18 ps for $WO_3/BiVO_4$ system, which is shorter than that of pristine $BiVO_4$ (τ_r = 24 ps). Thus, as shown in Scheme 6.1, a new electron-hole recombination path is at work when $BiVO_4$ is in contact with WO_3, occurring on the same time scale and in competition with hot electrons cooling, *i.e.* their injection from $BiVO_4$ into WO_3, followed by back electron transfer from WO_3 to the $BiVO_4$ valence band. We are unable to determine which of these two steps is the rate limiting process dictating the disappearance of trapped holes in the $WO_3/BiVO_4$ coupled system. The longer hole decay component (with time constant τ_t ~ 3.8 ns) does not appear to be markedly influenced by the presence of WO_3.

3.5. Tracking electron injection with TH photocatalytic reduction as probe reaction

Thionine (TH) has been widely used to probe the photocatalytic reduction properties of semiconductor particles and mesoscopic films. Here we employed photocatalytic TH reduction in order to obtain information about the potential energy of photoexcited electrons in the three studied electrodes and in particular in the combined system. By measuring the ratio of unreduced/reduced thionine it is possible to determine the Fermi

level of semiconductor materials.[46,50] The two-electron reduction of thionine to the colorless TH^{2-} leuco form can be monitored following the bleaching of the TH absorption maximum at 606 nm (reactions 3 and 4).

$$MO_{(e^-)} + TH(blue) \rightarrow MO + TH^{-\bullet} \quad (3)$$

$$2\ TH^{-\bullet} \rightarrow TH^{2-}(colorless) + TH \quad (4)$$

with $MO_{(e^-)}$ representing an electron photopromoted in the conduction band of a metal oxide MO and $TH^{-\bullet}$ is the semireduced dye form. Metastable $TH^{-\bullet}$ undergoes quick disproportionation yielding the reduced colorless TH^{2-} form.

The reduced form is stable under inert atmosphere, while it oxidizes quickly when exposed to air. In the present study TH bleaching has been investigated in the presence of the WO_3, $BiVO_4$ and $WO_3/BiVO_4$ photoelectrodes under visible light irradiation (λ > 400 nm) without any applied bias. A blank experiment was also run using FTO in place of the semiconductor films.

With increasing the duration of visible light irradiation, a decrease in the absorption at 606 nm was observed (Figure 6.11A), as TH captures electrons from the semiconductor film and undergoes reduction. The reduction step was confirmed by

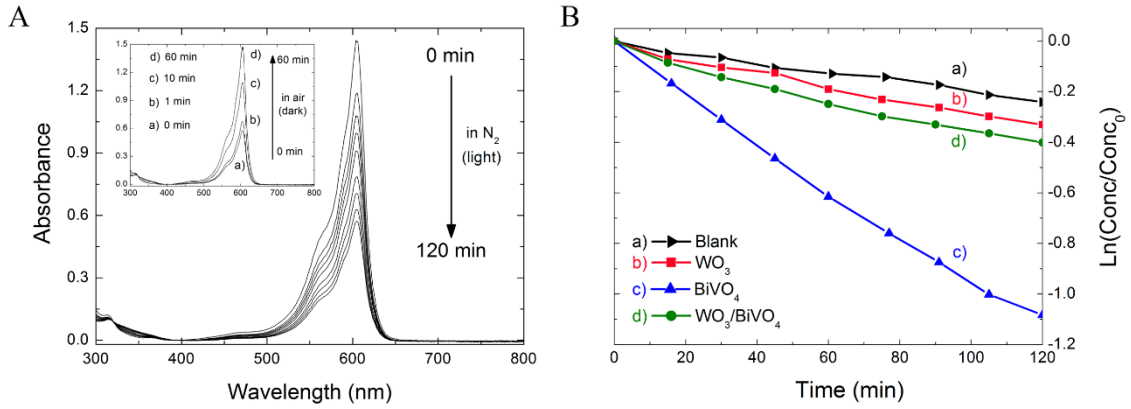

Figure 6.11. (A) Absorption spectra recorded during a TH photoreduction experiment in the presence of $BiVO_4$. Inset: absorption spectra recorded at different time after opening the cuvette to air after the end of irradiation: the solution recovered the blue coloration of oxidized TH. (B) Logarithmic plot of the concentration decay of TH in contact with WO_3, $BiVO_4$ and $WO_3/BiVO_4$ films irradiated at 400 nm. The blank experiment a) was run with FTO placed in the cuvette, in contact with the TH solution.

exposure of the solution to air at the end of irradiation experiment. The solution containing reduced TH completely recovered its original color after exposure to air (inset of Figure 6.11A), confirming that the disappearance of the dye in Figure 6.8A was due to the reduction process (reactions 3 and 4).

TH reduction in the presence of WO_3, $BiVO_4$ and of the combined $WO_3/BiVO_4$ films coated on FTO is shown in Figure 6.11B. Photoirradiated $BiVO_4$ film exhibited a faster reduction rate (k_{et} = 9. 2 $\times 10^{-3}$ min^{-1}) than the WO_3 film (k_{et} = 2.7 $\times 10^{-3}$ min^{-1}). Interestingly with the coupled $WO_3/BiVO_4$ system the reduction rate (k_{et} = 3.3 $\times 10^{-3}$ min^{-1}) was more similar to that obtained with WO_3 than to that obtained with $BiVO_4$.

In order to explain the results of TH reduction, the flat band potentials of the three materials were determined by photoelectrochemical measurements in the presence of Na_2SO_3 0.5 M as hole scavenger. We confirmed the band gap position of the studied materials, by performing PEC experiments with the films in contact with a Na_2SO_3 solution. This electron donor quickly fills surface holes, thus minimizing electron-hole recombination. By this way the photocurrent onset was shifted to negative potentials providing a good approximation of the flat band potential. PEC measurements are reported in Figure 6.12, with the insets showing magnified views of the photocurrent profiles near the onset potential.

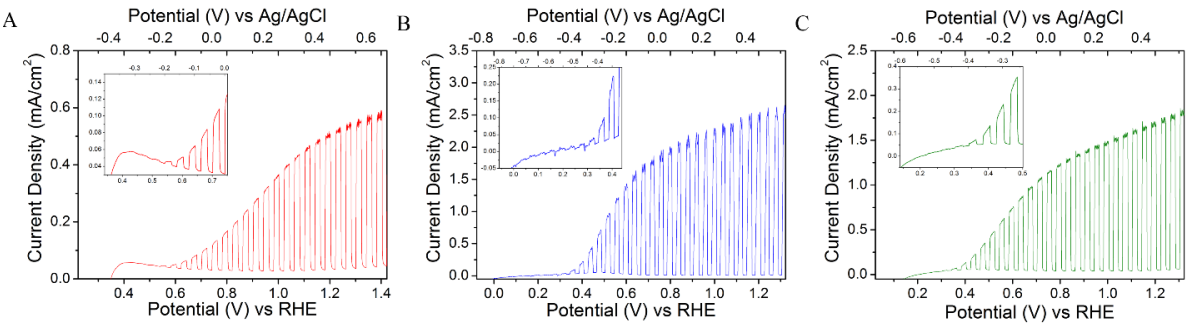

Figure 6.12. Current density *vs* applied potential experiments in the presence of Na_2SO_3 (electron donor) measured with A) the WO_3, B) the $BiVO_4$ and C) the $WO_3/BiVO_4$ electrode. The insets show magnifications close to the onset potential.

The conduction band edge positions of WO_3 and $BiVO_4$ are +0.41 V and +0.02 V, respectively (Scheme 6.2), in agreement with those reported in the literature.[24] When compared to the flat band potential of $BiVO_4$, that of the composite material results shifted by 170 mV to positive potentials. The positive shift is consistent with a shift of the Fermi level due to electron equilibration at the interface between the two materials. The conduction bands of all investigated materials are more negative in energy than the TH reduction potential (+0.48 eV).[58]

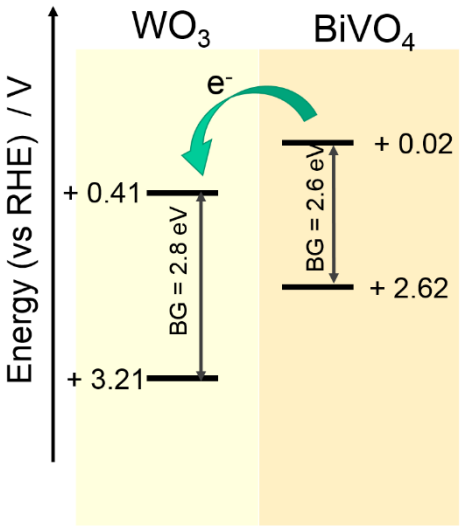

Scheme 6.2. Diagram of the band edge positions of the single materials.

Under such conditions, surface charge recombination is completely suppressed and the onset potential is cathodically shifted. The estimated onset potential is a good approximation of the flat band potential of the electrodes.[51] As expected, the flat band potentials of the single WO_3 and $BiVO_4$ films and of the coupled $WO_3/BiVO_4$ electrode were found to be more negative in energy than the reduction potential of TH (0.064 V *vs.* NHE at pH 7).[52] Measurements on $BiVO_4$ and $WO_3/BiVO_4$ electrodes gave flat band values of 0.02 V and 0.19 V *vs.* RHE, respectively, indicating that the flat band potential (or apparent Fermi level[50]) in the coupled system is positively shifted by *ca.* 170 mV with respect to that of $BiVO_4$ and closer to that of WO_3 films (Scheme 6.3). As previously shown, the driving force for the reduction step, measured from the difference between the conduction band of the semiconductor and the reduction potential of the electron acceptor, dictates the rate of electron transfer. The

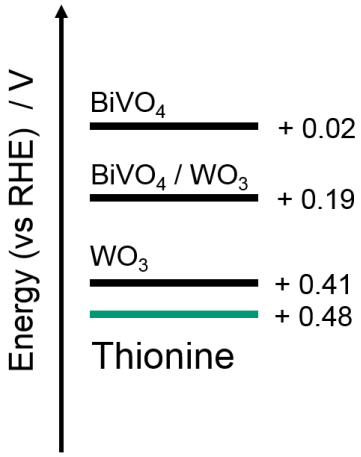

Scheme 6.3. Apparent energy of semiconductors Fermi levels (see SI for details)

decreased driving force for reduction of $WO_3/BiVO_4$ with respect to $BiVO_4$ makes the reduction rate lower in the coupled system and it is an evidence that photopromoted electrons in $BiVO_4$ undergo a decrease in their reduction potential after their injection in the conduction band of WO_3.

The electron transfer from photoexcited $BiVO_4$ to the conduction band of WO_3 leads to the two different effects observed in PEC experiments in the presence of Na_2SO_4 electrolyte solution and TH reduction measurements, respectively. On one side, during photoelectrochemical experiments in the presence of an inert electrolyte, such as Na_2SO_4, fast electron injection from $BiVO_4$ to WO_3 enhances charge separation and leads to a retardation in the recombination rate of photogenerated charge carriers. Despite the free energy loss, longer-living electron-hole couples enhance the photoelectrochemical performance of such system with respect to single $BiVO_4$. On the other hand in reactions where surface recombination is completely suppressed by the effect of electron donors (namely ethanol in TH reduction without applied bias or Na_2SO_3 in the PEC measurements), the effectiveness in the reduction reaction is dictated by the apparent Fermi level of the material.

4. CONCLUSIONS

$BiVO_4$, a photocatalyst with response in the visible region, can participate to reduction and oxidation process quite effectively. The charge separation in this system can be improved by coupling it with another oxide film (*e.g.* WO_3, E_{CB} = +0.41 V *vs*. RHE) capable of accepting electrons from the conduction band of $BiVO_4$ (E_{CB} = +0.02 V *vs*. RHE). While electrons lose their driving force for reduction, hole oxidation is significantly enhanced as evidenced by the enhanced photoconversion efficiency. The trapped holes, as characterized from transient absorption measurements, provide further insight into the excited state dynamics. A better understanding of the fast

charge separation dynamics occurring in coupled oxides can further aid in designing tandem photocatalytic systems in which reduction and oxidation occur on two different particles.

REFERENCES

(1) Kudo, A.; Miseki, Y. Heterogeneous Photocatalyst Materials for Water Splitting. *Chem. Soc. Rev.* **2009**, *38*, 253–278.

(2) Maeda, K.; Domen, K. Photocatalytic Water Splitting: Recent Progress and Future Challenges. *J. Phys. Chem. Lett.* **2010**, *1*, 2655–2661.

(3) Dozzi, M. V.; Selli, E. Doping TiO_2 with P-Block Elements: Effects on Photocatalytic Activity. *J. Photochem. Photobiol. C Photochem. Rev.* **2013**, *14*, 13–28.

(4) Zou, Z.; Ye, J.; Sayama, K.; Arakawa, H. Direct Splitting of Water under Visible Light Irradiation with an Oxide Semiconductor Photocatalyst. *Nature* **2001**, *414*, 625–627.

(5) Maeda, K.; Takata, T.; Hara, M.; Saito, N.; Inoue, Y.; Kobayashi, H.; Domen, K. GaN:ZnO Solid Solution as a Photocatalyst for Visible-Light-Driven Overall Water Splitting. *J. Am. Chem. Soc.* **2005**, *127*, 8286–8287.

(6) Park, Y.; McDonald, K. J.; Choi, K.-S. Progress in Bismuth Vanadate Photoanodes for Use in Solar Water Oxidation. *Chem. Soc. Rev.* **2013**, *42*, 2321–2337.

(7) Bignozzi, C. A.; Caramori, S.; Cristino, V.; Argazzi, R.; Meda, L.; Tacca, A. Nanostructured Photoelectrodes Based on WO_3: Applications to Photooxidation of Aqueous Electrolytes. *Chem. Soc. Rev.* **2013**, *42*, 2228–2246.

(8) Gratzel, M. Photoelectrochemical Cells. *Nature* **2001**, *414*, 338–344.

(9) Santato, C.; Odziemkowski, M.; Ulmann, M.; Augustynski, J. Crystallographically Oriented Mesoporous WO_3 Films: Synthesis, Characterization, and Applications. *J. Am. Chem. Soc.* **2001**, *123*, 10639–10649.

(10) Kudo, A.; Omori, K.; Kato, H. A Novel Aqueous Process for Preparation of Crystal Form-Controlled and Highly Crystalline $BiVO_4$ Powder from Layered Vanadates at Room Temperature and Its Photocatalytic and Photophysical Properties. *J. Am. Chem. Soc.* **1999**, *121*, 11459–11467.

(11) Walsh, A.; Yan, Y.; Huda, M. N.; Al-Jassim, M. M.; Wei, S. Band Edge Electronic Structure of $BiVO_4$: Elucidating the Role of the Bi s and V d Orbitals. *Chem.*

Mater. **2009**, *21*, 547–551.

(12) Eisenberg, D.; Ahn, H. S.; Bard, A. J. Enhanced Photoelectrochemical Water Oxidation on Bismuth Vanadate by Electrodeposition of Amorphous Titanium Dioxide. *J. Am. Chem. Soc.* **2014**, *136*, 14011–14014.

(13) Mcdowell, M. T.; Lichterman, M. F.; Spurgeon, J. M.; Hu, S.; Sharp, I. D.; Brunschwig, B. S.; Lewis, N. S. Improved Stability of Polycrystalline Bismuth Vanadate Photoanodes by Use of Dual-Layer Thin TiO_2/Ni Coatings. *J. Phys. Chem. C* **2014**, *118*, 19618–19624.

(14) Park, H. S.; Kweon, K. E.; Ye, H.; Paek, E.; Hwang, G. S.; Bard, A. J. Factors in the Metal Doping of BiVO 4 for Improved Photoelectrocatalytic Activity as Studied by Scanning Electrochemical Microscopy and First-Principles Density-Functional Calculation. *J. Phys. Chem. C* **2011**, *115*, 17870–17879.

(15) Abdi, F. F.; Han, L.; Smets, A. H. M.; Zeman, M.; Dam, B.; Van de Krol, R. Efficient Solar Water Splitting by Enhanced Charge Separation in a Bismuth Vanadate-Silicon Tandem Photoelectrode. *Nat. Commun.* **2013**, *4*, 2195.

(16) Huang, Z.-F.; Pan, L.; Zou, J.-J.; Zhang, X.; Wang, L. Nanostructured Bismuth Vanadate-Based Materials for Solar-Energy-Driven Water Oxidation: A Review on Recent Progress. *Nanoscale* **2014**, *6*, 14044–14063.

(17) Zhang, L.; Reisner, E.; Baumberg, J. J. Al-Doped ZnO Inverse Opal Networks as Efficient Electron Collectors in $BiVO_4$ Photoanodes for Solar Water Oxidation. *Energy Environ. Sci.* **2014**, *7*, 1402–1408.

(18) Zhou, M.; Bao, J.; Xu, Y.; Zhang, J.; Xie, J.; Guan, M.; Wang, C.; Wen, L.; Lei, Y.; Xie, Y. Photoelectrodes Based upon Mo:$BiVO_4$ Inverse Opals for Photoelectrochemical Water Splitting. *ACS Nano* **2014**, *8*, 7088–7098.

(19) Kim, T. W.; Choi, K.-S. Nanoporous $BiVO_4$ Photoanodes with Dual-Layer Oxygen Evolution Catalysts for Solar Water Splitting. *Science* **2014**, *343*, 990–994.

(20) Pilli, S. K.; Furtak, T. E.; Brown, L. D.; Deutsch, T. G.; Turner, J. a.; Herring, A. M. Cobalt-Phosphate (Co-Pi) Catalyst Modified Mo-Doped BiVO4 Photoelectrodes for Solar Water Oxidation. *Energy Environ. Sci.* **2011**, *4*, 5028–5034.

(21) Zhong, D. K.; Choi, S.; Gamelin, D. R. Near-Complete Suppression of Surface Recombination in Solar Photoelectrolysis by “Co-Pi” Catalyst-Modified W:$BiVO_4$. *J. Am. Chem. Soc.* **2011**, *133*, 18370–18377.

(22) Chatchai, P.; Murakami, Y.; Kishioka, S.; Nosaka, A. Y.; Nosaka, Y. Efficient Photocatalytic Activity of Water Oxidation over $WO_3/BiVO_4$ Composite under Visible Light Irradiation. *Electrochim. Acta* **2009**, *54*, 1147–1152.

(23) Su, J.; Guo, L.; Bao, N.; Grimes, C. A. Nanostructured $WO_3/BiVO_4$ Heterojunction Films for Efficient Photoelectrochemical Water Splitting. *Nano Lett.* **2011**, *11*, 1928–1933.

(24) Hong, S. J.; Lee, S.; Jang, J. S.; Lee, J. S. Heterojunction $BiVO_4/WO_3$ Electrodes for Enhanced Photoactivity of Water Oxidation. *Energy Environ. Sci.* **2011**, *4*, 1781–1787.

(25) Fujimoto, I.; Wang, N.; Saito, R.; Miseki, Y.; Gunji, T.; Sayama, K. $WO_3/BiVO_4$ Composite Photoelectrode Prepared by Improved Auto-Combustion Method for Highly Efficient Water Splitting. *Int. J. Hydrogen Energy* **2014**, *39*, 2454–2461.

(26) Durrant, J. R. Molecular Approaches to Solar Energy Conversion: The Energetic Cost of Charge Separation from Molecular-Excited States. *Philos. Trans. R. Soc. A* **2013**, *371*, 20120195.

(27) Pihosh, Y.; Turkevych, I.; Mawatari, K.; Asai, T.; Hisatomi, T.; Uemura, J.; Tosa, M.; Shimamura, K.; Kubota, J.; Domen, K.; et al. Nanostructured $WO_3/BiVO_4$ Photoanodes for Efficient Photoelectrochemical Water Splitting. *Small* **2014**, *10* , 3692–3699.

(28) Tang, J.; Durrant, J. R.; Klug, D. R. Mechanism of Photocatalytic Water Splitting in TiO_2. Reaction of Water with Photoholes, Importance of Charge Carrier Dynamics, and Evidence for Four-Hole Chemistry. *J. Am. Chem. Soc.* **2008**, *130*, 13885–13891.

(29) Pendlebury, S. R.; Barroso, M.; Cowan, A. J.; Sivula, K.; Durrant, J. R.; Tang, J.; Gratzel, M. Dynamics of Photogenerated Holes in Nanocrystalline α-Fe_2O_3 Electrodes for Water Oxidation Probed by Transient Absorption Spectroscopyw. *Chem. Commun.* **2011**, *47*, 716–718.

(30) Pesci, F. M.; Cowan, A. J.; Alexander, B. D.; Durrant, J. R.; Klug, D. R. Charge Carrier Dynamics on Mesoporous WO_3 during Water Splitting. *J. Phys. Chem. Lett.* **2011**, *2*, 1900–1903.

(31) Ma, Y.; Pendlebury, S. R.; Reynal, A.; Le Formal, F.; Durrant, J. R. Dynamics of Photogenerated Holes in Undoped $BiVO_4$ Photoanodes for Solar Water Oxidation. *Chem. Sci.* **2014**, *5*, 2964–2973.

(32) Cherepy, N. J.; Liston, D. B.; Lovejoy, J. A.; Deng, H.; Zhang, J. Z. Ultrafast Studies of Photoexcited Electron Dynamics in γ- and α-Fe_2O_3 Semiconductor Nanoparticles. *J. Phys. B* **1998**, *102*, 770–776.

(33) Pendlebury, S. R.; Wang, X.; Formal, F. Le; Cornuz, M.; Kafizas, A.; Tilley, S. D.; Gratzel, M.; Durrant, J. R. Ultrafast Charge Carrier Recombination and Trapping in Hematite Photoanodes under Applied Bias. *J. Am. Chem. Soc.* **2014**, *136*, 9854–9857.

(34) Kronawitter, C. X.; Vayssieres, L.; Shen, S.; Guo, L.; Wheeler, D. A.; Zhang, J. Z.; Antoun, B. R.; Mao, S. S. A Perspective on Solar-Driven Water Splitting with All-Oxide Hetero-Nanostructures. *Energy Environ. Sci.* **2011**, *4*, 3889–3899.

(35) Su, J.; Guo, L.; Yoriya, S.; Grimes, C. A. Aqueous Growth of Pyramidal-Shaped $BiVO_4$ Nanowire Arrays and Structural Characterization: Application to Photoelectrochemical Water Splitting. *Cryst. Growth Des.* **2010**, *10*, 856–861.

(36) Luo, W.; Yang, Z.; Li, Z.; Zhang, J.; Liu, J.; Zhao, Z.; Wang, Z.; Yan, S.; Yu, T.; Zou, Z. Solar Hydrogen Generation from Seawater with a Modified $BiVO_4$ Photoanode. *Energy Environ. Sci.* **2011**, *4*, 4046–4051.

(37) Pokhrel, S.; Birkenstock, J.; Schowalter, M.; Rosenauer, A.; Mädler, L. Growth of Ultrafine Single Crystalline WO_3 Nanoparticles Using Flame Spray Pyrolysis. *Cryst. Growth Des.* **2010**, *10*, 632–639.

(38) Pokhrel, S.; Simion, C. E.; Teodorescu, V. S.; Barsan, N.; Weimar, U. Synthesis, Mechanism, and Gas-Sensing Application of Surfactant Tailored Tungsten Oxide Nanostructures. *Adv. Funct. Mater.* **2009**, *19*, 1767–1774.

(39) Abdi, F. F.; Savenije, T. J.; May, M. M.; Dam, B.; Van De Krol, R. The Origin of Slow Carrier Transport in $BiVO_4$ Thin Film Photoanodes: A Time-Resolved Microwave Conductivity Study. *J. Phys. Chem. Lett.* **2013**, *4*, 2752–2757.

(40) Abdi, F. F.; Van De Krol, R. Nature and Light Dependence of Bulk Recombination in Co-Pi-Catalyzed $BiVO_4$ Photoanodes. *J. Phys. Chem. C* **2012**, *116*, 9398–9404.

(41) Butler, M. A. Photoelectrolysis and Physical Properties of the Semiconducting Electrode WO_2. *J. Appl. Phys.* **1977**, *48*, 1914–1920.

(42) Christians, J. A.; Manser, J. S.; Kamat, P. V. Best Practices in Perovskite Solar Cell Efficiency Measurements. Avoiding the Error of *Making Bad Cells Look Good*. *J. Phys. Chem. Lett.* **2015**, *6*, 852–857.

(43) Kay, A.; Cesar, I.; Grätzel, M. New Benchmark for Water Photooxidation by Nanostructured α-Fe_2O_3 Films. *J. Am. Chem. Soc.* **2006**, *128*, 15714–15721.

(44) http://rredc.nrel.gov/solar/spectra/am1.5.

(45) Hotchandani, S.; Bedja, I.; Fessenden, R. W.; Kamat, P. V. Electrochromic and Photoelectrochromic Behavior of Thin WO_3 Films Prepared from Quantum Size Colloidal Particles. *Langmuir* **1994**, *10*, 17–22.

(46) Regragui, M.; Addou, M.; Outzourhit, A.; El, E. Electrochromic Effect in WO_3 Thin Films Prepared by Spray Pyrolysis. *Sol. Energy Mater. Sol. Cells* **2003**, *77*, 341–350.

(47) Yamase, T. Photo- and Electrochromism of Polyoxometalates and Related Materials. *Chem. Rev.* **1998**, *2665*, 307–325.

(48) Huang, Z.-F.; Song, J.; Pan, L.; Zhang, X.; Wang, L.; Zou, J.-J. Tungsten Oxides for Photocatalysis, Electrochemistry, and Phototherapy. *Adv. Mater.* **2015**, *27*, 5309–5327.

(49) Pesci, F. M.; Cowan, A. J.; Alexander, B. D.; Durrant, J. R.; Klug, D. R. Charge Carrier Dynamics on Mesoporous WO_3 during Water Splitting. **2011**, 1900–1903.

(50) Subramanian, V.; Wolf, E. E.; Kamat, P. V. Catalysis with TiO_2/gold Nanocomposites. Effect of Metal Particle Size on the Fermi Level Equilibration. *J. Am. Chem. Soc.* **2004**, *126*, 4943–4950.

(51) Christians, J. A.; Leighton, D. T.; Kamat, P. V. Rate Limiting Interfacial Hole Transfer in Sb_2S_3 Solid-State Solar Cells. *Energy Environ. Sci.* **2014**, *7*, 1148–1158.

(52) Jara, D. H.; Yoon, S. J.; Stamplecoskie, K. G.; Kamat, P. V. Size-Dependent Photovoltaic Performance of $CuInS_2$ Quantum Dot-Sensitized Solar Cells. *Chem. Mater.* **2014**, *26*, 7221–7228.

(53) Stamplecoskie, K. G.; Chen, Y.-S.; Kamat, P. V. Excited-State Behavior of Luminescent Glutathione-Protected Gold Clusters. *J. Phys. Chem. C* **2014**, *118*, 1370–1376.

(54) Bedja, I.; Hotchandani, S.; Kamat, P. V. Photoelectrochemistry of Quantized WO_3 Colloids. Electron Storage, Electrochromic, and Photoelectrochromic Effects. *J. Phys. Chem.* **1993**, *97*, 11064–11070.

(55) Nenadovie, M. T.; Rajh, T. Electron Transfer Reactions and Flat-Band Potentials of WO_3 Colloids. *J. Phys. Chem.* **1984**, *88*, 5827–5830.

(56) Aiga, N.; Jia, Q.; Watanabe, K.; Kudo, A.; Sugimoto, T.; Matsumoto, Y. Electron–Phonon Coupling Dynamics at Oxygen Evolution Sites of Visible-Light-Driven Photocatalyst: Bismuth Vanadate. *J. Phys. Chem. C* **2013**, *117*, 9881–9886.

(57) Ravensbergen, J.; Abdi, F. F.; Van Santen, J. H.; Frese, R. N.; Dam, B.; Van De Krol, R.; Kennis, J. T. M. Unraveling the Carrier Dynamics of $BiVO_4$: A Femtosecond to Microsecond Transient Absorption Study. *J. Phys. Chem. C* **2014**, *118*, 27793–27800.

(58) Kamat, P. V. Photoelectrochemistry in Colloidal Systems. *J. Chem. Soc. Faraday Trans. 1* **1985**, *81*, 509–518.

(59) Chen, Z.; Jaramillo, T. F.; Deutsch, T. G.; Kleiman-Shwarsctein, A.; Forman, A. J.; Gaillard, N.; Garland, R.; Takanabe, K.; Heske, C.; Sunkara, M.; et al. Accelerating Materials Development for Photoelectrochemical Hydrogen Production: Standards for Methods, Definitions, and Reporting Protocols. *J. Mater. Res.* **2011**, *25*, 3–16.

Chapter 7

The wavelength dependent charge carrier exchange between WO_3 and $BiVO_4$ in coupled WO_3/$BiVO_4$ systems

ABSTRACT

In this Chapter recent results are described on the further investigations on the dynamics of charge carriers in the WO_3/$BiVO_4$ heterojunction system. The fs-TAS characterization of two series of photoanodes with different $BiVO_4$ thickness allowed us to improve the scheme of photogenerated charge interaction between the two oxides reported in the previous Chapter. The model was found to accurately explain the performance of the two series of photoanodes in several PEC experiments.

1. INTRODUCTION

$BiVO_4$ has emerged rapidly as one of the most promising photoanode materials for the oxygen evolution reaction (OER). Films prepared with state of the art synthetic procedures perform remarkably well with highly stable photocurrent densities. The deposition of OER catalysts allow to decrease the overpotential needed to overcome the slow kinetics of O_2 evolution and therefore the photocurrent onset results cathodically shifted. In the WO_3/$BiVO_4$ heterojunction the excellent visible light harvesting properties of $BiVO_4$ are combined with the superior conductivity of the photogenerated charge carriers typical of WO_3. Due to the favorable band alignment between the two oxides, photopromoted electrons in $BiVO_4$ flow into the WO_3 conduction band (CB) and rapidly diffuse at the external circuit, exploiting the better charge mobility of the latter material. Thus, in this semiconductor oxide sensitized photoanode, better spatial charge separation is achieved limiting e^-/h^+ pairs recombination in photoexcited $BiVO_4$.

While band alignment and the enhanced performance of the heterojunction photoanode clearly suggest this charge transfer interaction, a direct and complete evidence of the fast dynamics occurring after photon absorption is still missing. Recently

the first femtosecond transient absorption spectroscopy (fs-TAS) studies on the charge carriers dynamics in $BiVO_4$ appeared[1] and Van de Krol's group finally unraveled the complex process occurring after band gap excitation, on a time scale ranging from ps to μs.

In the previous chapter we discussed the fs-TAS experiments on $BiVO_4$ and WO_3/$BiVO_4$ photoanodes and we used the obtained results to have an insight on the interfacial interactions between the two oxides. In the present Chapter we explain our efforts aimed at completely unveil the charge transfer processes in such system.

We prepared two series of photoanodes, one containing a $BiVO_4$ layer deposited directly on FTO conductive glass (BV series) and the second including a WO_3 layer between the FTO and $BiVO_4$ (WBV series). In the two series we varied the $BiVO_4$ thickness only, performing subsequent layer deposition through spin coating a precursor solution. In order to definitively assign to surface trapped holes the typical transient positive absorption signal of $BiVO_4$, we evaluated the spectral changes of this material in electrochromic experiments. Then, using fs-TAS, we evaluated the thickness dependence of the photoinduced species after 387 nm pump excitation. The use of less energetic pumps (centered at 450, 460, and 500 nm) allowed us to confirm that the recombination between hot electrons and trapped holes accounts for the fast recombination process. More interestingly, by comparing the decay kinetics of BV and WBV films with identical $BiVO_4$ thickness, we found that the effect of the WO_3 underlayer strongly depends on the energy of the absorbed photons. For high energy photons (*i.e.* 387 nm pump), holes are shorter lived in the coupled system, while for photons with energy close to the energy gap of $BiVO_4$ (*i.e.* 500 nm pump), the hole lifetime is largely

extended. On the other hand, after excitation with a 450 nm pump, the signal decay profiles obtained with the BV and WBV films are very similar, while in the case of intermediate wavelengths, *e.g.* with the 460 nm pump, the hole lifetime increases but less markedly than for the 500 nm pump.

The extended lifetime found in the coupled system for pump wavelengths lower in energy than the WO_3 band gap (450 nm) directly proves, for the first time, that the injection of photoexcited electrons from the $BiVO_4$ conduction band (CB) to WO_3 CB (k_{inj}) leads to the effective space separation of the e^-/h^+ pairs. However, photons with energy greater than the WO_3 band gap excite both semiconductors and the recombination between electrons photoexcited in the CB of WO_3 and photogenerated holes in the valence band (VB) of $BiVO_4$ (k_{W-inj}) becomes a viable detrimental process, leading to the decrease of the trapped holes lifetime in the coupled system. Subsequently besides the electron injection from the $BiVO_4$ CB to the WO_3 CB, a second negative pathway is also possible (k_{bck}), the backward electron transfer to the VB of $BiVO_4$.To better elucidate the effect of k_{W-inj}, we carried out more fs-TAS experiments with 387 nm pump excitation on the WBV series and we extracted useful information on this unfavorable process. The results of the wavelength-dependent interaction between WO_3 and $BiVO_4$ in the heterojunction system allowed us to suggest a more accurate model for the optical transitions between the two oxides.

We then validated the transient spectroscopy data and the proposed model by carrying out photoelectrochemical experiments with the two BV and WBV series. In both series we found a correlation between the increased trapped holes lifetime (increasing with the $BiVO_4$ thickness) and the improved PEC performance of thicker films. However, we found

that the photocurrent density drops for films with thickness exceeding 115 nm. Finally, for the films having the optimal $BiVO_4$ thickness, we compared the IPCE at 1.23 V vs RHE measured with the combined electrode with the IPCE values obtained with the single material photoanodes (WO_3 and $BiVO_4$). Form the comparison we found that the photoresponse of the heterojunction photoanode correlates extremely well with the proposed model, with the coupled system working dramatically better than the two separate materials for wavelengths longer than 450 nm. For shorter wavelengths, the efficiency improvement in the heterojunction photoanode is less pronounced. Moreover for wavelengths shorter than 370 nm, the contribution of k_{w-inj} predominates over that of k_{inj} and the coupled system is less active than the sum of the IPCE values of the two separate oxides, even with an applied bias of 1.23 V vs RHE. Therefore the overall photoelectrocatalytic performance of the WO_3/$BiVO_4$ heterojunction is subject to the wavelength-dependent balance between k_{inj} and k_{w-inj}.

2. EXPERIMENTAL

2.1 Materials

The following chemicals were employed: tungsten(VI) ethoxide 99.8% (5% w/v in ethanol), ammonium vanadium oxide, bismuth(III) nitrate pentahydrate ACS 98%, benzyl alcohol ACS 99% (Alpha Aesar); ethyl cellulose (MP Biomedics); citric acid 99% and zirconium oxynitrate hydrate 99% (Aldrich); anhydrous sodium sulfate (Fisher Scientific) tetrabutylammonium tetrafluorophosphate [TBA] [PF_4] (99.0% Aldrich), anhydrous acetonitrile, (99.8% Aldrich).

2.2 Photoelectrodes preparation

WO_3 was prepared as follows. 1.0 mL of tungsten ethoxide, 5 wt% in ethanol, was added to 42 mg of citric acid acting as stabilizer. Once citric acid was completely dissolved, benzyl alcohol (0.3 mL) and ethyl cellulose (40 mg) were added to the solution and stirred overnight to allow the complete dissolution of ethyl cellulose. The so obtained paste is stable for several weeks. Fluorine-doped tin oxide (FTO) glass (Pilkington Glass, TEC-7, thickness 2 mm) was coated with the paste by spin coating at 4000 rpm for 30 s. The final spinning rate was reached with a three acceleration steps program: 200 $rpm*s^{-1}$ up to 1000 rpm, than 500 $rpm*s^{-1}$ up to 2000 rpm and finally 2000 $rpm*s^{-1}$ up to 4000 rpm. Prior to deposition, the FTO glass was cleaned by 30 min-long sonication in an aqueous soap solution, then in ethanol and finally in water. After coating, the film was dried for 1 h at 80°C and then annealed at 500°C for 8 h.

Bismuth vanadate films (BV) were prepared starting from a liquid solution similar to that reported elsewhere.[2] In a typical synthesis, 0.002 mol of $Bi(NO_3)_3$ and NH_4VO_3 were added to 6 mL of HNO_3 23.3% containing 0.004 mol of citric acid. The mixture was stirred overnight to allow dissolution of the precursor. The $BiVO_4$ based photoanodes were prepared on clean FTO by spinning the solution at 8000 rpm for 30 s with an acceleration rate of 6000 $rpm*s^{-1}$. The film was then dried for 1 h at 80°C and annealed for 1 h at 500°C. The thickness of the $BiVO_4$ layer was controlled by repeating the spin coating procedure and the thermal treatment up to eight times. Once the desired optical density was obtained, the electrode was annealed 8 h at 500°C.

The $WO_3/BiVO_4$ combined films (WBV) with different thickness were prepared by coating the WO_3 electrodes (prepared as described before) with the $BiVO_4$ precursor solution. Then the composite film was dried for 1 h at 80°C and annealed for 1 h at 500°C.

The amount of $BiVO_4$ in the $WO_3/BiVO_4$ electrodes was controlled in the same way as for the BV series. The final films were annealed 8 h at 500°C.

Using the here adopted subsequent layer deposition technique we were able to tune the film thickness. With such technique, we obtained a fine tuning of the $BiVO_4$ thickness also between films of the two series prepared with the same number of coating (*i.e.* the same optical densities was obtained). Therefore, here after we indicate the studied $BIVO_4$ photoanodes as BV15 nm, BV30, BV50, BV75, BV115 and BV160, with the heterojunction $WO_3/BiVO_4$ photoanodes as WBV15, WB30, WB50, WB75, WB115, WB160 where the number indicating the thickness of the $BiVO_4$ layer in nanometers. We slightly approximated the thickness value to simplify the comparison between films of the two sets. Please refer to Table 1 for the exact values.

2.3 Optical and morphological measurements

Images showing the morphology and the cross sectional view of the electrodes were obtained using a FEI Magellan-400 field emission scanning electron microscope (FESEM). UV-visible absorption spectra were recorded using a Jasco V650 spectrophotometer. The crystalline phase of the materials was determined through XRPD analysis using a PHILIPS PW1820 with Cu Kα radiation at 40 mA and 40 kV.

2.4 Photoelectrochemical and spectroelectrochemical characterization

Photoelectrochemical (PEC) measurements were carried out using a three electrode cell with an Ag/AgCl (3.0 M NaCl) reference electrode, a platinum gauze as a counter electrode and a Princeton Applied Research 2263 (PARstat) potentiostat. The light source was a 300 W Xe lamp with an AM 1.5G illumination (1 sun). A 0.5 M Na_2SO_4 aqueous solution was used in electrochemical measurements. The potential *vs.* Ag/AgCl

was converted into the RHE scale using the following equation: $E_{RHE} = E_{AgCl} + 0.059\ pH + E^{o}_{AgCl}$, with E^{o}_{AgCl} (3.0 M NaCl) = 0.210 V at 25°C.

Incident photon to current efficiency (IPCE) measurements were carried out with a set-up similar to that of PEC experiments, with a Bausch and Lomb grating monochromator placed between the Xe lamp and the sample. A 1.23 V bias *vs.* NHE was applied and the current was measured with a 10 nm step, within the 350 and 600 nm range. The incident light power was measured at each wavelength using a calibrated photodiode connected to a Keithley 617 electrometer. The IPCE was calculated at each wavelength λ (nm) using the following equation:

$$IPCE = \frac{[1240 \times J]}{P_{\lambda} \times \lambda} \times 100$$

where J is the photocurrent density (mA cm^{-2}) and P_{λ} (mW cm^{-2}) is the power of the monochromatic light at wavelength λ.

The electrochromic experiments on $BiVO_4$ films were carried out with the same potentiostat used for PEC measurements. UV-Vis spectra under applied bias were recorded with a Jasco V650 spectrophotometer. A different tri-electrodes Pyrex electrochemical cell was used for the measurements. Here, the two opposite windows of the cell were closed on one side with the $BiVO_4$ photoanode and on the other side with a quartz window. A Pt wire was used as counter electrode and the reference was an Ag/AgCl electrode in 3 M KCl. A 0.1 M tetrabutylammonium hexafluorophosphate solution in acetonitrile was used as electrolyte.

2.5 Transient absorption spectroscopy

Femtosecond transient absorption spectroscopy was used to follow the early evolution of photogenerated charge carriers in the two separate semiconductors and to track charge transfer in the WO_3/$BiVO_4$ heterojunction. Experiments with 387 nm excitation were carried out in the Radiation Laboratory at Notre Dame University, Indiana, USA, while measurements using pump excitation with variable wavelength were recorded at the National Laboratory for Ultrafast and Ultraintense Optical Science, Politecnico di Milano, Milan, Italy. Transient absorption experiments were performed using a system based on a Ti:sapphire laser source (Clark MXR CPA-2010) generating pulses centered at 775 nm with a FWHM of 130 fs and 1 kHz repetition rate. For 387 nm pump excitation measurements 95% of the laser pulse was frequency doubled to λ = 387 nm and used as pump, while the remaining 5% was focused on a CaF_2 crystal to generate the white light probe. Different pump wavelengths were generated using the optical parametric amplification (OPA) of the chirped white light produced in a CaF_2 crystal. Briefly, a portion of the frequency doubled fundamental harmonic of the Ti:sapphire laser was focused on the CaF_2 crystal and originated the broadband seed beam. A second harmonic (SH) portion was then overlapped in space and time in a BBO β-barium borate nonlinear crystal with the focused seed. Finally, the amplified pulse was separated from the SH and the idler and used directly as the pump (480 and 500 nm) or frequency doubled (*i.e.* in the case of 450 and 460 nm pump, we doubled the amplified near IR wavelenghts). The so obtained differently colored pumps had an average bandwidth (FWHM) of *ca.* 50 nm. The detector used was a Helios transient absorption system from Ultrafast Systems. A pump energy density of 40 μJ/cm^2 was used during all experiments. Transient absorption spectra were recorded within a 1400 ps scale in the 400-800 nm range and fitted with different models, as discussed in detail in the following text.

3 RESULTS AND DISCUSSION

3.1 Characterization of the BV and W/BV series with different $BiVO_4$ thickness

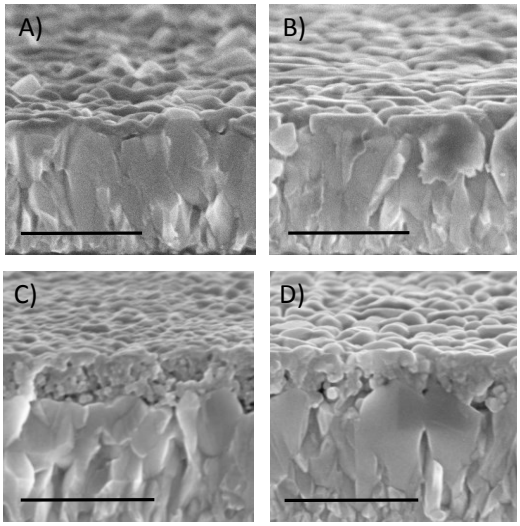

Figure 7.1. FESEM side view images of the photoanodes obtained with the sequential deposition of two and four BiVO4 layers: (A, B) directly on the FTO conductive glass substrate, and (C, D) on a 200 nm thick WO_3 layer (films BV30 and BV75 and W/BV30 and W/BV75, respectively). The scale bar is 500 nm.

The morphology of the mesoporous photoanodes employed in this study were characterized with Field Emission Scanning Electron Microscopy (FESEM). Side view pictures of the BV samples obtained with 2 and 6 $BiVO_4$ coating layers are reported in Figure 7.1A and 7.1B. In W/BV films, because the FTO asperities are completely covered by the WO_3 underlayer, the $BiVO_4$ coating results more uniform and the WO_3 layer is completely covered after only two $BiVO_4$ coatings. In both series, successive depositions led to an increase in size of the $BiVO_4$ grains forming a mesoporous architecture (see Figure 7.1C, 7.1D and Figure 7.2 for more FESEM images). The mesoporous WO_3 layer is formed by the aggregation of small grains with the diameter in the order of 17 nm, as previously reported for films obtained with the same synthetic procedure.[3]

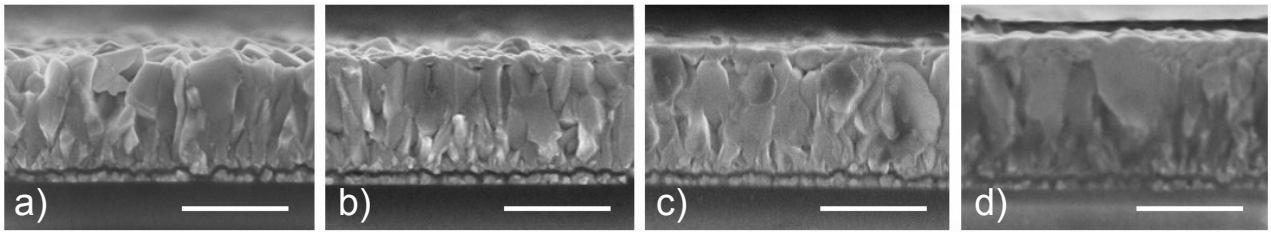

Figure 7.2. Cross section FESEM images of a) clean FTO, b), c) and d) $BiVO_4$ photoanodes prepared with the subsequent spin coatings of 2, 4 and 6 layers of $BiVO_4$ respectively. The scale bar is of 500 nm.

From the thickness measurements of the $BiVO_4$ layer in the picture reported in Figure 7.2, an absorption coefficient for $BiVO_4$ films at 420 nm can be calculated using the following equation (eqn(1))

$$A_{420} = \alpha_{420} \times d \qquad \text{eqn(1)}$$

where α_{420} is the absorption coefficient of $BiVO_4$ at 420 nm, A_{420} is the absorption at 420 nm and d is the average thickness in cm. We performed the SEM cross sectional analysis of the samples prepared with 2, 4 and 6 subsequent $BiVO_4$ depositions, while the UV-visible absorption measurements were made to obtain the absorbance of the three electrodes. The SEM images are reported in Figure 7.2; the cross section of the clean conductive glass substrate was used to determine the thickness of the pristine FTO layer. Then, to estimate the absorption coefficient, we plotted the film absorbance at 420 nm *vs.* the film thickness (Graph 7.1). From the slope the absorption coefficient of $BiVO_4$ at 420 nm (α_{420}) was calculated as 6.7 10^4 cm^{-1}.

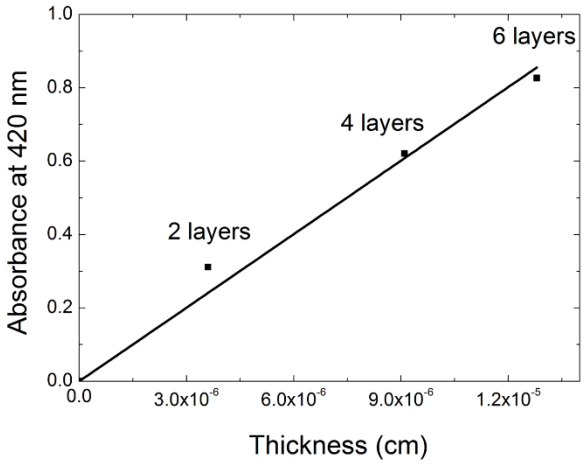

Graph 7.1. Plot of the absorbance at 420 nm of the $BiVO_4$ films prepared by 2, 4 and 6 subsequent coatings, *vs.* the film thickness.

We then used the calculated α_{420} value to estimate the films thickness from their absorbance at 420 nm. In order to avoid the contribution due to the visible light scattering typical of FTO, as baseline, we used a high transparent ZrO_2 film coated on a clean FTO

N° of coatings	$BiVO_4$ Abs	$BiVO_4$ Thickness (nm)	$WO_3/BiVO_5$ Abs	$WO_3/BiVO_5$ Thickness (nm)
1	0.09	14	0.11	16
2	0.21	31	0.20	30
3	0.33	49	0.33	50
4	0.50	75	0.50	74
6	0.76	114	0.77	115
8	1.09	163	1.07	160

Table 7.1. Absorbance at 420 nm and estimated thickness of the $BiVO_4$ layer in the $BIVO_4$ and $WO_3/BiVO_4$ films employed in our investigation.

substrate and prepared starting from $ZrO(NO_3)_2$ with a procedure similar to that reported for $BiVO_4$ films. In Table 7.1 the absorbance and the related thickness of all films employed in the investigation are reported. The thickness increases almost linearly with the number of coatings with an average increment of 21 nm per coating.

The UV-Vis absorption spectra of WO_3, BV160 and WBV160 films are reported in Figure 7.3A. In the WBV8 coupled system the extremely transparent WO_3 film is effectively sensitized up to 520 nm by coating with $BiVO_4$. The residual visible absorption over 520 nm is mainly due to lattice fringes and scattering. It is worth noting that the deposition of $BiVO_4$ in several subsequent layer deposited by spin coating gives well reproducible results also after 8 coatings in either systems, as suggested by the almost

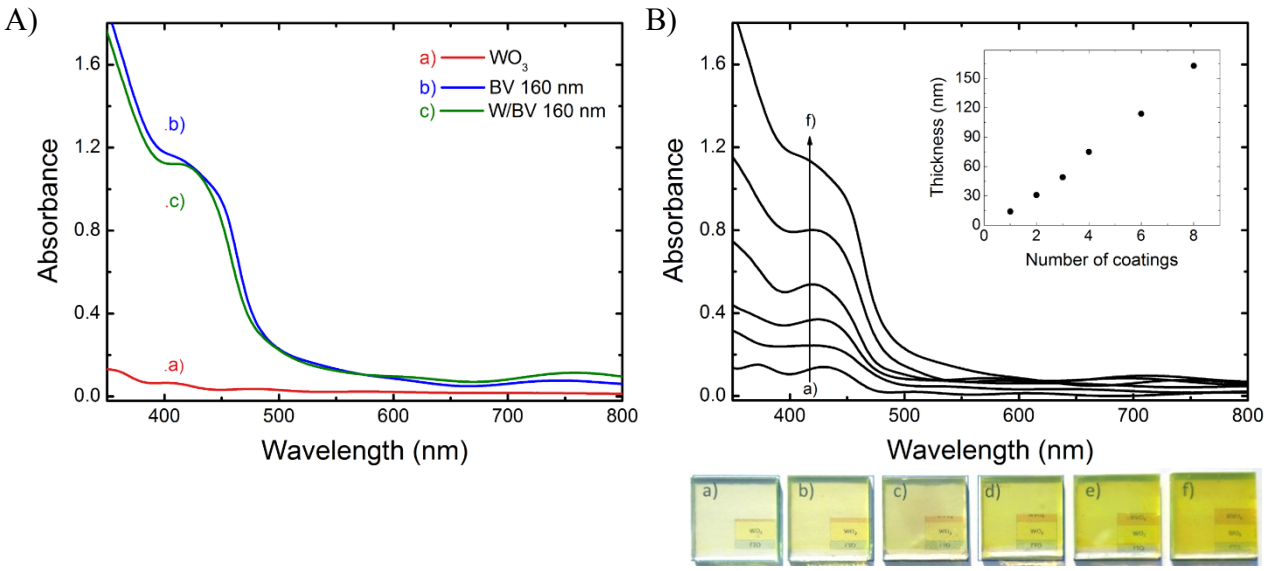

Figure 7.3. (A) Absorption spectra oxide films deposited on conducting glass (FTO) electrodes: a) WO_3, b) BV 160 nm and c) WBV 160 nm. (B) From a) to f), absorption spectra of the WBV series obtained by the subsequently deposition of $BiVO_4$ precursor. In the inset, the linear growth in thickness plotted against the number of coatings. The corresponding photographs of the samples are shown below.

superimposed absorption profiles of BV160 and WBV160. The UV-Vis absorption features and a picture of the WBV series are reported in Figure 7.3B. Absorbance increases linearly with the number of coatings, allowing a better exploitation of visible light in thicker films.

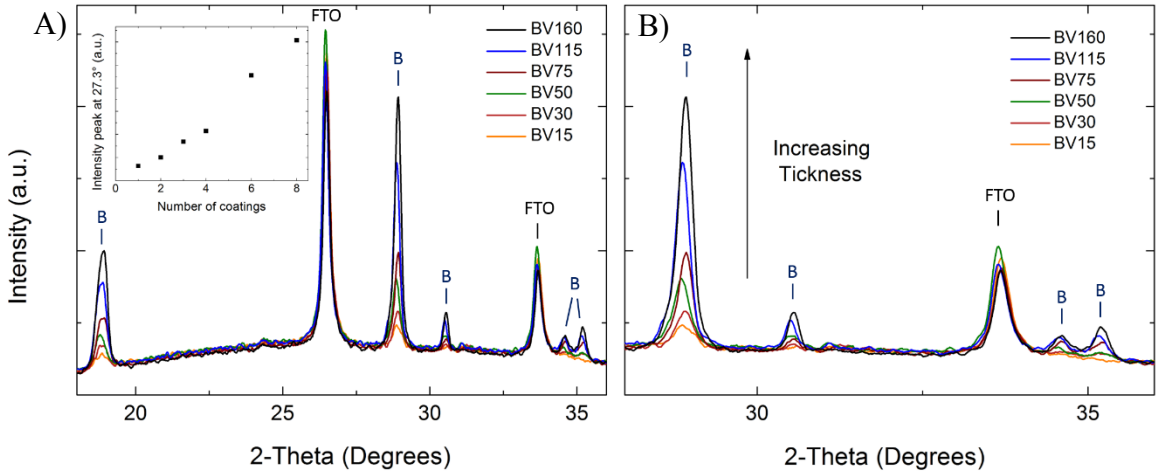

Figure 7.4. A) XRPD analysis of the BV series and B) magnification of 28 – 36° region. The typical patterns of $BiVO_4$ monoclinic scheelite as well as those of FTO are indicated in the two Figures with the B and FTO labels, respectively. Each photoanode was annealed 8 h at 500°C.

X-ray powder diffraction patterns recorded with the two series with variable thickness are reported in Figure 7.4. The patterns of both individual materials fit well with monoclinic (JCPDS 05-0363 for WO_3)[4,5] and monoclinic scheelite (JCPDS 75-1867 for $BiVO_4$)[2] structures. Figure 7.4A and the magnification for the 28 – 36 degree range in Figure 3B, show that in the BV series all diffraction peaks typical of this crystalline phase increase linearly as reported specifically in the inset for the strongest signal of $BiVO_4$ at 2θ = 27.3°. The signals of the FTO conductive glass film (2θ = 26.5° and 2θ = 33.6°) slightly decrease with

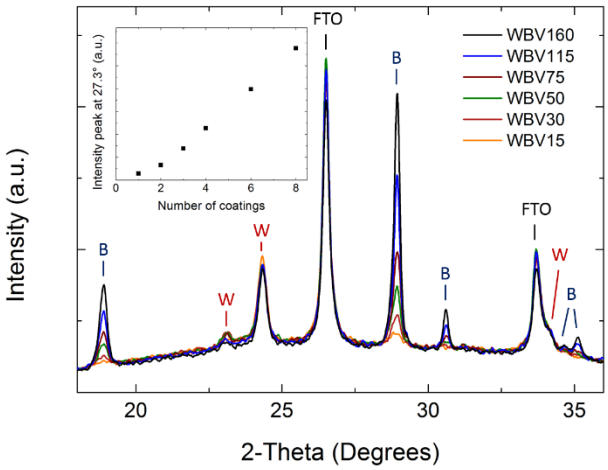

Figure 7.5. XRPD analysis of the WBV series. The typical patterns of $BiVO_4$ monoclinic scheelite and WO_3 monoclinic structure as well as those of FTO are indicated with the B, W and FTO labels respectively. Each photoanode was annealed 8 h at 500°C.

increasing the thickness of the $BiVO_4$ layer. Similarly in Figure 7.5 the reflections assigned to monocline WO_3 (2θ = 23.0°, 24.3° and 34.1°) progressively decrease with the successive coating of $BiVO_4$ layers. WO_3 patterns didn't match completely in the 2θ = 23-25 2° region, where the three closely spaced peaks typical of the monoclinic structures[6] overlap. Peak broadening should probably be attributed to non-constructive scattering due to the small crystallite size of the WO_3 film.[7,8]

A direct comparison between films of the two series with equal $BiVO_4$ thickness is reported in Figures 7.6A and 7.6B. In both couples of photoanodes (with $BiVO_4$ layers of 75 nm and 150 nm) the $BiVO_4$ peaks in the coupled system (black traces) at 2θ = 18.6, 34.5 and 35.3 degrees were lower in magnitude with respect to those of single material films (red traces). A possible explanation is that the $BiVO_4$ layer grows with a preferential orientation on the underlying WO_3 film. Nevertheless, the magnitude of the strongest peak of the monoclinic $BiVO_4$ phase is totally overlapped in the two series as, well as the peak at 30.8 degrees.

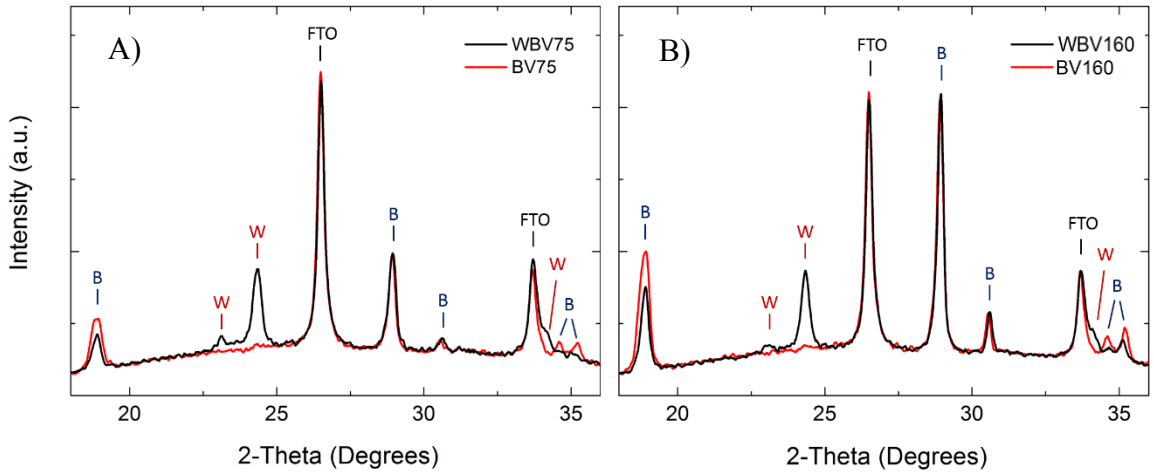

Figure 7.6. Comparison of the XRPD analysis of the BV and WBV films with equal $BiVO_4$ thickness. The two films with a A) 75 nm and B) 160 nm thick $BiVO_4$ layer are compared.

3.2 Spectroelectrochemical changes of $BiVO_4$ under an applied positive potential

Electrochromic materials have optical properties that change in response to the application of an external potential and are widely studied for the fabrication of displays or windows with tunable light transmittance. The applied bias changes the electronic configuration of the studied materials, introducing new transitions in the visible region.[9] Spectral changes under negative potentials were previously reported for semiconductors such as TiO_2, WO_3 and CdSe nanocrystals.[10–13] In the first two cases, the accumulation of trapped electrons under the application of external electric field, is due to the reduction of Ti^{4+} to Ti^{3+} in TiO_2 (or W^{6+} to W^{5+} in WO_3) at appropriate lattice sites. The new intraband transition leads to an increase of the film absorption at wavelengths longer with respect to the band gap onset and usually greater than 450-500 nm for the mentioned oxides, and in the IR region in the case of CdSe nanocrystals.

The effects of hole accumulation under positive applied potentials has been less studied. Barroso et al. reported the spectral changes of Fe_2O_3 photoanode films under the application of positive bias and found that the anodic bias results in the formation of a well-defined positive feature peaking at 580 nm.[14,15] The appearance of such new positive absorption signal at potentials only slightly anodic to the flat band potential suggested the assignment of this transition to intra-bandgap states close in energy to the hematite conduction band. Moreover, this allowed the authors to clearly attribute the transient absorption signal observed with this materials (either in isolated films or under positive bias) to the same intra-bandgap states. In our study we used spectroelectrochemical experiments with a similar purpose.

Electrochromic tests on $BiVO_4$ films were carried out in acetonitrile, in order to avoid the narrower potential stability window of water. As depicted in Figure 7.7A the cyclic voltammogram of the $BiVO_4$ film showed a broad cathodic peak starting around 0.7 V vs Ag/AgCl and becoming more pronounced for potentials higher than 1.1 V, while no well-defined anodic peaks were observed at the applied potentials. The positive feature in the voltammogram can be accounted for the oxidation of $BiVO_4$, with the consequent accumulation of PF_4^- at the surface (Reaction A).

$$BiVO_4 \longrightarrow BiVO_4^+ [PF_6]^- + e- \qquad \text{Reaction (A)}$$

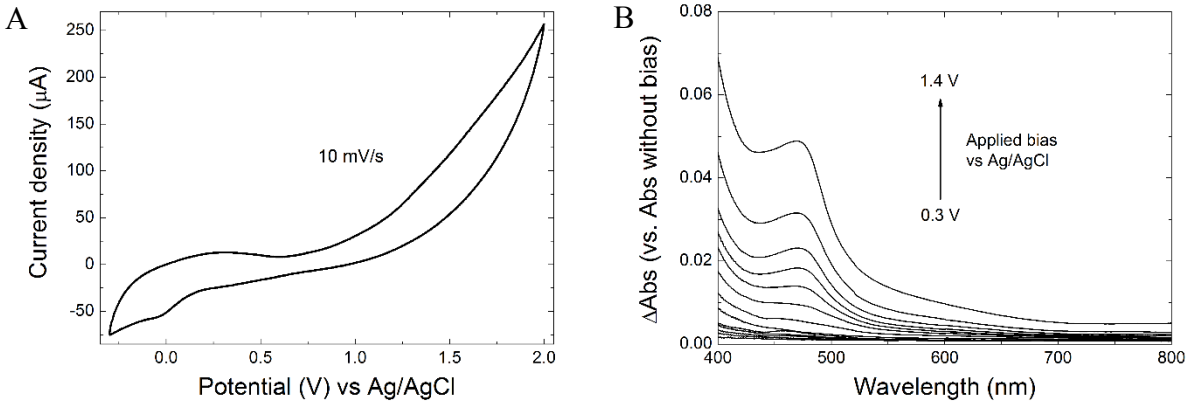

Figure 7.7. A) Cyclic voltammogram of a $BiVO_4$ film measured with a sweep rate of 10 mV/s in an acetonitrile solution containing 0.1 M a tetrabutylammonium hexafluorophosphate. B) UV-Vis absorption spectra for a $BiVO_4$ film at different positive potentials (vs Ag/AgCl) measured after a 60 s polarization with 100 mV steps. The spectrum recorded in the absence of applied bias was used as baseline.

The redox process in reaction A induces a change in the UV-Vis absorption spectrum of the $BiVO_4$ electrode associated to the formation of holes as $BiVO_4^+$, due to the extraction of electrons as a consequence of the applied positive bias.

The differential absorption spectra (ΔA) of the $BiVO_4$ film recorded after a 60 s polarization at different applied potentials are reported in **Figure 7.7B**. The spectrum without applied bias was used as a reference. The absorption increases with increasing the applied bias. The observation of a positive absorption signal at potential anodic the

flat band potential indicates that this feature arises from the oxidized form of intra-band states of $BiVO_4$. At low applied potentials a broad feature rises over the entire spectral window while at bias higher than 0.8 V a shoulder peaking at 470 nm becomes more pronounced. Such potentials are largely anodic to the flat band potential of $BiVO_4$ (0.02 V vs RHE)[3], therefore the rise of such positive absorption features with the application of increasing positive potentials can be assigned to the formation of oxidized states at energies few hundreds of meV above the $BiVO_4$ valence band. In the absence of an electrical field, these intraband states are occupied by electrons, while, after the application of an adequate bias, they are depopulated and a new optical transition, involving electrons from the $BiVO_4$ valence band, is now possible. As we discuss in the next section, the spectral changes of $BiVO_4$ upon pump excitation peak at 470 nm and have features similar to that obtained in electrochromic experiments. Therefore the photoinduced absorption spectra can be clearly attributed to the same intraband gap states that acts as hole trap sites.

3.3 fs-TAS experiments with different $BiVO_4$ thickness in the BV and WBV series

Our strategy to measure the charge carrier interaction between the two oxides in the coupled system is to compare the excited state dynamics in $BiVO_4$ alone and in the WO_3/$BiVO_4$ heterojunction film. On the here studied timescale, only the processes previously described by Ravensbergen et al. for this material are at work in the films containing $BiVO_4$ alone. First, hole diffusion and trapping (k_{h-dif}) at surface trap sites gives rise to the ΔA build up, in a few ps timescale. Then trapped holes can recombine with two distinct paths, one involving hot electrons and occurring during the first tens of ps (k_1) and the second occurring with timescale of nanoseconds and accounting for the

slow recombination with thermalized electrons at the bottom of the conduction band (k_2).[1] In the coupled system, due to the suitable band alignment, the injection of photoexcited electrons from the conduction band of $BiVO_4$ to the conduction band of WO_3 (k_{inj}) is a new viable path, leading to the spatial separation of the excited charges and potentially to longer lived charge carriers that are usually invoked as responsible for the better PEC performances of the studied system. On the other hand two more relaxation channels are available in heterojunction photoanodes: the back transfer (k_{bck}) to the valence band of $BiVO_4$ of the electrons previously injected from the $BiVO_4$ CB to the WO_3 CB and the direct injection of the photopromoted electrons in the WO_3 CB to the $BiVO_4$ VB (k_{w-inj}). The latter channel is feasible only if the incident photons are enough energetic to allow WO_3 band gap excitation (*i.e.* with wavelengths shorter than 450 nm)

Femtosecond transient absorption spectroscopy is a unique and powerful pump and probe technique that allows to directly follow the dynamics of photoexcited states in many different molecular systems.[16–18] Briefly in this pump-probe technique the sample is excited by an intense laser pump pulse; then a white light laser pulse probes the excited state of the sample after a precisely defined delay time. Here we employed such technique in order to track the events following photon absorption in both BV and WBV series. To better study the charge carrier dynamics in the two series we used different pump energies.

We evaluated the charge carriers dynamics in $BiVO_4$. Such material shows a transient ΔA positive feature extending in all visible range over 450 nm and peaking at 470 nm (see Figure 7.8). The photoinduced absorption has been previously ascribed to surface trapped holes by carrying out transient absorption experiments with the film in contact with a solution containing a hole scavenger and has been definitively attributed with the electrochromic measurements reported in the previous Section. The negative ground state photobleaching partially overlaps with the transient hole signal and has a minimum at 420 nm, in relation with the absorption maximum in the UV-Vis spectra (see Figure 7.2). The positive signal below 400 nm can be explained considering the spectral changes reported in Figure 6B for electrochromic experiments, where the positive applied bias generate a broad positive ΔA at all the investigated wavelengths. Therefore we suggest that in TAS spectra the photobleaching burns a hole in the photoinduced ΔA positive signal. The ΔA transient spectra of the two $BiVO_4$ films with thickness of 15 and 160 nm recorded at their ΔA maxima (8 and 23 ps after 387 nm pump excitation) are reported in Figure 7.8B. The positive photoinduced absorption increases with increasing the film thickness, consistently with the greater surface area in the thicker mesoporous film and consequently larger number of surface trap sites. Photobleaching does not change in magnitude because the ratio of absorbed photons does not change with thickness (the extinction coefficient is not thickness dependent).

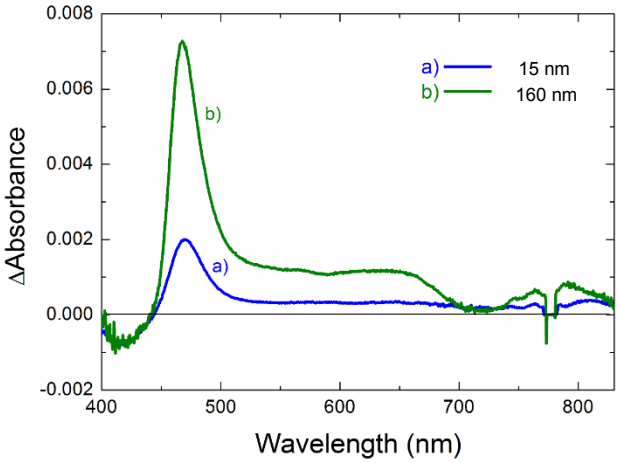

Fig. 7.8. Transient absorption spectra of $BiVO_4$ electrodes with thickness of a) 15 nm and b) 160 nm recorded at their ΔA maxima, respectively 8 and 23 ps after 387 nm pump excitation.

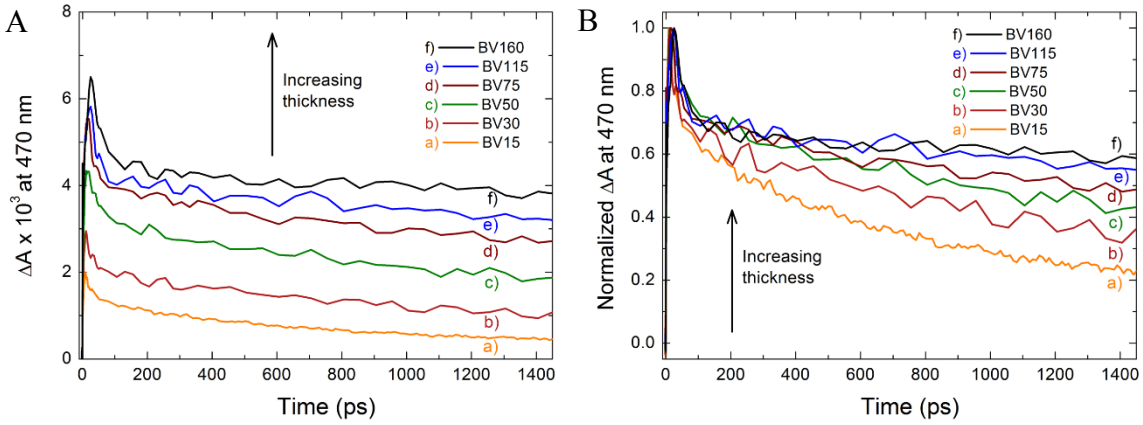

Figure 7.9. (A) Not normalized transient absorption decay traces recorded at 470 nm and (B) normalized transient decays, respectively (B), the first 60 ps following laser excitation and (C) decay traces in a 1400 ps range. (D) Sweep voltammetry photoelectrochemical experiments recorded with electrolyte 0.5M Na_2SO_4.

The transient absorption technique allowed us to observe the dynamics of photoinduced species by following the ΔA in time at a single wavelength. In this case we follow the trapped holes signal at 470 nm. The not normalized ΔA time evolution traces recorded after 387 nm pump excitation for films of the BV series with variable thickness are reported in Figure 7.9A. As already discussed the magnitude of ΔA rises along with thickness because of the increased number of surface trap states. While we observed a linear growth from trace a) to d), the ΔA growth seems to reach a maximum for thicker films (the difference in ΔA between trace d) and f) is comparable with the difference between trace a) and b), while the increase in thickness for the two couple of films is 85 nm and 15 nm respectively). This is consistent with the fact that in thicker films the mean distance between trap sites and the excitation sites is approaching the hole diffusion limit[19] of $BiVO_4$ and hence only holes photogenerated at a distance from the surface smaller or equal to that limit can travel to the trap sites.

The normalized ΔA signals are reported in Figure 8B. The ΔA decay of the normalized kinetic traces was fitted to a biexponential decay model, eqn (2)

$$y = A_1\, e^{-t/\tau_1} + A_2\, e^{-t/\tau_2} \qquad \textbf{eqn (2)}$$

where τ_1 and τ_2 are the two time constants of the fast and slow decay processes (k_1 and k_2), A_1 and A_2 are the weighted coefficients representing the contribution of the decay lifetimes to the overall decay. Because hole trapping occurs at least one and two orders of magnitude faster than k_1 and k_2, respectively, we decided to fit the data after the conclusion of hole trapping, for simplicity. The fitting parameters for all films of the BV series are reported in Table 7.2. The weight of the two decay processes is independent of the film thickness, with 30% of the holes decaying within the fast decay process and the remaining 70% with the long decay process. The fast decay time constant is not affected by the thickness of the $BiVO_4$ film and has an average value of *ca.* 30 ps; hence the hole trapping process occurring in the early stage (that is thickness dependent) is not influencing this first recombination channel. This fast decay involves the recombination between hot electrons and the already trapped holes. Since we pumped all films at the same wavelength and with the same energy density, it is reasonable that we obtained the same τ_1 and A_1 because we photoexcited the same ratio (depending on pump energy density) of the electrons over the $BiVO_4$ CB always with the same excess of energy (depending on the pump wavelength).

	BV15			BV30			BV50			BV75			BV115			BV160		
A1	33%	±	4%	32%	±	5%	30%	±	4%	31%	±	5%	30%	±	6%	33%	±	4%
τ1	28	±	2	22	±	3	47	±	4	22	±	2	20	±	2	33	±	3
A2	67%	±	1%	68%	±	1%	70%	±	1%	69%	±	1%	70%	±	1%	67%	±	1%
τ2	1270	±	19	2028	±	94	2719	±	114	3555	±	160	5514	±	378	9658	±	947
Tau Average	860	±	13	1380	±	64	1925	±	81	2469	±	111	3885	±	267	6455	±	633

Table 7.2. Summary of the fitting parameters relative to the decay of the transient signal recorded at 470 nm for the $BiVO_4$ films with different thickness. The decays were fitted with a biexponential equation.

Surprisingly, the holes lifetime increases with increasing the film thickness, suggesting that in thicker films photopromoted electrons are less prone to recombine with surface

trapped holes. Therefore in $BiVO_4$ charge recombination is limited by electron diffusion. In other words, while in thin films thermalized electrons have better chances to diffuse to the surface and recombine with trapped holes, in films with increased thickness the recombination process is less likely because, in order to recombine with trapped holes, electrons need to cover a distance precluded by their low mobility in $BiVO_4$. The role of long-lived holes have been suggested in many study to be crucial in order to efficiently carry out the slow water oxidation process. The evidence that holes become longer living in films with increased $BiVO_4$ thickness should be correlated to the better PEC properties described for optimized films in other reports. [20–22] The increase in trapped holes lifetime becomes less noticeable for films exceeding a $BiVO_4$ thickness of 75 nm, supporting the fact that charge mobility is a limiting factor also in hole trapping and that only holes photogenerated at a distance from the surface close to their diffusion limit can be trapped. Thus the ratio of charge carriers that undergo recombination becomes constant for a $BiVO_4$ thickness greater than this limit.

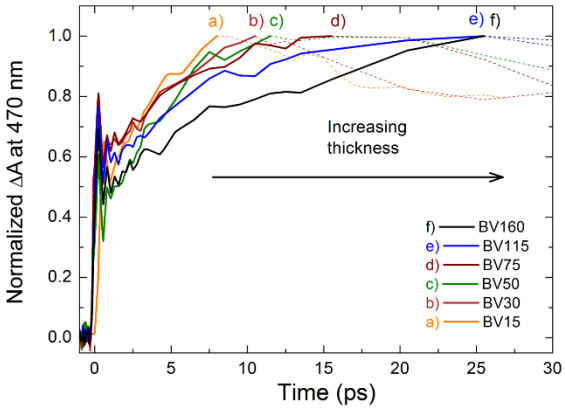

Figure 7.10. Normalized transient decays recorded at 470 nm, for the first 30 ps after pump excitation.

The ΔA build up occurring in the early stage following pump excitation is shown in Figure 7.10. 50-60% of the holes get trapped in the first ps, with a time evolution which cannot be resolved with the fs-TAS equipment used for the present investigation. The ΔA growth is highly dependent on the film thickness and the maximum population of trapped holes is reached at longer times along with thickness increase (ranging from 8 ps in BV15 up to 25 ps in BV115 and BV160 films). With Increasing the film thickness, the formation of

trapped holes takes longer because the holes have to travel longer from the photoexcitation site to the trap sites. The similar buildup duration observed in the two thicker samples confirm that in such films hole trapping is limited by holes' mobility.

To extract more information on the charge carrier dynamics in the coupled system, we performed fs-TAS experiments with different excitation wavelengths on the samples having the optimized $BiVO_4$ thickness (75nm) and leading to the best performing heterojunction photoanode in our study (*vide infra*). We evaluated the charge carrier dynamics in the two systems by exciting selectively only $BiVO_4$ or both semiconductors simultaneously, using respectively pump having photon energy lower or greater than the WO_3 band gap. The decay traces of the two systems obtained using four different pumps are reported in Figure 7.11. When $BiVO_4$ was excited selectively with 500 nm photons in the coupled system, the holes lifetime gets extremely extended with respect to that detected for the film containing only $BiVO_4$ and, except for the fast decay process, no further decay was detectable in the timescale studied. Thus electrons photopromoted in the CB of $BiVO_4$ are delocalized through the injection into WO_3 CB. This injection leads to a retarded recombination. To the best of our

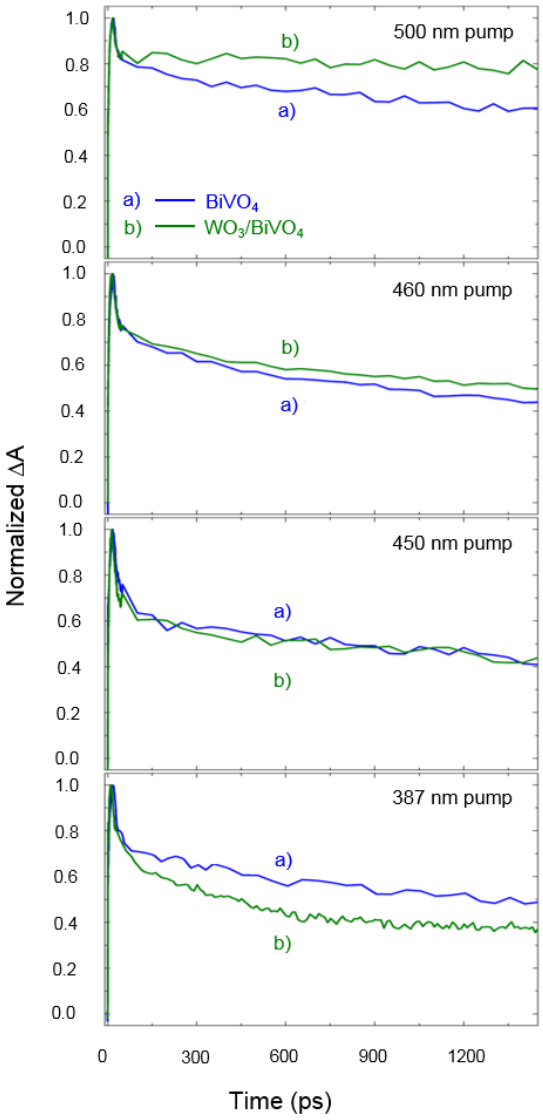

Figure 7.11. Dependence on the pump wavelength of the normalized transient kinetics recorded at 470 nm in the BV75 and WBV75 films. The four pump wavelengths used are, from the top, 500 nm, 460 nm, 450 nm and 387 nm.

knowledge, this is the first direct observation through fs-TAS, that charge separation in this coupled system leads to the increase in charge carriers lifetime. By increasing the energy of the pump photons, the lifetime of trapped holes in the heterojunction system decreases and for 450 nm pump the decay profiles in the two systems are almost identical. On the other hand, by exciting both oxides with a 387 nm photons, we observed that trapped holes in the heterojunction system recombine faster than in $BiVO_4$ alone, hence a new recombination channel is now open. Furthermore, our investigation point out that the holes' lifetime is wavelength dependent. In the next Section, using the information we

extracted through fs-TAS, we propose a scheme for the interfacial charge interaction occurring between the two oxides in heterojunction photoanodes.

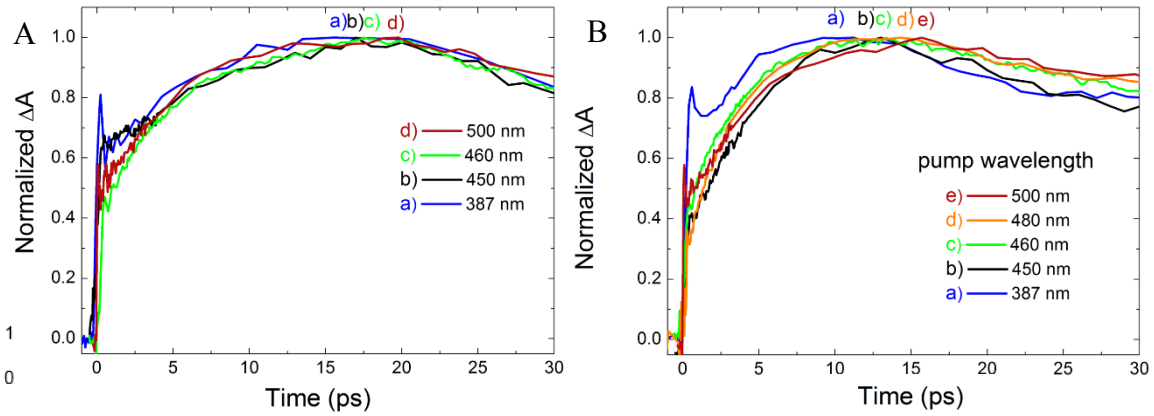

Figure 7.13. (A) Buildup of the transient signal recorded at 470 nm, due to hole trapping in the 30 ps following excitation with different wavelength pumps for A) BV75 and B) WBV75.

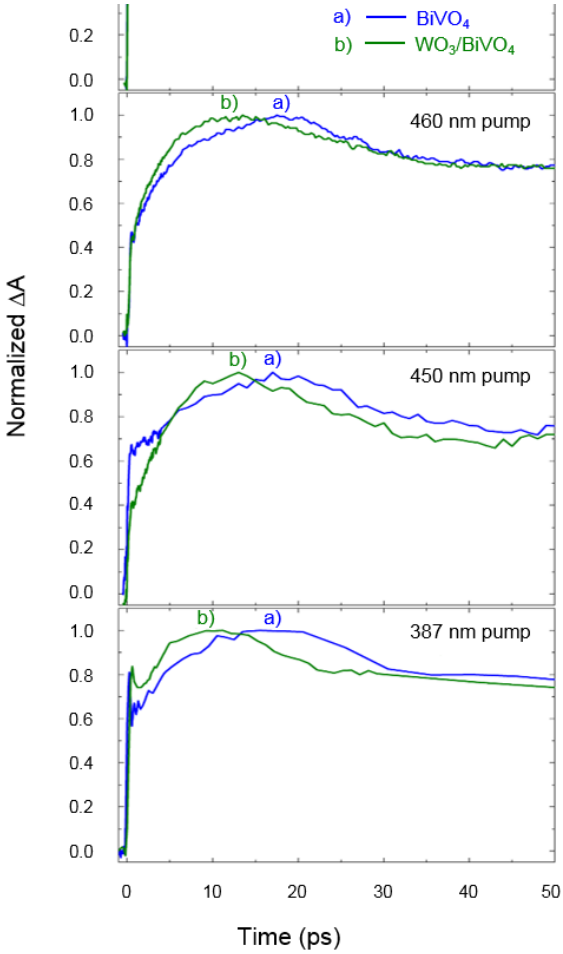

Figure 7.12. Pump wavelength dependence on the normalized transient signal kinetic at 470 nm in the BV75 and WBV75 films during the first 50 ps after pump excitation. The four pump wavelengths used are, from the top, 500 nm, 460 nm, 450 nm and 387 nm.

The comparison of the ΔA buildup in the first 50 ps following pump excitation in the two studied systems is reported in Figure 7.12 and Figure 7.13. Holes trapping is found to be substantially independent of the excitation wavelength in BV75 (see Figure 7.13A for the direct comparison between the dynamics recorded with the four pumps used). On the other hand, in the coupled system, while the buildup becomes faster at wavelengths shorter than 500 nm, with 500 nm excitation the two kinetic traces are almost overlapped (see also Figure 7.13B). The valence band alignment between the two oxides allows interfacial hole transfer from WO_3 to $BiVO_4$. Therefore it is

reasonable that with excitation enough energetic to excite both semiconductors, holes injection from WO_3 VB to $BiVO_4$ VB takes place. Pumps centered at wavelengths shorter (387 nm) or close (450 and 460 nm) to the absorption edge of WO_3 induce the formation of holes in WO_3 VB. Subsequently holes can be transferred to the valence band of $BiVO_4$ contributing to the overall trapping process. This hole injection process, as well as k_{inj}, represents a beneficial charge exchange path, potentially leading to a slower recombination of the photogenerated charge carriers.

The results of our fs-TAS study employing different excitation wavelengths (Figure 7.14) are in agreement with the model suggested by Ravensbergen et al. and discussed at the beginning of this Section.[1] The thermalization of high-energy (hot) photoexcited electrons depends on the excitation wavelength. Electrons excited by short wavelength pumps possess a larger energy excess over the $BiVO_4$ CB than electrons excited with less energetic pumps. Thus hot electrons relaxation takes longer in the former case. High-energy mobile hot electrons have better chances to recombine with trapped holes than hot electrons generated by the absorption of less energetic photons. In Figure 7.14A, the weight of the fast decay process (occurring in the first 100 ps following pump excitation) in photoexcited BV75 decreases with increasing the pump wavelength, in correlation with the lower energy excess of electrons

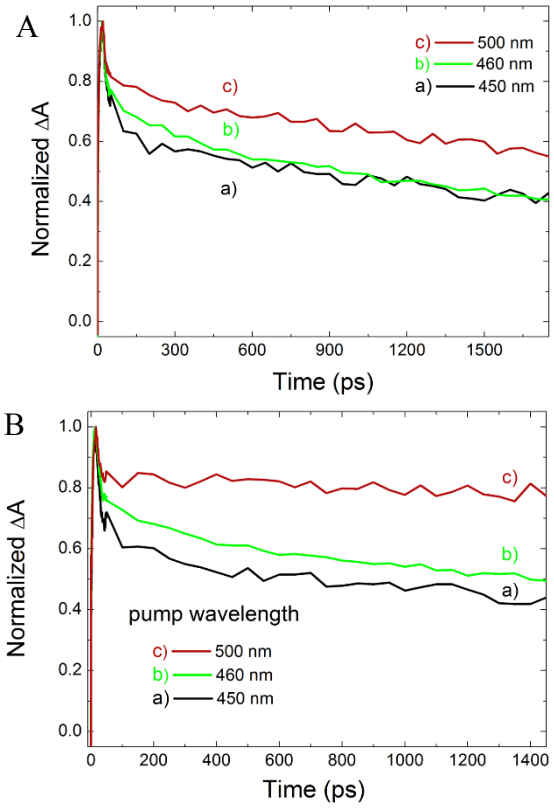

Figure 7.14. Transient signal traces recorded at 470 nm after excitation with pumps with different wavelengths for: A) BV75 and B) WBV75.

photopromoted by less energetic photons. After hot electrons thermalization to the bottom of the $BiVO_4$ conduction band, ΔA decays similarly, as suggested by the almost parallel decay traces. The wavelength dependence of the fast decay process for the WBV75 film is reported in Figure 7.14B. As expected the magnitude of the fast decay process decreases for longer wavelengths, while the long decay component becomes slower, as previously discussed.

Finally, we studied the electronic interaction between excited WO_3 and $BiVO_4$ in the WBV series as a function of $BiVO_4$ thickness, performing fs-TAS experiments with 387 nm pump excitation. Such wavelength is enough energetic to excite both semiconductors. From this set of measurements we obtained useful information on the $BiVO_4$ thickness dependence of the k_{w-inj} in the heterojunction films. Normalized ΔA kinetic traces and the magnification of the normalized buildup are reported in Figure 7.15A and 7.15B.

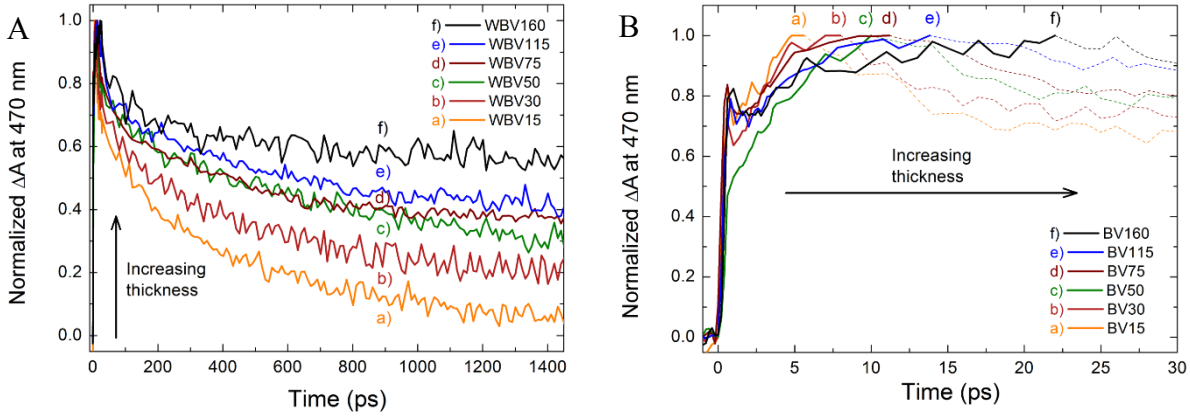

Figure 7.15. Decay traces of the transient signal recorded at 470 nm after excitation with 387 nm pump for the WBV series. A) Normalized transient decays and B) magnification of the absorption build up in the first 30 ps after the pump pulse

Similarly to the BV series both, hole trapping and the overall recombination process become slower with increasing the $BiVO_4$ thickness. The comparison between the kinetic traces in films of the two series with equal $BiVO_4$ thickness are reported in Figure 7.16A while the buildup in Figure 7.16B. Clearly thin $BiVO_4$ films are more influenced than thick

films by the detrimental recombination channel that involves the direct injection of photoexcited electrons from the WO_3 CB to $BiVO_4$ VB (k_{w-inj}). A third exponential decay is present in the heterojunction films and is active on a timescale the fast and long recombination processes typical of $BiVO_4$. Figure 7.16A, shows that with increasing the $BiVO_4$ thickness, the contribution of the third decay process is decreasing and for a $BiVO_4$ thickness of 160 nm the decay of the transient signal seems to be almost unaffected by the presence of WO_3.

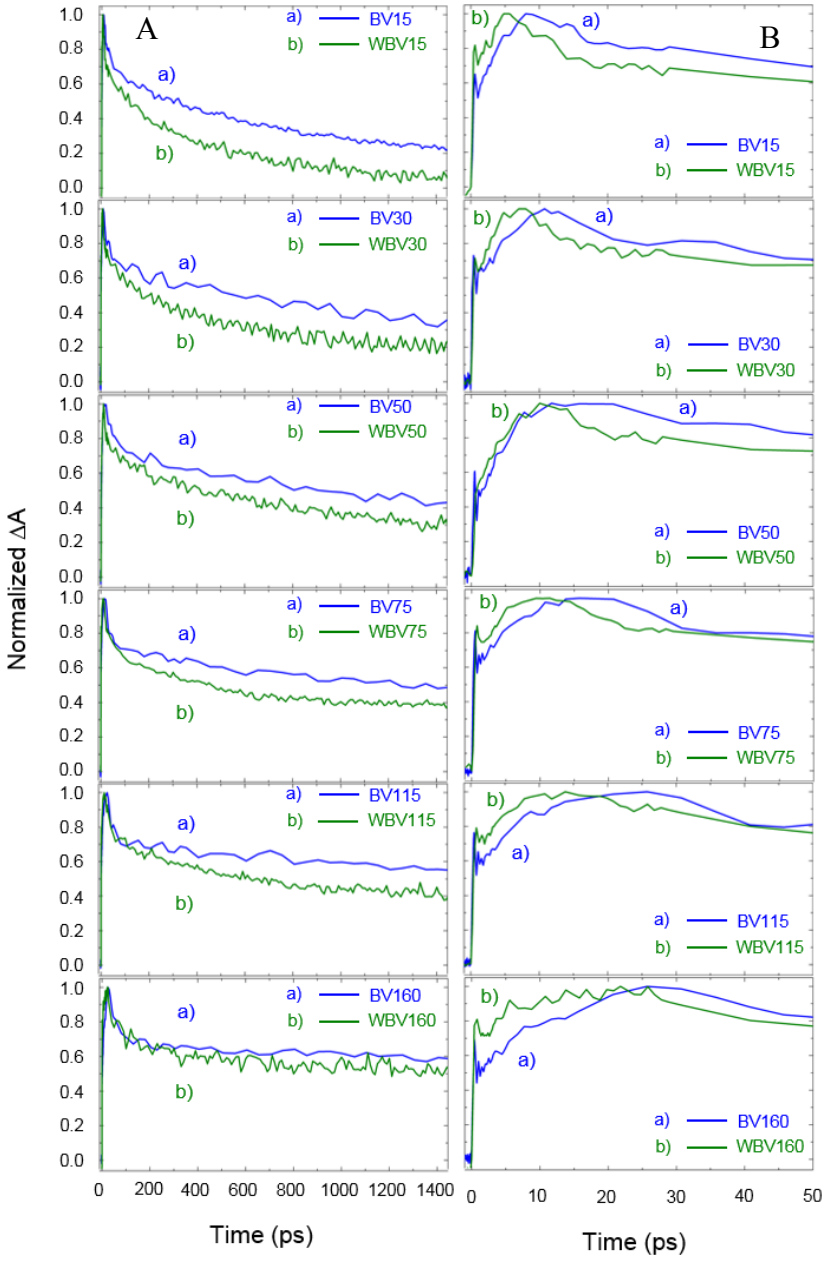

Figure 7.16. Thickness dependency of the normalized transient kinetics recorded at 470 nm in the BV and WBV series during the A) 1.4 ns and b) the first 30 ps after pump excitation.

In order to extract valuable information from the transient signal reported in Figure 15A, ΔA decays were fitted to a triexponential decay model, **eqn (3)**

$$y = A_1\, e^{-t/\tau_1} + A_{w-inj}\, e^{-t/\tau_{w-inj}} + A_3\, e^{-t/\tau_3} \qquad \textbf{eqn (3)}$$

where τ_1, τ_2 and τ_{w-inj} are respectively the two time constants of the fast and slow decay processes (k_1 and k_2) typical of $BiVO_4$ and the new decay process (k_{w-inj}) introduced by the presence of WO_3, A_1, A_2 and A_{w-inj} are the weighted coefficients representing the contribution of the decay lifetimes to the overall decay. As well as the fitting of the BV series we decided to fit the data after the conclusion of hole trapping process. We assumed that the fast and slow decay processes are not affected by the presence of WO_3 and we fitted each WBV transient kinetics using the τ_1 and τ_2 parameters previously obtained with the fitting of the kinetic traces recorded with photoanodes having corresponding $BiVO_4$ thickness in the BV series. Therefore, in the fitting we let free to calculate only τ_{w-inj}, the time constant relative to the new deactivation channel.

The fitting parameters are reported in Table 3. For all studied films we found that the new process have a characteristic time constant τ_{w-inj} of *ca.* 330 ± 110 ps, with a weight decreasing with increasing the $BiVO_4$ thickness.

	BV15			BV30			BV50			BV75			BV115			BV160		
A1	38%	±	6%	26%	±	10%	27%	±	7%	25%	±	6%	24%	±	1%	23%	±	13%
τ1	28	±	0	22	±	0	47	±	0	22	±	0	20	±	0	33	±	0
$A_{w\text{-}ing}$	**49%**	**±**	**7%**	**31%**	**±**	**5%**	**21%**	**±**	**12%**	**20%**	**±**	**5%**	**25%**	**±**	**1%**	**16%**	**±**	**15%**
$\tau_{w\text{-}ing}$	**386**	**±**	**24**	**266**	**±**	**29**	**617**	**±**	**170**	**209**	**±**	**19**	**305**	**±**	**19**	**203**	**±**	**42**
A2	13%	±	33%	43%	±	2%	51%	±	7%	55%	±	1%	51%	±	1%	61%	±	1%
τ2	1270	±	0	2028	±	0	2719	±	0	3555	±	0	5514	±	0	9670	±	0
Tau Average	406	±	12	953	±	9	1542	±	36	2007	±	4	2870	±	14	5978	±	7

Table 7.3. Summary of the fitting parameters for the decay of the transient signal recorded at 470 nm for the WBV series. The decays were fitted with a triexponential equation using τ_1 and τ_2 values obtained for the films of the BV series having the same $BiVO_4$ thickness. We left the fitting program free to determine τ_{w-inj} only.

3.4 Proposed model for the interfacial charge transfer in the WO_3/$BiVO_4$ heterojunction

The extended lifetime found in the coupled system excited with pump energy smaller than the WO_3 band gap directly proves, for the first time, that the injection of photoexcited electrons from the conduction band of $BiVO_4$ to the CB of WO_3 (k_{inj}) leads to the effective space separation of the e^-/h^+ pairs (see Figure 7.11). Longer living holes are able to more readily induce the four-hole water oxidation reaction to O_2. On the other hand, photons with energy greater than the band gap of WO_3 excite both semiconductors and the recombination (k_{w-inj}) between electrons photoexcited in the CB of WO_3 and photogenerated holes in the valence band (VB) of $BiVO_4$ becomes a viable detrimental process, leading to the decrease of trapped holes lifetime in the coupled system. After electrons are injected from the $BiVO_4$ CB to the WO_3 CB, a second undesired pathway is their backward transfer to the $BiVO_4$ VB.

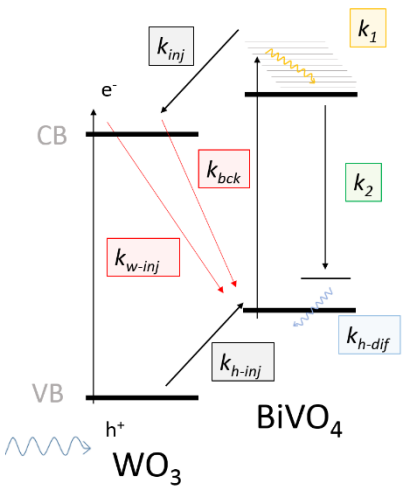

Scheme 7.1. Proposed model for the interaction between the two metal oxides in the heterojunction system. k_{h-dif}, k_2 and k_3 are the three rate constants of the processes occurring in $BiVO_4$: holes relaxation and trapping, hot electrons relaxation and recombination between trapped holes and the electrons at the bottom of the CB. k_{inj}, k_{bck}, k_{h-inj} and k_{w-inj} are the four rate constants relative to the proposed processes involved in the coupled system: injection of photoexcited electrons from the CB of $BiVO_4$ to the CB of WO_3, their possible successive back electron transfer from the WO_3 CB to the VB holes in $BiVO_4$, injection of photogenerated holes from WO_3 VB to $BiVO_4$ VB and direct recombination between photoexcited electrons in the CB of WO_3 and trapped holes in $BiVO_4$ VB.

The results of the wavelength-dependent interaction between WO_3 and $BiVO_4$ in the heterojunction system allowed us to suggest a new scheme for the electronic interaction between the two oxides, which is reported in Scheme 7.1. For excitation energy smaller than the WO_3 band gap, k_{w-inj} is an issue and leads to a decreased holes lifetime. For excitation less energetic than the WO_3 band gap, electrons can only be excited in the CB of $BiVO_4$. Therefore holes are not generated in the WO_3 VB and electron injection from

the $BiVO_4$ CB to the WO_3 CB leads to the beneficial separation of e^-/h^+ pairs and the subsequent increase of trapped holes lifetime.

Finally, in the next section, we validate the transient spectroscopy data and the proposed model by carrying out photoelectrochemical experiments with the two BV and WBV series.

3.5 Photoelectrochemical performances of the two series

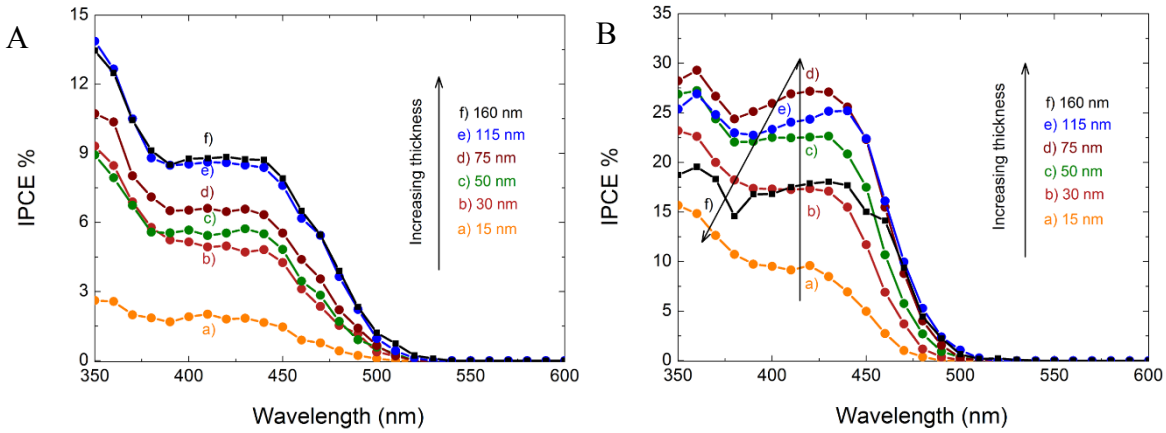

Figure 7.17. IPCE measurements of the A) BV and B) WBV series, recorded in Na_2SO_4 0.5 M aqueous solution and an applied bias of 1.23 V vs RHE.

To validate the correlation between fs-TAS data and the photocatalytic performances of the studied electrodes, we carried out photoelectrochemical (PEC) experiments in Na_2SO_3 0.5 M electrolyte solution using the films of both series of photoanodes. We found a correlation between the increase of trapped holes lifetime (with increasing $BiVO_4$ thickness) and the improved PEC performances of thicker films for either series.

IPCE measurements recorded at 1.23 V vs RHE for both series are reported in Figure 7.17A and 7.17B. Due to the charge separation in the heterojunction system, the WBV series works dramatically better than the BV series and the increase in the $BiVO_4$ thickness gives rise to a better exploitation of visible light and to the red shift of the photocurrent onset. The IPCE increase should be directly correlated to the longer living holes, as found through fs-TAS measurements. Moreover in the BV series, IPCE values

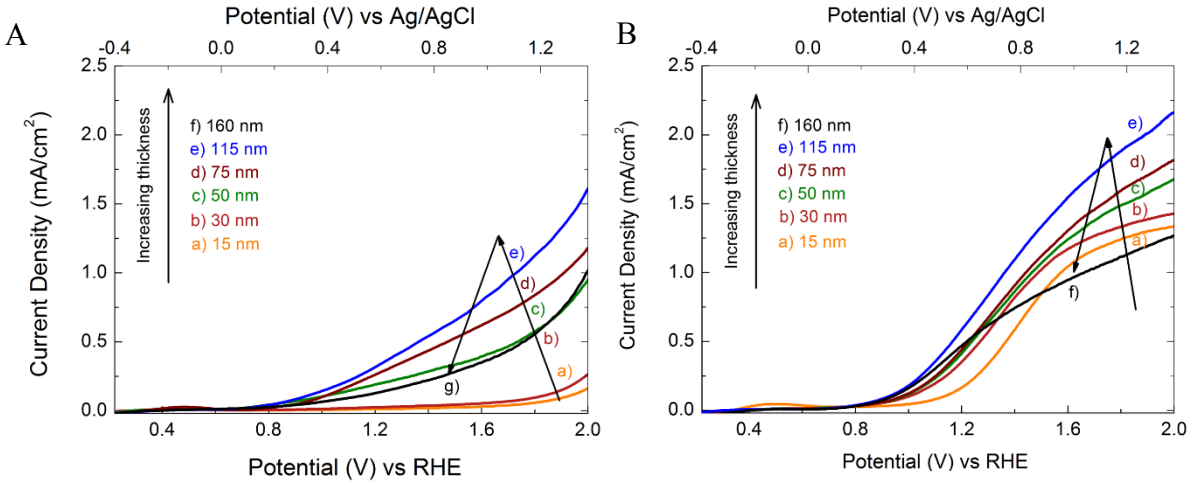

Figure 7.18. Linear sweep voltammetry under AM 1.5G irradiation of the A) $BiVO_4$ and B) $WO_3/BiVO_4$ photoanodes, recorded in Na_2SO_4 0.5 M aqueous solution, with a scan rate of 10 mV s^{-1}. In both systems the photocurrent increases with increasing the amount of the coated $BIVO_4$ up to a limit (115 nm) for which the thickness of the $BiVO_4$ layer becomes larger than the average path of the photopromoted charge carriers.

increase markedly in the first thinner films, while BV 160 show efficiency only slightly higher than BV115, in a way similar to the fs-TAS traces reported in Figure 7.9. Among the WBV films, WBV75 shows the best efficiency and WBV115 has similar performances. On the other hand, the IPCE recorded with the WBV160 photoanode is extremely decreased below 450 nm. The different behavior performed by the WBV series should be ascribed to the ineffective contact between the electrolyte solution and the WO_3 underlayer in photoanodes with a $BiVO_4$ thickness exceeding 115 nm. The optimal balance between visible light absorption and charge carriers recombination in the heterojunction films with a thickness ranging between 75 and 115 nm leads to a maximized IPCE.

Sweep voltammetry measurements under simulated solar light AM 1.5G irradiation are reported in Figure 7.18A and 7.18B. Both series show an increase in the performance for films with increasing thickness, which is directly correlated to the increase of the holes' lifetime found through fs-TAS (see Figure 7.9A and 7.15A). Under AM 1.5G conditions the best performing photoanode of the BV series is BV115, while the photocurrent density

measured with BV160 is extremely low. We suggest that the different trends found between these PEC measurements and the IPCE reported in Figure 17A are due to the different photon fluxes typical of the two types of experiment. In PEC experiments under AM 1.5G irradiation the number of photons reaching the sample is three order of magnitude greater than in IPCE tests. Therefore the high photogenerated charge densities obtained in PEC experiments under simulated solar light irradiation for the BV160 photoanode are not supported by a suitable charge diffusion in the $BiVO_4$ layer, and a large number of charge carriers undergo recombination. The WBV series shows a higher current density with respect to the BV series; this enhancement is due to the beneficial charge interaction between the two oxides. Both BV160 and WBV160 photoanodes show lower current densities than WBV115, in analogy with the high photon flux used in sweep voltammetry experiments and with the diminished IPCE performances showed in Figure 7.17B. Therefore with such thickness, both charge and electrolyte diffusion are limiting factors in the WBV160 photoanode.

For the films having the optimal $BiVO_4$ thickness, we compared the IPCE measured at 1.23 V *vs* RHE with the combined electrode, with the IPCE values obtained with the single WO_3 and $BiVO_4$ photoanodes (see Figure 7.19). We evaluate the performance of the WBV160 film by means of the IPCE enhancement factor, that is the difference between the IPCE obtained with the coupled system minus the sum of the two IPCE values obtained in the two separate photoanodes.

$$IPCE\ enhancement\ (\%) = IPCE_{WO_3/BiVO_4} - (IPCE_{WO_3} + IPCE_{BiVO_4})$$

The photoresponse of the heterojunction photoanode correlates extremely well with the model proposed in Scheme 1, with the coupled system working dramatically better than the two separate materials at wavelengths close or longer than the WO_3 absorption edge (450 nm). For shorter wavelengths, the IPCE enhancement in the heterojunction photoanode is less pronounced. Moreover, for wavelengths shorter than 360 nm the contribution of k_{w-inj} predominates over k_{inj} and the coupled system is less active than the sum of the IPCEs of the two separate oxides, even with a 1.23 V applied bias. Therefore the overall photoelectrocatalytic performance of the $WO_3/BiVO_4$ heterojunction is subject to the wavelength-dependent balance between the k_{inj} and k_{w-inj} electron transfer paths.

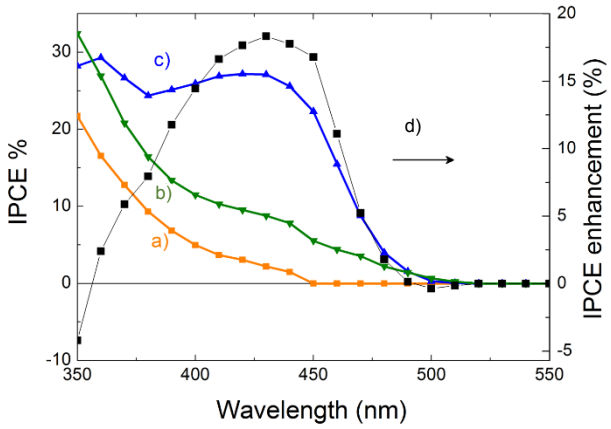

Figure 7.19. a) IPCE measurements of the WO_3 photoanode, b) sum of the IPCEs measured with WO_3 and BV75 films c) IPCE recorded with WBV75 film and d) IPCE enhancement. The IPCEs were carried out in Na_2SO_4 0.5 M aqueous solution and with an applied bias of 1.23 V vs RHE.

4. CONCLUSIONS

In this study we obtained the first demonstration through fs-TAS measurements that charge separation in the $WO_3/BiVO_4$ heterojunction systems leads to longer lived charge carriers. We observed the increase of holes lifetime subsequent to the injection of photoexcited electrons from $BiVO_4$ CB to WO_3 CB for wavelength longer than the WO_3 absorption edge and the detrimental injection of photoexcited electrons from the WO_3 CB to the $BiVO_4$ VB for excitation at wavelengths shorter than 450 nm. Hole injection from WO_3 VB to $BiVO_4$ VB can also be observed for excitation energy high enough to excite both oxides. Therefore, the beneficial charge separation is active starting from the early

ps following photon absorption. Moreover, holes lifetime was found to increase with increasing the $BiVO_4$ thickness. Such longer lived species are directly responsible of the better PEC performances obtained with thicker films in our studies and explain the better performances obtained with optimized thickness in many reports. Finally, our study based on the dependence of the charge carriers dynamics and PEC properties to the thickness of the light harvesting oxide can be adopted in order to extract many useful insights on the excited state dynamics in different novel semiconducting materials.

REFERENCES

(1) Ravensbergen, J.; Abdi, F. F.; Van Santen, J. H.; Frese, R. N.; Dam, B.; Van De Krol, R.; Kennis, J. T. M. Unraveling the Carrier Dynamics of $BiVO_4$: A Femtosecond to Microsecond Transient Absorption Study. *J. Phys. Chem. C* **2014**, *118*, 27793–27800.

(2) Su, J.; Guo, L.; Yoriya, S.; Grimes, C. A. Aqueous Growth of Pyramidal-Shaped $BiVO_4$ Nanowire Arrays and Structural Characterization: Application to Photoelectrochemical Water Splitting. *Cryst. Growth Des.* **2010**, *10*, 856–861.

(3) Grigioni, I.; Stamplecoskie, K. G.; Selli, E.; Kamat, P. V. Dynamics of Photogenerated Charge Carriers in $WO_3/BiVO_4$ Heterojunction Photoanodes. *J. Phys. Chem. C* **2015**, *119*, 20792–20800.

(4) Di Paola, A.; Palmisano, L.; Venezia, A. M.; Augugliaro, V.; Ugo, V.; Malfa, L. Coupled Semiconductor Systems for Photocatalysis. Preparation and Characterization of Polycrystalline Mixed WO_3/WS_2 Powders. *J. Phys. Chem. B* **1999**, *103*, 8236–8244.

(5) Su, J.; Guo, L.; Bao, N.; Grimes, C. A. Nanostructured $WO_3/BiVO_4$ Heterojunction Films for Efficient Photoelectrochemical Water Splitting. *Nano Lett.* **2011**, *11*, 1928–1933.

(6) Santato, C.; Odziemkowski, M.; Ulmann, M.; Augustynski, J. Crystallographically Oriented Mesoporous WO_3 Films: Synthesis, Characterization, and Applications. *J. Am. Chem. Soc.* **2001**, *123*, 10639–10649.

(7) Pokhrel, S.; Birkenstock, J.; Schowalter, M.; Rosenauer, A.; Mädler, L. Growth of Ultrafine Single Crystalline WO_3 Nanoparticles Using Flame Spray Pyrolysis. *Cryst. Growth Des.* **2010**, *10*, 632–639.

(8) Pokhrel, S.; Simion, C. E.; Teodorescu, V. S.; Barsan, N.; Weimar, U. Synthesis, Mechanism, and Gas-Sensing Application of Surfactant Tailored Tungsten Oxide Nanostructures. *Adv. Funct. Mater.* **2009**, *19*, 1767–1774.

(9) Yamase, T. Photo- and Electrochromism of Polyoxometalates and Related Materials. *Chem. Rev.* **1998**, *2665*, 307–325.

(10) Rothenberger, G.; Fitzmaurice, D.; Griitzel, M. Spectroscopy of Conduction Band Electrons in Transparent Metal Oxide Semiconductor Films: Optical Determination of the Fiatband Potential of Colloidal Titanium Dioxide Filmst. *J. Phys. Chem.* **1992**, 5983–5986.

(11) Hotchandani, S.; Bedja, I.; Fessenden, R. W.; Kamat, P. V. Electrochromic and Photoelectrochromic Behavior of Thin WO_3 Films Prepared from Quantum Size Colloidal

Particles. *Langmuir* **1994**, *10*, 17–22.

(12) Sakai, N.; Ebina, Y.; Takada, K.; Sasaki, T. Electronic Band Structure of Titania Semiconductor Nanosheets Revealed by Electrochemical and Photoelectrochemical Studies. *J. Am. Chem. Soc.* **2004**, *126*, 5851–5858.

(13) Wang, C.; Wang, C.; Shim, M.; Shim, M.; Guyot-Sionnest, P.; Guyot-Sionnest, P. Electrochromic Nanocrystal Quantum Dots. *Science* **2001**, *291*, 2390–2392.

(14) Barroso, M.; Mesa, C. A.; Pendlebury, S. R.; Cowan, A. J.; Hisatomi, T.; Sivula, K. Dynamics of Photogenerated Holes in Surface Modified α - Fe_2O_3 Photoanodes for Solar Water Splitting. *Proc. Natl. Acad. Sci. U. S. A.* **2012**, *109*, 15640–15645.

(15) Barroso, M.; Pendlebury, S. R.; Cowan, A. J.; Durrant, J. R. Charge Carrier Trapping, Recombination and Transfer in Hematite (α-Fe_2O_3) Water Splitting Photoanodes. *Chem. Sci.* **2013**, *4*, 2724–2734.

(16) Cerullo, G.; De Silvestri, S. Ultrafast Optical Parametric Amplifiers. *Rev. Sci. Instrum.* **2003**, *74*, 1–18.

(17) Jara, D. H.; Yoon, S. J.; Stamplecoskie, K. G.; Kamat, P. V. Size-Dependent Photovoltaic Performance of $CuInS_2$ Quantum Dot-Sensitized Solar Cells. *Chem. Mater.* **2014**, *26*, 7221–7228.

(18) Tvrdy, K.; Frantsuzov, P. A.; Kamat, P. V. Photoinduced Electron Transfer from Semiconductor Quantum Dots to Metal Oxide Nanoparticles. *Proc. Natl. Acad. Sci. U. S. A.* **2011**, *108*, 29–34.

(19) Abdi, F. F.; Van De Krol, R. Nature and Light Dependence of Bulk Recombination in Co-Pi-Catalyzed $BiVO_4$ Photoanodes. *J. Phys. Chem. C* **2012**, *116*, 9398–9404.

(20) Hong, S. J.; Lee, S.; Jang, J. S.; Lee, J. S. Heterojunction $BiVO_4/WO_3$ Electrodes for Enhanced Photoactivity of Water Oxidation. *Energy Environ. Sci.* **2011**, *4*, 1781–1787.

(21) Bornoz, P.; Abdi, F. F.; Tilley, S. D.; Dam, B.; Van De Krol, R.; Graetzel, M.; Sivula, K. A Bismuth Vanadate-Cuprous Oxide Tandem Cell for Overall Solar Water Splitting. *J. Phys. Chem. C* **2014**, *118*, 16959–16966.

(22) Chen, L.; Alarco, E.; Hettick, M.; Sharp, I. D.; Lin, Y.; Javey, A.; Ager, J. W. Reactive Sputtering of Bismuth Vanadate Photoanodes for Solar Water Splitting. *J. Phys. Chem. C* **2013**, *117*, 21635−21642.

Chapter 8

The effects of surface carbon-containing impurities on the performance of TiO_2-based materials in photocatalytic CO_2 reduction

ABSTRACT

The photocatalytic reduction of CO_2 has been investigated over TiO_2-based materials, modified by surface deposition of Cu and Pt. The work has been carried out as a part of the research project in collaboration with a company that provided different high surface area materials containing only titania or modified with different amounts of Ni and Cu. In this Chapter, the results of a part of such photocatalytic tests are reported, in particular those obtained with a home-made homogeneous series of materials.

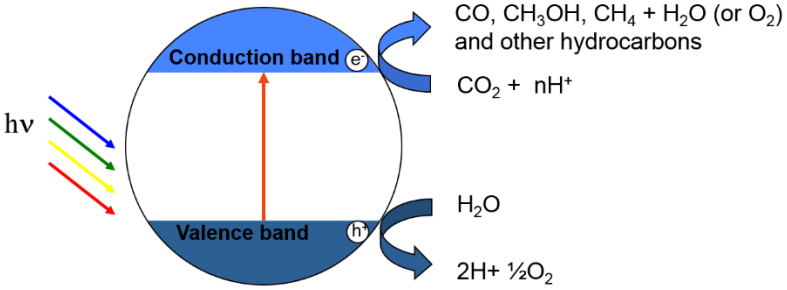

Figure 8.1. Scheme of the photocatalytic CO_2 reduction reaction over semiconductor material.

Photocatalytic CO_2 reduction ideally occurs over an irradiated semiconductor in the presence of water as electron donor (see Figure 8.1). The conduction band of the semiconductor should be more negative in energy that the redox potential of CO_2 reduction. Figure 8.2 reports the redox potentials of the main chemical species involved in this reaction, as well as the band gap position of some of the most studied photocatalytic materials. While the one electron reduction of carbon dioxide is highly unfavorable (the reduction potential is -1.48 vs RHE at pH 0), the multi-step reactions need photoexcited electrons with less reducing power.

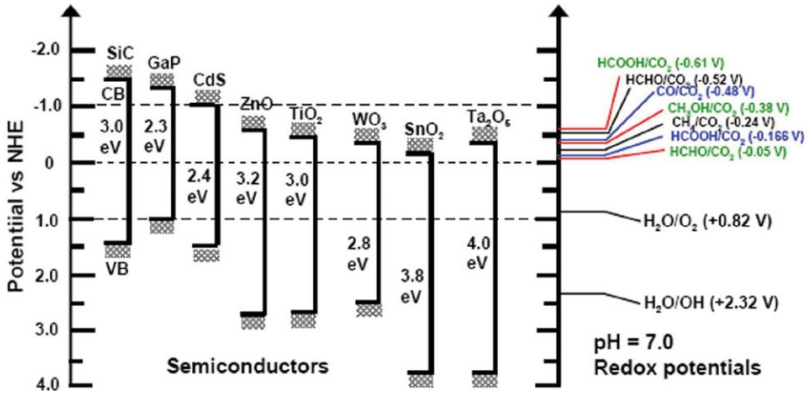

Figure 8.2. Conduction and valence band positions of various photocatalytic materials and the redox potentials at pH 7 of the compounds involved in CO_2 reduction.

1. INTRODUCTION

The rapid depletion of fossil fuel reserves and the environmental impact of the increasing emission and concentration of CO_2 in the atmosphere promoted the search for alternative, clean and renewable energy sources. In this context much interest has been focused in recent years on the development of photocatalytic semiconductor materials allowing one to obtain efficient conversion and storage of solar energy into chemical energy, in the form of hydrocarbons (resulting from CO_2 reduction)[1–3] and H_2 (obtained from water splitting).[4,5] Although CO_2 photoreduction to formaldehyde and methanol in purified water was first reported in 1979,[6] great interest in this reaction has grown only in the last few years. However, the reaction rates are still very low with the best values being around 10 μmol h^{-1} g_{cat}^{-1} for the major products (usually methanol, formic acid or formaldehyde for the reaction in the liquid phase, methane for the gas phase reaction).[7] The results were obtained with SiC, CdS and Nb[8] and Ta-based[9] semiconductors, which have more negative conduction band edges than TiO_2. In the last few years researchers have been studying new semiconducting materials having conduction band higher than that of TiO_2.[10] Photoexcited electrons in this photocatalyst, possess a larger overpotential in order to carry out the extremely up-hill direct reduction of CO_2 to $CO_2^{\cdot-}$ ($E^{\circ}(V)\ vs\ RHE$ = -1.48) or the less demanding two electron reactions of CO or HCOOH production ($E^{\circ}(V)\ vs\ RHE$ -0.11 and -0.19, respectively).[11] On the other hand the prerequisite of a sufficiently high conduction band is often strictly related to the increase of the band gap of photocatalytic materials[12–14] and therefore to the exploitation of a negligible UV portion of the solar spectrum. Moreover, most of the studied materials show a decrease over time

in the rate of products evolution due to photocatalysts deactivation or to consumption, as hole scavenger, of the previously evolved products.[10] Very recently, new promising strategies to undergo such reaction have been reported. For example, the photocatalytic reduction of CO_2 to CH_4 was reported using H_2 as electron donor, in the presence of irradiated nickel supported on silica-alumina;[15] the use of pyridine as electro-catalyst;[16,17] the use of metal organic frameworks as visible light harvesting materials;[18] the band gap narrowing of materials with high conduction band[19] and the use of sensitized semiconductor in Z-scheme systems.[20] Photoelectrochemical CO_2 reduction using small band gap materials such as $CuFeO_2$ coupled with CuO as co-catalysts in the reduction reaction showed a stable *ca.* 1% solar to formate conversion during one week simulated solar light irradiation.[21] Lastly in a novel monolithic assembly using a triple-junction of amorphous silicon-germanium as light absorber and coupled with a porous ruthenium complex polymer and iridium oxide (respectively the CO_2 reduction and water oxidation catalysts), a stable formate evolution has been proved, using water as electron donor, and performing a promising 4.6% solar to chemical energy conversion efficiency.[22]

Although these recent progresses are very promising, the rates of products evolution are still low. Such low yields are comparable to the amount of possible surface carbon-containing species originated in the catalyst synthesis. For example, a typical CH_4 production rate of 10 μmol h^{-1} g_{cat}^{-1} leads during 6 h-long irradiation to 60 μmol g_{cat}^{-1} of CH_4, *i.e.* to *ca.* 1 mg of CH_4 per gram of catalyst. Such amounts are extremely small and pose many doubts, if no isotopic labeling experiments are carried out, whether CH_4 and other reduced species with similar production rate can be ascribed to CO_2 photocatalytic reduction, especially when the rate of products evolution is not linear with time and reaches a plateau after the first few hours of irradiation. Moreover, this holds particularly

if carbon doped photocatalysts or high surface area materials synthesized at low temperature without post annealing treatments are used as photocatalysts in this reaction. The amount of carbonaceous species in the photocatalyst highly affects the evolution rate of the reduced species. Isotopic labeling experiments constitute the proper way to directly prove that the reaction products arise from carbon dioxide reduction and not from other carbon sources, and an increasing number of papers are reporting this important test.[16,20–22] On the other hand not so often isotopic tracing experiments are feasible. Therefore, extreme caution has to be used in the interpretation of the results obtained in photocatalytic carbon dioxide reductions tests and the experimental procedure needs to be carefully planned.

In the present Chapter, the results are reported on the studies performed aiming at evidencing the effect of carbon-containing impurities on the surface of the photocatalyst. The determination of the nature of such carbonaceous compounds is behind the scope of the present investigation.

The studied materials were tested in a recirculating gas phase system[23,24] (similar to that described in Chapter 5) in the photocatalytic H_2 production through steam reforming of methanol and under the typical experimental conditions of photocatalytic CO_2 reduction (namely in the presence of CO_2 and H_2O and using He as inert gas). The first reaction is a good test for ascertaining the reducing properties of the investigated materials in the presence of a hole scavenger, and it usually leads to a linear production of H_2 over time. In the second reaction the rates of CO and CH_4 evolution are not linear during irradiation and in the 6 hours-long test the photocatalysts activity showed a net decrease.

To better discern between the effect due to carbon-containing impurities on the photocatalyst surface and actual photocatalytic carbon dioxide reduction, we divided the photocatalytic reaction test in two steps. In the first step (cleaning step) the photocatalyst was irradiated in an inert environment in the absence of CO_2 and in the presence of moisture. In the second step (irradiation step), the clean photocatalyst was irradiated after the introduction of CO_2 in the recirculating system.

In order to limit the heterogeneity among the studied photocatalysts, a set of four TiO_2-based materials was prepared in our laboratory with the same procedure starting from P25 Evonik. The four materials include simple TiO_2 (T), a 0.1 wt% copper and a 0.5 wt% platinum surface modified TiO_2 (labelled Cu(0.1)/T and Pt/T respectively) and a TiO_2 modified by the co-deposition of 0.1 wt% copper and 0.5 wt% platinum (Pt/Cu(0.1)/T). All these materials were treated with the same procedure used to obtain the Pt/Cu(0.1)/T sample starting from Evonik P25 (see below). Moreover, in order to check if new carbonaceous impurities were introduced by employed surface modification procedure, we tested also TiO_2 P25 as supplied by Evonik (hereafter indicated as P25 in the text). Finally, in order to investigate the effect of the amount of carbon-containing species on the rates of products evolution, a commercial, high surface area titania was also tested, which was obtained by a sol-gel synthesis, followed by spray-drying at low temperature.

2. EXPERIMENTAL SECTION

2.1. Surface modification of P25-based samples by surface deposition of Pt, Cu and Pt-Cu

The here investigated P25-based photocatalysts were prepared in our laboratory through the surface modification of P25-Evonik, directly employed as supplied. This series of materials are currently under further studies and therefore their complete characterization cannot be reported in detail here.

We prepared the Pt/Cu/TiO_2 materials by combining the grafting of Cu(II) metal ions on the TiO_2 surface (step A) with the subsequent Pt nanoparticles (NPs) deposition (step B). Evonik P25 (84% anatase – 16% rutile) was employed as starting material and the impregnation method was employed in step A, using $Cu(NO_3)_2 \cdot 3H_2O$ as Cu(II) source. In particular, two grams of commercial TiO_2 powder were dispersed in 20 mL of Milli-Q water and firstly sonicated for 10 min. A proper amount of $Cu(NO_3)_2 \cdot 3H_2O$, dissolved in 1 ml of water, was then added to the aqueous TiO_2 suspension, heated at 90 °C and kept under stirring for 1 hour in a vial reactor up to complete solvent removal. The so-obtained materials were then dried at 110 °C for 24 hours and ground into fine powders using an agate mortar.

In order to obtain the Pt/Cu(0.1)/T photocatalyst, we proceeded with step B. An aliquot of surface Cu-modified P25 was further modified by the surface deposition of a fixed amount of Pt NPs (0.5 wt.%) according to a modified Deposition-Precipitation (DP) method, using urea as the precipitating agent.[25] The proper amount of pre-sonicated Cu 0.1 wt%-modified P25 (suspended in water) was added to an aqueous solution containing H_2PtCl_6 (0.1 $g \cdot L^{-1}$ Pt) and urea (0.42 M). The suspension, thermostated at 80 °C, was

vigorously stirred for 4 hours, until pH 7.5 was reached. The slurry was then cooled down to room temperature and the solid product was collected by centrifugation, employing a CL10 Thermo Scientific centrifuge. The separated powder was then re-suspended in 20 mL of Milli-Q water and the reduction of surface Pt(IV) to Pt(0) was attained by adding an excess of $NaBH_4$, employed as chemical reductant species. This was accompanied by a change in color of the suspension, from white or slightly green to gray. After 20 min the slurry was centrifuged and washed with 20 mL of Milli-Q water. The washing procedure was repeated for at least three times, in order to remove residual chloride and nitrate anions, the amounts of which in the surnatant were checked to be lower than 1 ppm by ion chromatography. The so obtained photocatalyst was named Pt/Cu(0.1)/T.

Moreover, in order to ascertain the effects induced by the metal deposition procedures on the presence of carbon-containing compounds and to compare the role played by the single metal or by the co-presence of Cu and Pt on the TiO2 surface, three more samples were prepared, as follows. The T sample consisted of modified P25 obtained by following both steps A and B in the absence of the metals precursor. Cu(0.1)/Pt was synthesized by adopting the Cu(II) grafting procedure followed by the DP procedure in the absence of Pt precursor. Pt/T was prepared by following step A in the absence of the Cu (II) source, followed by subsequent Pt nanoparticles (NPs) deposition according to the above described DP method. All chemicals employed in the synthesis of the materials and in the preparation of all solutions were purchased from Aldrich. Water purified by a Milli-Q water system (Millipore) was used throughout. Finally the SD/T sample was a commercial high surface area TiO_2, obtained by sol-gel synthesis, followed by spray-drying at 150°C. The so obtained material retains large amounts of un-combusted carbon species.

2.2. Photocatalytic tests

The photocatalytic activity of the TiO_2-based materials in hydrogen production by photo-steam reforming of methanol and in carbon dioxide photocatalytic reduction has been tested using a bench-scale apparatus, connected to a gas phase closed system.[23,24] The gas phase was recirculated by means of a metal bellows pump and was saturated with the reactant vapors by bubbling it through the reactant solution, namely a 20% methanol solution in deionized water for the photo-steam reforming and pure deionized water for CO_2 reduction. This system was connected to a gas phase photocatalytic reactor with the catalyst powder (16 mg) immobilized on quartz grains and fed with the gas mixture. The gas phase was then bubbled again in the liquid solution. The recirculating phase was analyzed automatically using an Agilent 6890 N gas-chromatograph equipped with two columns (a MolSieve 5A and a plot-U), a methanizer and two detectors (a flame ionization and thermal conductivity detectors). The irradiation source was a 300W Xenon lamp (LOT Oriel LSH 302). Prior to the beginning of irradiation, the system was preliminarily purged with an inert gas, nitrogen or helium, in order to remove any oxygen trace. During the photocatalytic experiment, the temperature of the gas mixture was maintained at 30°C.

The composition of the recirculating gas phase in the photo-steam reforming tests was 2% CH_3OH, 4% H_2O, 94% N_2. The two platinum containing samples (Pt/Cu(0.1)/T and Pt/T), because of the high H_2 production rate attained, were irradiated for 2 hours, so as to maintain below 0.5 bar the pressure of the recirculating phase. The two hours-long runs were repeated three times. Between each irradiation cycle the system was purged with N_2 for 40 min, in order to remove all gaseous products. The Pt-free samples (P25, T,

(Cu0.1)/T and SD/T) were irradiated for 6 hours under gas phase recirculation. Each sample was tested twice to check the reproducibility of the photocatalytic experiments.

In CO_2 photoreduction tests, the gas phase consisted of 12% CO_2, 4% H_2O, 84% He. As already mentioned, in order to study the role of the carbon-containing species the photocatalytic CO_2 experiments were divided into two steps. After 40 min-long purging with He, the sample were first irradiated for 2.25 hours in the absence of CO_2 and fed, in recirculation mode, with He and steam (cleaning step). Then after a second 40 min-long purging step with He, the irradiation was carried out in the presence of CO_2, for 3.75 hours. Each sample was tested three times. A 6 hours-long CO_2 photocatalytic reduction test was also performed with the Pt/T sample, in order to check the deactivation of the photocatalyst after prolonged irradiation. From CO_2 vs. time evolution tests, we checked that after two hours-long pre-irradiation the sample was almost completely cleaned from surface carbon-containing species. Finally a 6 hours-long water splitting experiment was carried out with the (Cu0.1)/T sample in the presence of only N_2 and steam, in order to investigate the possible role of surface carbonaceous species as electron donors.

3. RESULTS AND DISCUSSION

3.1. Photocatalytic steam reforming of methanol

The photocatalytic activity results of the studied materials in hydrogen production by photo-steam reforming of methanol are summarized in Table 1. Pt/T systems were more active than the corresponding unmodified materials or the sample containing only Cu, as a consequence of the well-known positive role in photoactivity of noble metals that, acting as a trap of electrons photoexcited in the conduction band, increase the efficiency of electron-hole separation.[26,27] A synergistic effect on photoactivity induced by the co-

presence of Cu and Pt on the TiO_2 surface can be clearly outlined in the case of Pt/Cu(0.1)/T. The rate of H_2 production obtained with this sample overcomes the sum of those obtained with the samples singly modified with Cu or Pt. The three bare TiO_2 samples showed similar photocatalytic performances, with the T sample performing better than P25 used as supplied, probably because of the prolonged thermal treatment at 110 °C. The high hydrogen production rate obtained with the SD/T sample is likely due to its high surface area and to the presence of large amounts of unburnt carbon containing species.

Table 8.1. H_2 evolution rate obtained in the photo-steam reforming of methanol.

		H_2
	Photocatalyst	**mmol g_{cat}^{-1} g^{-1}**
1	P25	0.168
2	T	0.3
3	Cu(0.1)/T	4.5
4	Pt/T	16.1
5	Pt/Cu(0.1)/T	23.728
6	SD/T	0.346

3.2. Photocatalytic experiments in the presence of CO_2 and moisture

While in the steam reforming reaction the photocatalysts allowed for a linear H_2 evolution over time (see previous section), their activity during CO_2 reduction decreased over the irradiation time and the production of reduced species was not linear with time. Figure 8.3 shows the typical time evolution profile of CH_4 production during 6 hours irradiation in the presence of CO_2. Clearly, the photoactivity of the Pt/T sample rapidly decreased during the first half of the experiment, the rate of CH_4 production becoming very low in the last three hours.

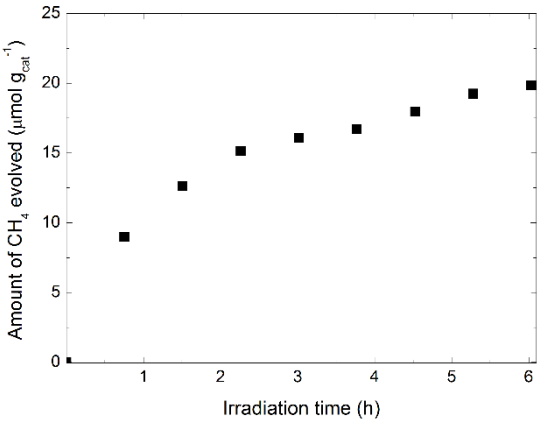

Figure 8.3. CH_4 time evolution profile obtained on Pt/T sample irradiated for 6 hours in presence of a 4% moisture and 94% helium gas phase.

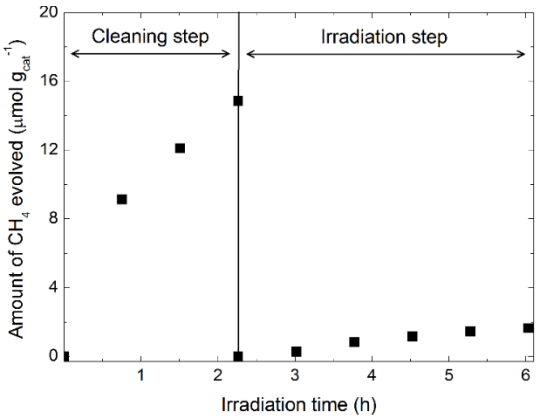

Figure 8.4. CH_4 time evolution profile obtained with Pt/T during a two step photocatalytic CO_2 reduction experiment. During the 2.25 hours long cleaning step the photocatalyst was irradiated in the presence of a gas phase containing 4% moisture and 94% helium. Prior to the 3.75 hours long irradiation , CO_2 was introduced in the recirculating gas phase.

The rapid decrease in the rate of methane evolution does not provide evidence of the photocatalytic activity of the semiconductor material. Therefore, aiming at establishing the origin of the observed photocatalyst deactivation, we divided the test reaction into two steps. An example of a two-step photocatalytic test over the Pt/T photocatalyst is reported in Figure 8.4. We observed that most of the produced methane evolved during the cleaning step in the absence of CO_2. During the irradiation step in the presence of CO_2 the photocatalyst seems to be less active and a lower amount of CH_4 was detected with respect to the first step.

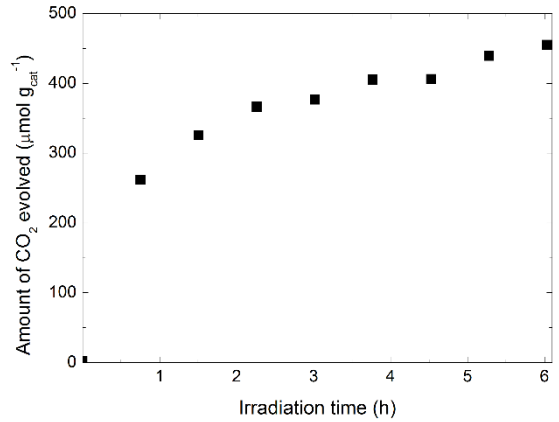

Figure 8.5. Carbon dioxide time evolution profile obtained on Pt/T sample irradiated for 6 hours in presence of a 4% moisture and 94% helium gas phase.

We then carried out a 6 hours long irradiation test in the absence of CO_2. We found that during the first 2.25 irradiation hours a considerable amount of CO_2 evolved (see Figure 8.5). This unexpected evolution of carbon dioxide, likely originated from the decomposition of carbon-containing compounds, which are the only carbon source present during the cleaning step.

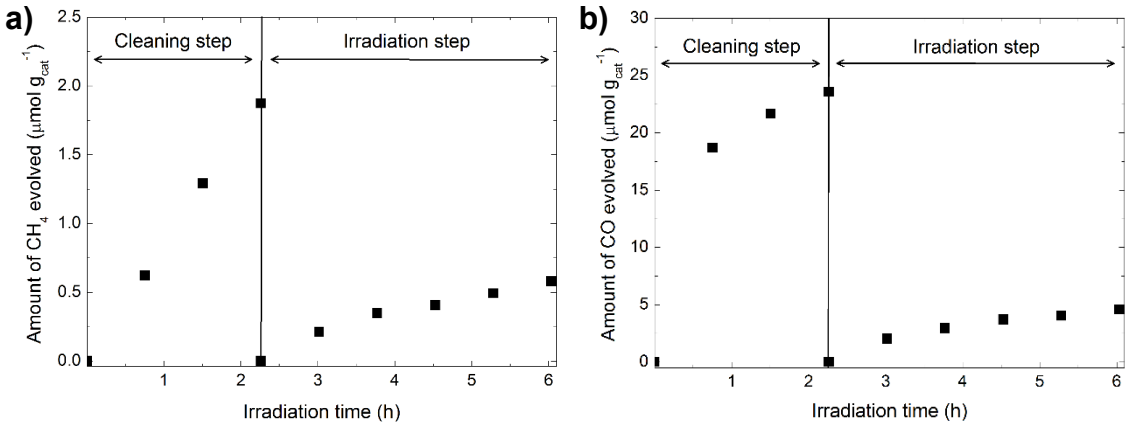

Figure 8.6. a) CH_4 and b) CO evolved during the cleaning and irradiation step of CO_2 photocatalytic reduction experiments with Cu(0.1)/T.

The two-steps photocatalytic CO_2 reduction experiments carried out with all materials showed an abrupt decrease in the evolution rate of carbon-containing reduced products between the two steps (see Figures 8.6 and 8.7 for the CH_4 and CO time evolution profiles obtained with the Cu(0.1)/T and SD/T samples).

The photocatalytic rates of methane, carbon monoxide and ethane production, obtained over the six tested catalysts during the cleaning and irradiation step, are summarized in Table 8.2 and Figure 8.8, while the total amount of CO_2 evolved during the cleaning step is reported in Figure 8.9.

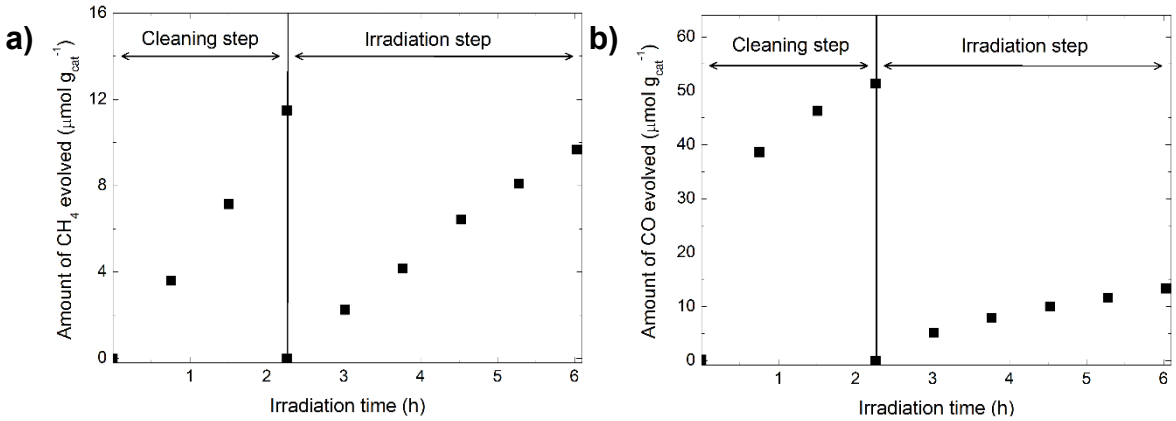

Figure 8.7. a) CH_4 and b) CO evolved during the cleaning and irradiation step of CO_2 photocatalytic reduction experiments with the SD/T sample.

Table 8.2. CH_4, CO and CH_3CH_3 evolution rates obtained during the cleaning step and irradiation step of the photocatalytic carbon dioxide reduction experiments: P25 as supplied from Evonik (line a and A), after the thermal and chemical treating described in section (T in line b and B), after surface modification with 0.1wt% of Cu (Cu(0.1)/T in line c and C), 0.5wt% of Pt (Pt/T in line d and D) and the co-modification with both 0.1wt%Cu and 0.5wt%Pt (Pt/Cu(0.1)/T in line e and E). In line f and F are reported the results obtained for the high surface area commercial spray dried sample.

			CH_4	CO	CH_3CH_3
		Photocatalyst	**μmol g_{cat}^{-1} g^{-1}**	**μmol g_{cat}^{-1} g^{-1}**	**μmol g_{cat}^{-1} g^{-1}**
Cleaning step	**a**	P25	0.4	2.2	--[a]
	b	T	0.3	2.9	--[a]
	c	Cu(0.1)/T	0.8	10.5	0.4
	d	Pt/T	4.1	0.2	0.2
	e	Pt/Cu(0.1)/T	6.6	0.3	0.3
	f	SD/T	5.0	22.2	--[a]
Irradiation step	**A**	P25	0.2	1.4	--[a]
	B	T	0.2	1.0	--[a]
	C	Cu(0.1)/T	0.1	1.3	--[a]
	D	Pt/T	0.7	0.3	--[a]
	E	Pt/Cu(0.1)/T	0.4	0.2	--[a]
	F	SD/T	2.6	3.5	--[a]

[a]: no CH_3CH_3 was detected.

An extremely low ethane evolution was recorded only during the cleaning step for the three surface modified TiO_2 samples. Among the home-made samples the catalysts showing the best selectivity in CH_4 production are those modified by Pt deposition. And when employing these samples CO was detected in very low, steady concentrations. Cu(0.1)/T allowed for the highest selectivity toward CO, while T and unmodified P25 showed intermediate selectivity toward this product. The co-presence of platinum

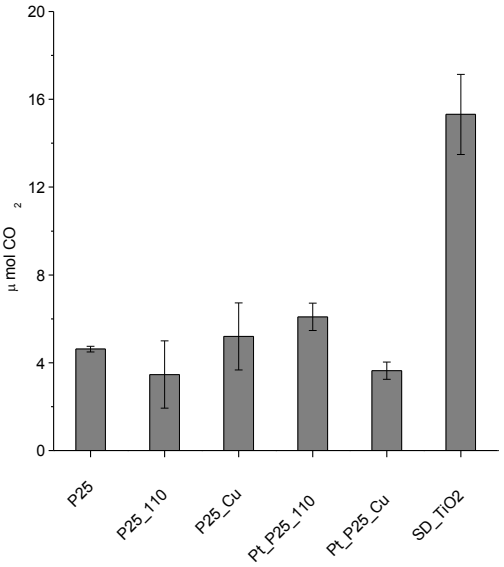

Figure 8.9. Total CO_2 evolution obtained during the cleaning step for all the six studied photocatalysts.

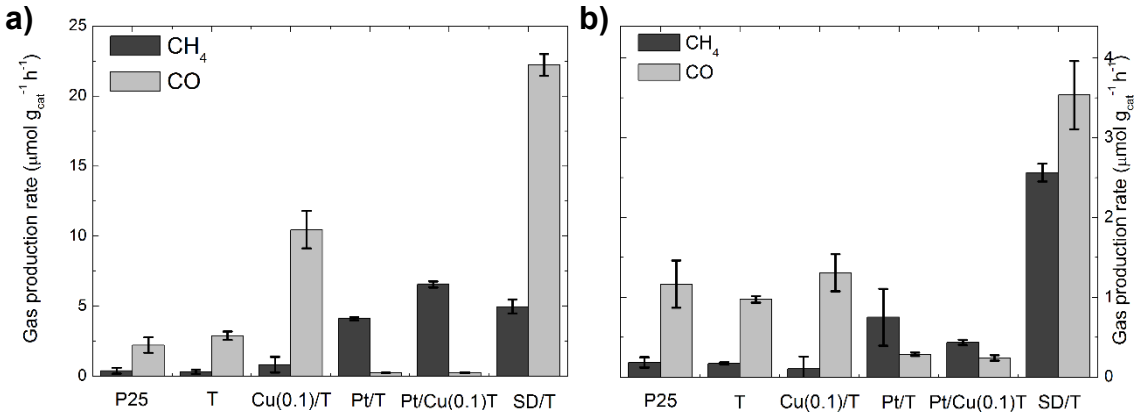

Figure 8.8. CH_4 and CO evolution rates obtained a) during the cleaning step and b) during the irradiation step of CO_2 photocatalytic reduction experiments over the six photocatalysts investigated in this study.

and copper in the Pt/Cu(0.1)/T sample highly enhanced the production rate of methane and a value of 6.6 μmol h^{-1} g_{cat}^{-1} was obtained in the cleaning step. The selectivity to CO and CH_4 with all studied photocatalysts did not show substantial difference between the pre-irradiation and the irradiation step.

The commercial, high surface area SD-TiO_2 sample showed good productivity of both CO and CH_4. Although no surface modification was performed on this sample, the production rates of both products are quite high compared to those obtained with the other two unmodified catalysts. Very likely this is due to the massive presence of carbon-containing compounds, persisting on the photocatalyst surface as a consequence of the low temperature adopted in the preparation of this photocatalyst. In fact, during the cleaning step, a volume of *ca.* 0.4 mL of CO_2 evolved after 2.25 irradiation hours. This volume is *ca.* two order of magnitude higher than both CH_4 and CO evolved volumes during the same irradiation period (0.005 mL and 0.020 mL for CH_4 and CO, respectively).

3.3 Comparison between H_2 productions from photo-steam reforming of methanol and CO_2 reduction

In order to obtain useful information on the role played by the surface carbon-containing compounds, the four semiconductors prepared through the same surface modification technique, namely T, Cu(0.1)/T, Pt/T and Pt/Cu(0.1)/T, were employed as photo-catalysts in the two studied test reaction (H_2 production from photo-steam reforming and CH_4 production in the CO_2 photocatalytic reduction).

We found that the rate of H_2 production and of CH_4 production during the cleaning step well correlate each other, as reported in Figure 8.10a. Therefore the reducing properties of the four different materials are perfectly retained in the two test reactions. More interestingly, the linear correlation suggests that the carbonaceous impurities act as hole scavengers in a way similar to methanol in H_2 photocatalytic production. During the cleaning step, surface impurities are consumed and methane evolution consequently drops during the following irradiation step. On the other hand, the correlation does not hold in the irradiation step (see Figure 8.10b).

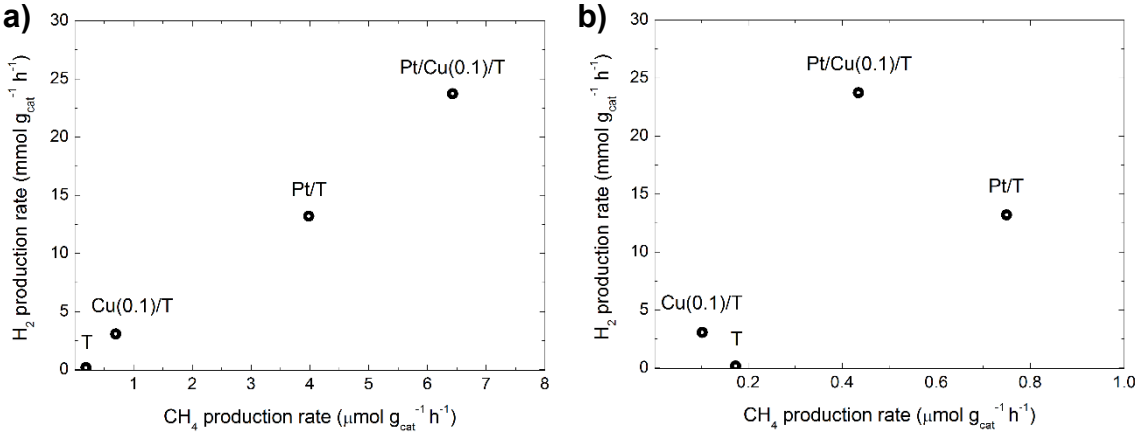

Figure 8.10. Comparison between the rates of photocatalytic H_2 evolution in the presence of methanol as electron donor and of CH_4 evolution in a) the cleaning step and b) the irradiation step of the CO_2 photocatalytic reduction experiments with the four photocatalysts modified by the same procedures.

Finally, in order to obtain more insight on the electron donor character of the surface carbon-containing species we performed a water splitting reaction test (*i.e.* H_2 evolution in the presence of only N_2 and H_2O vapors as reactant). The results are reported in Figure 8.11). The H_2 evolution profile obtained during irradiation of the Pt/Cu(0.1)/T sample is similar to that of CH_4 evolution shown in Figure 8.3. This demonstrates that photocatalytic H_2 production take place only during the first two irradiation hours, when the partially reduced carbon containing species act as electron donors.

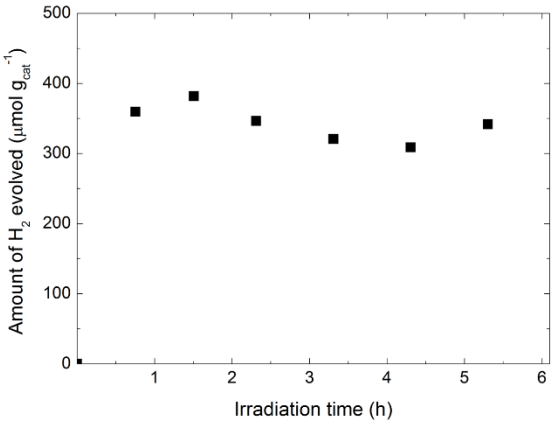

Figure 8.11. Photocatalytic H_2 accumulation profile over the Pt/Cu(0.1)/T photocatalyst in the presence of N_2 and water vapors as the only electron donor.

4. CONCLUSIONS

In this Chapter we discussed the effect of the carbon-containing species already present at the photocatalyst surface prior to photocatalytic CO_2 reduction. The evolution of few μmol g_{cat}^{-1} h^{-1} of methane takes place in the absence of CO_2, in the cleaning step, Therefore the detected reduced products do not arise from the photoassisted reduction of CO_2 on the here employed materials. Actually, in the cleaning step, methane can only originate from the partially reduced carbon-containing species already present at the photocatalyst surface, which are the only carbon source during the first step. The decreased CH_4 and CO evolution rates observed after the consumption of such carbon sources, point out that such surface impurities play a fundamental role in the evolution of the reduced gaseous species. The linear correlation found for the comparison between the production rates obtained in photocatalytic H_2 production in the presence of an hole

scavenger and CH_4 evolution during the cleaning step of the photocatalytic CO_2 reduction, suggests that the carbonaceous impurities act both as electron donor and as carbon-containing substrates. Therefore, due to the low production rates observed for this photocatalytic reaction, the effects of carbon-containing impurities has to be taken into account especially for photocatalysts synthetized through low temperature synthetic procedures using organic precursors. If isotopic labeling experiments are precluded, the here adopted two steps reaction test is a valid method to partially discern if the reduced products arise effectively from photocatalytic CO_2 reduction.

REFERENCES

(1) Izumi, Y. Recent Advances in the Photocatalytic Conversion of Carbon Dioxide to Fuels with Water And/or Hydrogen Using Solar Energy and beyond. *Coord. Chem. Rev.* **2013**, *257*, 171–186.

(2) Tu, W.; Zhou, Y.; Zou, Z. Photocatalytic Conversion of CO_2 into Renewable Hydrocarbon Fuels: State-of-the-Art Accomplishment, Challenges, and Prospects. *Adv. Mater.* **2014**, *26*, 4607–4626.

(3) Habisreutinger, S. N.; Schmidt-Mende, L.; Stolarczyk, J. K. Photocatalytic Reduction of CO_2 on TiO_2 and Other Semiconductors. *Angew. Chemie Int. Ed.* **2013**, *52*, 7372–7408.

(4) Hisatomi, T.; Kubota, J.; Domen, K. Recent Advances in Semiconductors for Photocatalytic and Photoelectrochemical Water Splitting. *Chem. Soc. Rev.* **2014**, *43*, 7520–7535.

(5) Ager III, J. W.; Shaner, M.; Walczak, K.; Sharp, I. D.; Ardo, S. Experimental Demonstrations of Spontaneous, Solar-Driven Photoelectrochemical Water Splitting. *Energy Environ. Sci.* **2015**, *2*, 1–3.

(6) Inoue, T.; Fujishima, A.; Konishi, T.; Honda, K. Photoelectrocatalytic Reduction of Carbon Dioxide in Aqueous Suspensions of Semiconductor Powders. *Nature* **1979**, *277*.

(7) Yui, T.; Kan, A.; Saitoh, C.; Koike, K.; Ibusuki, T.; Ishitani, O. Photochemical Reduction of CO_2 Using TiO_2: Effects of Organic Adsorbates on TiO_2 and Deposition of Pd onto TiO_2. *ACS Appl. Mater. Interfaces* **2011**, *3*, 2594–2600.

(8) Shi, H.; Zou, Z. Photophysical and Photocatalytic Properties of $ANbO_3$ (A=Na, K) Photocatalysts. *J. Phys. Chem. Solids* **2012**, *73*, 788–792.

(9) Pan, P.-W.; Chen, Y.-W. Photocatalytic Reduction of Carbon Dioxide on $NiO/InTaO_4$ under Visible Light Irradiation. *Catal. Commun.* **2007**, *8*, 1546–1549.

(10) Navalón, S.; Dhakshinamoorthy, A.; Alvaro, M.; Garcia, H. Photocatalytic CO_2 Reduction Using Non-Titanium Metal Oxides and Sulfides. *ChemSusChem* **2013**, *6*, 562–577.

(11) Zhao, J.; Wang, X.; Loo, J. S. C. Hybrid Catalysts for Photoelectrochemical Reduction of Carbon Dioxide : A Prospective Review on Semiconductor / Metal Complex Co-Catalyst Systems. *J. Mater. Chem. A Mater. energy Sustain.* **2014**, *00*, 1–6.

(12) Iizuka, K.; Wato, T.; Miseki, Y.; Saito, K.; Kudo, A. Photocatalytic Reduction of Carbon Dioxide over Ag Cocatalyst-Loaded $ALa_4Ti_4O_{15}$ (A = Ca, Sr, and Ba) Using Water as a

Reducing Reagent. *J. Am. Chem. Soc.* **2011**, *133*, 20863–20868.

(13) Liu, Q.; Zhou, Y.; Kou, J.; Chen, X.; Tian, Z.; Gao, J.; Yan, S.; Zou, Z. High-Yield Synthesis of Ultralong and Ultrathin Zn_2GeO_4 Nanoribbons toward Improved Photocatalytic Reduction of CO_2 into Renewable Hydrocarbon Fuel. *J. Am. Chem. Soc.* **2010**, *132*, 14385–14387.

(14) Ahmed, N.; Morikawa, M.; Izumi, Y. Photocatalytic Conversion of Carbon Dioxide into Methanol Using Optimized Layered Double Hydroxide Catalysts. *Catal. Today* **2012**, *185* (1), 263–269.

(15) Sastre, F.; Puga, A. V; Liu, L.; Corma, A.; García, H. Complete Photocatalytic Reduction of CO□ to Methane by H□ under Solar Light Irradiation. *J. Am. Chem. Soc.* **2014**, *136* (19), 6798–6801.

(16) Boston, D. J.; Xu, C.; Armstrong, D. W.; MacDonnell, F. M. Photochemical Reduction of Carbon Dioxide to Methanol and Formate in a Homogeneous System with Pyridinium Catalysts. *J. Am. Chem. Soc.* **2013**, *135* (44), 16252–16255.

(17) Riboni, F.; Selli, E.; Colussi, A. J. Homogeneous Reduction of CO_2 by Photogenerated Pyridinyl Radicals. *J. Phys. Chem. A* **2015**, *119*, 4433–4438.

(18) Zhang, T.; Lin, W. Metal-Organic Frameworks for Artificial Photosynthesis and Photocatalysis. *Chem. Soc. Rev.* **2014**, 5982–5993.

(19) Links, D. A. Mesoporous Zinc Germanium Oxynitride for CO_2 Photoreduction under Visible Lightw. **2012**, 1269–1271.

(20) Arai, T.; Sato, S.; Kajino, T.; Morikawa, T. Solar CO_2 Reduction Using H_2O by a Semiconductor/metal-Complex Hybrid Photocatalyst: Enhanced Efficiency and Demonstration of a Wireless System Using $SrTiO_3$ Photoanodes. *Energy Environ. Sci.* **2013**, *6*, 1274.

(21) Kang, U.; Choi, S. K.; Ham, D. J.; Ji, S. M.; Choi, W.; Han, D. S.; Abdel-Wahab, A.; Park, H. Photosynthesis of Formate from CO_2 and Water at 1% Energy Efficiency via Copper Iron Oxide Catalysis. *Energy Environ. Sci.* **2015**, *8*, 2638–2643.

(22) Arai, T.; Sato, S.; Morikawa, T. Monolithic Device for CO2 Photoreduction to Generate Liquid Organic Substances in a Single-Compartment Reactor. *Energy Environ. Sci.* **2015**, *8*, 1998–2002.

(23) Chiarello, G. L.; Forni, L.; Selli, E. Photocatalytic Hydrogen Production by Liquid- and Gas-Phase Reforming of CH_3OH over Flame-Made TiO_2 and Au/TiO_2. *Catal. Today* **2009**, *144*,

69–74.

(24) Chiarello, G. L.; Dozzi, M. V.; Scavini, M.; Grunwaldt, J.-D.; Selli, E. One Step Flame-Made Fluorinated Pt/TiO_2 Photocatalysts for Hydrogen Production. *Appl. Catal. B Environ.* **2014**, *160-161*, 144–151.

(25) Dozzi, M. V.; Prati, L.; Canton, P.; Selli, E. Effects of Gold Nanoparticles Deposition on the Photocatalytic Activity of Titanium Dioxide under Visible Light. *Phys. Chem. Chem. Phys.* **2009**, *11*, 7171–7180.

(26) Chiarello, G. L.; Aguirre, M. H.; Selli, E. Hydrogen Production by Photocatalytic Steam Reforming of Methanol on Noble Metal-Modified TiO_2. *J. Catal.* **2010**, *273*, 182–190.

(27) Subramanian, V.; Wolf, E. E.; Kamat, P. V. Catalysis with TiO_2/gold Nanocomposites. Effect of Metal Particle Size on the Fermi Level Equilibration. *J. Am. Chem. Soc.* **2004**, *126*, 4943–4950.

Chapter 9

Conclusions and perspectives

1. CONCLUSIONS

The aim of this work was to obtain visible light harvesting materials active as photocatalysts for the production of renewable solar fuels. By shortly summarizing, chronologically the topics which I treated during the last three years studied the photocatalytic carbon dioxide reduction over titania-based materials, hydrogen production using CdSe QDs as visible light harvesting materials and, finally, in the second half of my PhD work, I focused my attention on photoelectrocatalytic water splitting using electrodes based on $BiVO_4$, WO_3 and their heterojunction.

1.1 CO_2 photoassisted reduction with TiO_2 based materials

The results described in Chapter 8, obtained as a part of a PON project during the first year of PhD, showed that photocatalytic gas-phase CO_2 reduction is not a feasible process over the tested materials. The use of TiO_2 as a photocatalyst presents evident drawbacks: even with a large band gap of 3.2 eV, its conduction band is too low in energy and consequently photopromoted electrons do not have sufficient energy to carry out the direct gas-phase reduction of CO_2. The observed CH_4 and CO evolution occurring under irradiation showed to be ascribed to the more thermodynamically favorable reduction of the carbon containing species already present at the photocatalysts surface. Once these carbon based compound are consumed, CH_4 evolution does not take place any more. Moreover, such surface impurities act as sacrificial agent, initially pushing the activity of the photocatalytic materials. The very small amount of impurities present at the photocatalyst surface give rise to detectable CH_4 or CO amounts. Therefore the evolution of reduced carbon – containing species in photocatalytic CO_2 reduction over TiO_2 materials has to be carefully proved employing

techniques such as isotopic labeling experiments. On the other hand, when this kind of experiments is not feasible, the two step photocatalytic test discussed in Chapter 8 allow one to obtain information on the source of the reduced products.

Recently new approaches to carry out such reaction have been developed: for example the co-presence of an electro catalyst (such as pyridine) or the photothermal approach in the presence of H_2 as reductant led to promising results.[1,2] Very recently the photocatalytic reduction of CO_2 to CO over $CuFeO_2$/CuO (solar to chemical efficiency of 1%) and a photoelectrocatalytic approach with ZnTe/ZnO photocathodes also led to promising results. Such studies employed photocatalytic materials having high conduction bands.[3,4] That is one of the key points to be checked to follow in order to successfully develop photocatalytic CO_2 reduction.

1.2 Photocatalytic properties of CdSe QDs in the H_2 production under visible light

High stability, good light to hydrogen conversion efficiency and high molar extinction coefficient make CdSe quantum dots very promising materials in photocatalysis. We found that the 2.8 nm sized CdSe QDs showed the best activity in the studied reaction because it possess the proper balance between light harvesting properties, conduction band position and low recombination rate between photogenerated electron/hole couples.[5] The synthesis of nanocrystal (NC) assisted by non-coordinating solvents is an extremely versatile tool that allows to obtain NCs with different shapes. The combination of hole and electron acceptors in multi component structures should lead to charge separation and highly efficient solar light exploitation.[6] Moreover reproducibility is a big issue in QDs and generally in NCs preparation: in fact temperature changes of only few tens of degrees lead to drastically different NCs growth kinetics.

Neverteless CdSe QDs are very promising materials, which merit to be further investigated as photocatalytic systems in connection with other semiconductors. In particular these but in general all semiconductor photocatalytic materials (refer to Chapter 2 and 3 for some examples) should potentially be prepared through high temperature synthesis in non-coordinating solvents, in order to obtain them in different shapes with tunable properties. Still such new materials merit to be characterized and fully exploited in new field of photocatalysis.

1.3 PEC properties and charge carriers dynamics in WO_3, $BiVO_4$ and $WO_3/BiVO_4$ photoanodes

Preliminary results[7] concerning this topic are presented in Chapter 6 and successively deepened in Chapter 7. Femtosecond TAS has been successfully applied to extract reliable and useful information on the kinetics of photogenerated charges. By following the evolution over time of the transient species ascribed to surface trapped holes, we indirect information on the dynamics of photoexcited electrons was got. Using pumps with different energy, allowed us to evidence that the interfacial interaction between the two oxides is wavelength dependent. In the coupled $WO_3/BiVO_4$ system, by exciting $BiVO_4$ exclusively with a 500 nm pump, extremely long living holes are produced, while by exciting both oxides with a 387 pump, the holes become shorter living, with respect to single $BiVO_4$. Therefore, the effect of spatial charge separation on the electron/hole pairs was directly evidenced. For the first time evidence was provided that holes the lifetime of the holes is extended after charge (electron) exchange $BiVO_4$ and WO_3. Charge separation occurs on a tens of picosecond timescale and therefore probably involves photoexcited hot electrons in $BiVO_4$. From the results obtained in

these studies we proposed a scheme for the photogenerated charge interactions between the two oxides in the coupled WO_3/$BiVO_4$ system, which was validated by PEC experiments.

Photoelectrochemical devices based on visible light harvesting materials are very promising and extremely recent improvements showed that 10 % solar to hydrogen conversion efficiency, which is the lower limit for a widespread commercialization, should be probably achieved in the next ten years. Due to the harsh reaction conditions, durability remains the main issue for the materials employed in such application. However semiconductor oxides such as WO_3, Fe_2O_3 and $BiVO_4$ show good stability and the use of passivation or protective layers (for example Al_2O_3 and NiO) should further extend the lifetime of photoanodes based on such materials.[8,9]

It is worth underlining that $BiVO_4$ and other narrow band gap semiconductors possess the appropriate properties to be employed in the near future as photoanode materials for the water oxidation reaction in real practical devices. Good transparency is necessary in order to study the charge carriers dynamics with femtosecond transient absorption spectroscopy and for future application in tandem devices. The solution processed preparation adopted in this study allows us to obtain very transparent films with tunable thickness which should be employed for the preparation of multilayered films of semiconductors also different from those studied here.

2. PERSPECTIVES

The work of the last two years has contributed to elucidate some of the important properties of the interaction between WO_3 and $BiVO_4$ in heterojunction photoanodes. This coupled system is the most studied for PEC applications. On the other hand many

different semiconductor combinations are possible and, by choosing the materials with the proper band gap alignment, charge separation should potentially lead to the better exploitation of the visible spectrum, in a way similar to natural photosynthetic systems.[10,11]

Recently the use of amorphous TiO_2, has been employed to protect Si photoanodes from oxidation as well as oxide photoanode materials from photodegradation and opened a new research field that merits to be studied.[9] The charge carriers dynamics in such systems should be studied through fs-TAS, which only in the last years has become and popular in the photocatalytic field. However, films with suitable optical properties need to be employed in such field of studies and data elaboration is not trivial. On the other hand, the obtained information should potentially be used to address the limitations concerning the slow water oxidation reaction and the recombination of the photogenerated charge carriers, to ultimately attain lead to the assembly of highly efficient photoanodes.

(1) Riboni, F.; Selli, E.; Colussi, A. J. Homogeneous Reduction of CO_2 by Photogenerated Pyridinyl Radicals. *J. Phys. Chem. A* **2015**, *119*, 4433–4438.

(2) Sastre, F.; Puga, A. V; Liu, L.; Corma, A.; García, H. Complete Photocatalytic Reduction of CO2 to Methane by H2 under Solar Light Irradiation. *J. Am. Chem. Soc.* **2014**, *136*, 6798–6801.

(3) Jang, Y. J.; Jang, J.-W.; Lee, J.; Kim, J. H.; Kumagai, H.; Lee, J.; Minegishi, T.; Kubota, J.; Domen, K.; Lee, J. S. Selective CO Production by Au Coupled ZnTe/ZnO in the Photoelectrochemical CO_2 Reduction System. *Energy Environ. Sci.* **2015**.

(4) Kang, U.; Choi, S. K.; Ham, D. J.; Ji, S. M.; Choi, W.; Han, D. S.; Abdel-Wahab, A.; Park, H. Photosynthesis of Formate from CO_2 and Water at 1% Energy Efficiency via Copper Iron Oxide Catalysis. *Energy Environ. Sci.* **2015**, *8*, 2638–2643.

(5) Grigioni, I.; Bernareggi, M.; Sinibaldi, G.; Dozzi, M. V.; Selli, E. Size-Dependent Performance of CdSe Quantum Dots in the Photocatalytic Evolution of Hydrogen under Visible Light Irradiation. *Appl. Catal. A Gen.* **2015**.

(6) Wu, K.; Chen, Z.; Lv, H.; Zhu, H.; Hill, C. L.; Lian, T. Hole Removal Rate Limits Photodriven H_2 Generation Efficiency in CdS-Pt and CdSe/CdS-Pt Semiconductor Nanorod-Metal Tip Heterostructures. *J. Am. Chem. Soc.* **2014**, *136*, 7708–7716.

(7) Grigioni, I.; Stamplecoskie, K. G.; Selli, E.; Kamat, P. V. Dynamics of Photogenerated Charge Carriers in WO_3/$BiVO_4$ Heterojunction Photoanodes. *J. Phys. Chem. C* **2015**, *119*, 20792–20800.

(8) Steier, L.; Herraiz-Cardona, I.; Gimenez, S.; Fabregat-Santiago, F.; Bisquert, J.; Tilley, S. D.; Grätzel, M. Understanding the Role of Underlayers and Overlayers in Thin Film Hematite Photoanodes. *Adv. Funct. Mater.* **2014**, *24*, 7681–7688.

(9) Hu, S.; Shaner, M. R.; Beardslee, J. A.; Lichterman, M.; Brunschwig, B. S.; Lewis, N. S. Amorphous TiO_2 Coatings Stabilize Si, GaAs, and GaP Photoanodes for Efficient Water Oxidation. *Science.* **2014**, *344*, 1005–1009.

(10) Cowan, A. J.; Durrant, J. R. Long-Lived Charge Separated States in Nanostructured Semiconductor Photoelectrodes for the Production of Solar Fuels.

Chem. Soc. Rev. **2013**, *42*, 2281–2293.

(11) Durrant, J. R. Molecular Approaches to Solar Energy Conversion: The Energetic Cost of Charge Separation from Molecular-Excited States. *Philos. Trans. R. Soc. A* **2013**, *371*, 20120195.

LIST OF SCIENTIFIC CONTRIBUTIONS

Stage abroad

Between March 08 and September 25, 2014 I worked in Professor P. Kamat's research group in the Radiation Laboratory of the University of Notre Dame, Indiana, US.

Presentations delivered during group meetings in Prof. Kamat's research group:

- 21/03/2014
- 11/09/2014

Oral communication

Dynamics of photogenerated charge carriers in WO_3/$BiVO_4$ heterojunction photoanodes

I. Grigioni, P. V. Kamat, E. Selli

presented at the Italian Photochemistry Meeting 2014, Abbiategrasso (MI), Italy, November 27-29 November 2014.

Congress attended

4th International Conference on Semiconductor Photochemistry (SP4), Prague, Czech Republic, June 23rd to 27th 2013.

Italian Photochemistry Meeting 2014, Abbiategrasso (MI), Italy, November 27-29 November 2014.

Poster Presentation

Poster on the topics treated during the three years at PhD, presented at the event for the closure of the first SmartMat lab courses session, 30 April 2015, Dipartimento di Chimica, Università degli Studi di Milano.

"Photocatalytic CO_2 reduction vs. hydrogen production from CH_3OH/H_2O on a series of metal modified titanias" I. Grigioni, M.V. Dozzi, E. Selli; 4th International Conference on Semiconductor Photochemistry (SP4) Prague, Czech Republic, June 23rd to 27th 2013.

E. SELLI, M.V. Dozzi, G.L. Chiarello, I. Grigioni:
Photocatalytic hydrogen production on Cu(II) pre-grafted Pt/TiO2,
Italian Photochemistry Meeting 2014, Cascina Caremma (MI), November 27-29, 2014.

E. SELLI, M.V. Dozzi, G.L. Chiarello, I. Grigioni:
Photocatalytic hydrogen production on Cu(II) pre-grafted Pt//TiO2,
Italian Photochemistry Meeting 2013, Rifreddo (PZ), 28 novembre – 1 dicembre 2013.

E. SELLI, M.V. Dozzi, G.L. Chiarello, I. Grigioni:
Photocatalytic hydrogen production on Cu(II) pre-grafted Pt//TiO2,
3rd European Symposium on Photocatalysis, Portorož, Slovenia, September 25-27, 2013.
ISBN 978-961-6311-78-6.

M.V. Dozzi, G.L. Chiarello, I. Grigioni, E. SELLI:
Photocatalytic activity of Cu(II) pre-grafted Pt/TiO2 in hydrogen production,
XLI Congresso Nazionale di Chimica Fisica, Alessandria, 23-27 giugno 2013.

Publications

1. I. Grigioni, K. G. Stamplecoskie, P. V. Kamat, E. Selli, Dynamics of photogenerated charge carriers in WO_3/$BiVO_4$ heterojunction photoanodes, *J. Phys. Chem. C,* **2015***, 119,* 20792-20800.

2. I. Grigioni, M. Bernareggi, G. Sinibaldi, M. V. Dozzi, E. Selli, Size-dependent performance of CdSe quantum dots in the photocatalytic evolution of H_2 under visible light irradiation, *App. Catal. A: Gen.,* **2015**, doi: 10.1016/j.apcata.2015.09.021

3. M. V. Dozzi, A. Zuliani, I. Grigioni, G. L. Chiarello, L. Meda, E. Selli, Photocatalytic activity of one step flame-made fluorine doped TiO_2, *App. Catal. A: Gen.*, 2015, doi: 10.1016/j.apcata.2015.10.048

4. I. Grigioni, M. V. Dozzi, M. Bernareggi, G. L. Chiarello, E. Selli, The effects of surface carbon-containing impurities on the performance of TiO_2-based materials in photocatalytic CO_2 reduction. *in preparation*

5. I. Grigioni, M. V. Dozzi, K. G Stamplecoskie, P. V. Kamat, G. Cerullo, E. Selli, The wavelength dependent charge carrier exchange between WO_3 and $BiVO_4$ in coupled WO_3/$BiVO_4$ systems. *in preparation*